Sensor-Assisted Condition Evaluation of Steel and Prestressed Concrete Girder Bridges Subjected to Fire - Phase III

Genda Chen, PhD
Professor and Robert W. Abbett Distinguished Chair in Civil Engineering
Director, Center for Intelligent Infrastructure
Director, INSPIRE University Transportation Center
Associate Director, Mid-America Transportation Center
Department of Civil, Architectural, and Environmental Engineering
Missouri University of Science and Technology

Yanping Zhu, PhD,
Postdoctoral Scholar
Department of Civil, Architectural, and
Environmental Engineering
Missouri University of Science and Technology

**MISSOURI
S&T**

2023

Sensor-Assisted Condition Evaluation of Steel and Prestressed Concrete Girder Bridges – Phase
III

Genda Chen, Ph.D., P.E., F. ASCE
Professor and Robert W. Abbett Distinguished Chair in Civil Engineering
Director, Center for Intelligent Infrastructure
Director, INSPIRE University Transportation Center
Associate Director, Mid-America Transportation Center
Department of Civil, Architectural, and Environmental Engineering
Missouri University of Science and Technology

Yanping Zhu, Ph.D. Postdoctoral Fellow
Department of Civil, Architectural, and Environmental Engineering
Missouri University of Science and Technology

Technical Report Documentation Page

1. Report No. 25-1121-0005-131-3	2. Government Accession No.	3. Recipient's Catalog No.	
4. Title and Subtitle Sensor-Assisted Condition Evaluation of Steel and Prestressed Concrete Girder Bridges Subjected to Fire – Phase III		5. Report Date July 2023	
		6. Performing Organization Code	
7. Author(s) Yanping Zhu, and Genda Chen		8. Performing Organization Report No. 25-1121-0005-131-3	
9. Performing Organization Name and Address Center for Intelligent Infrastructure Department of Civil, Architectural, and Environmental Engineering Missouri University of Science and Technology 500 W. 16th Street Rolla, MO 65409-0810		10. Work Unit No. (TRAIS)	
		11. Contract or Grant No. 69A3551747107	
12. Sponsoring Agency Name and Address Mid-America Transportation Center 2200 Vine St PO Box 830851 Lincoln, NE 68583-0851		13. Type of Report and Period Covered Final Report January 1, 2020 – July 30, 2023	
		14. Sponsoring Agency Code MATC TRB RiP No. 91994-51	
15. Supplementary Notes			

16. Abstract

This report summarizes the results and findings of Mid-America Transportation Research Center (MATC) research project No. 61706. It is focused on the measurement of strain and temperature in steel plates under high temperatures using a tunable-wavelength coherent optical time domain reflectometry (TW-COTDR) technique. The main objectives of this study are: (a) to experimentally investigate the effect of heat treatment on Rayleigh scattering based distributed single-mode fiber optic temperature measurement; (b) to quantify Rayleigh scattering based measurement accuracy of distributed fiber optic sensors under a heating-holding load protocol and characterize the effect of polymer coating on the sensors as the polymer softens and melts away at elevated temperatures; (c) to experimentally and numerically investigate effectiveness and limitation of Rayleigh scattering based, distributed fiber optic sensors (DFOS) without coatings for measuring temperature and strain of a steel plate subjected to a local constant temperature. One-time heat treatment eliminates the hysteresis effect and stabilizes the Rayleigh scattering based fiber optic temperature measurement up to 1000 ℃. The typical dual-layer coating effect on the temperature sensitivity of the Rayleigh frequency shift can be neglected at high temperatures in civil engineering application. It is found that the DFOS accurately measured the temperature and strain of the steel plate with different bond lengths of the epoxy, as compared to the thermocouple temperature and thermal-induced strain, respectively. The maximum strain (or temperature) that the DFOS without coatings could measure for the steel plate was less than 1600 $\mu\varepsilon$ (or 150 ℃). The fibers attached on steel plates with epoxy function like an extensometer at 155 °C~267 °C as a center portion of the coating with the high-end temperature is melted.

17. ORCID No. of each Researcher Genda Chen: 0000-0002-0658-4356		18. Distribution Statement		
19. Security Classif. (of this report) Unclassified	20. Security Classif. (of this page) Unclassified		21. No. of Pages 105	22. Price

Table of Contents

List of Figures

List of Tables

Acknowledgments

Disclaimer

The contents of this report reflect the views of the authors, who are responsible for the facts and the accuracy of the information presented herein. This document is disseminated in the interest of information exchange. The report is funded, partially or entirely, by a grant from the U.S. Department of Transportation's University Transportation Centers Program. However, the U.S. Government assumes no liability for the contents or use thereof.

Abstract

This report summarizes the results and findings of the Mid-America Transportation Research Center (MATC) research project No. 61707. It is focused on the measurement of strain and temperature in steel plates under high temperatures using a tunable-wavelength coherent optical time domain reflectometry (TW-COTDR) technique. The main objectives of this study are: (a) to experimentally investigate the effect of heat treatment on Rayleigh-scattering-based distributed single-mode fiber optic temperature measurement; (b) to quantify Rayleigh-scattering-based measurement accuracy of distributed fiber optic sensors under a heating-holding load protocol and characterize the effect of polymer coating on the sensors as the polymer softens and melts at elevated temperatures; (c) to experimentally and numerically investigate effectiveness and limitation of Rayleigh-scattering-based, distributed fiber optic sensors (DFOS) without coatings for measuring temperature and strain of a steel plate subjected to a local constant temperature. One-time heat treatment eliminates the hysteresis effect and stabilizes the Rayleigh-scattering-based fiber optic temperature measurement up to 1000 ℃. The typical dual-layer coating effect on the temperature sensitivity of the Rayleigh frequency shift can be neglected at high temperatures in a civil engineering application.

The polymer was found to start softening at 155 ℃ and melting at 267 ℃. As temperature sensors, optical fibers with an insulation sheath can accurately measure temperature until 155 ℃ without and 267 ℃ with thermo-mechanical analysis of sheath-fiber bonding behavior. As strain sensors, optical fibers with temperature compensation are accurate for strain measurement until 155 °C, above which strain transfer analysis is required due to softening of the fiber coating. Under a large temperature gradient covering 155 °C to 267 °C, the fibers attached on steel plates

with epoxy function like an extensometer as a center portion of the coating with the high-end

temperature is melted as verified by microscopic analysis.

It was found the DFOS accurately measured the temperature and strain of the steel plate

with different bond lengths of the epoxy, as compared to the thermocouple temperature and

thermal-induced strain, respectively. The maximum strain (or temperature) that the DFOS

without coatings could measure for the steel plate was less than 1600 $\mu\varepsilon$ (or 150 ℃). The elastic

modulus of epoxy within 100 MPa and the rectangular cross-section of epoxy (0.5 mm thick and

4 mm wide) could achieve a strain transfer coefficient of 0.997, while the initial defect has a

similar effect on the strain transfer to the protective coating. The normal-distribution epoxy

shape is designed for guiding robot assisted intelligent instrumentation and construction in the

future.

Chapter 1 Heat Treatment and Polymer Coating Effect on Rayleigh Scattering Based
Fiber Optic Temperature Measurement

1.1 Introduction

Heat treatment has been used for improving thermal stability and measurement operation

range of fused silica optical fiber because it can repair defects produced during material

manufacturing and relieve residual stress or strain, which relates to changes of density and

refractive index of the optical fiber (Zu et al. 2016; Zhong et al. 2022; Xu et al. 2018).

Specifically, Si-O covalent bonds with varying strengths form an irregular tetrahedral network of

the fused silica. The weak bonds are easily fractured, and stronger bonds re-form because of

absorbed energy at high temperatures (Yablon 2004). As a result, the change of the physical

structure directly influences optical fiber-based strain or temperature measurement. For example,

after the Fiber Bragg Grating (FBG) sensors with inscribed gratings were subjected to heat

treatment, the temperature operation range and thermal stability were enhanced because the

residual, frozen-in stresses in the fused silica optical fiber were released (Li et al. 2009; Shin et

al. (2008). However, the partial releasing of frozen-in stresses at a temperature of 200 ℃ to 300

℃ in the FBG sensors made by ultraviolet irradiation reduced strain and temperature sensitivities

(Mihailov 2012). The FBG sensors' ability to function at high temperatures (such as 600 ℃ to

700 ℃) is still a concern due to grating erasure.

Different from point sensors (i.e., FBG sensors), a telecom-grade single-mode fused

silica optical fiber can be directly used as fully distributed temperature and strain sensors based

on Rayleigh, Brillouin, and Raman scattering (Tan et al. 2022; 2016). The fully distributed

sensors are supposed to operate at high temperatures because no additional preparation and

fabrication are needed for the optical fiber, and the fiber glass core and cladding can survive at a

temperature of more than 1000 ℃ (Bao et al. 2016). Also, the fully distributed sensors are

notable for monitoring conditions of large-scale structures and bridges, simplifying instrumentation, and obtaining sufficient data informati (Guo et al. 2020).

Recently, Bao and Chen (2016a) was extending the Brillouin-scattering-based single-mode fiber optic temperature measurement range to 1000 ℃ through annealing treatment. However, to date, the Rayleigh-scattering-based distributed temperature measurement at high temperature has not been fully investigated. A simple ultraviolet exposure technique was proposed for improving signal strength and sensitivity in Rayleigh-scattering-based distributed temperature and strain sensing (Loranger et al. 2015). Li et al. (2003) reported that the Rayleigh intensity normalized by the ambient temperature value was linearly dependent on the temperature up to 827 ℃ in a dispersion-shifted fiber. Kishida et al. (2014) reported a hysteresis effect (i.e., varying Rayleigh frequency at the same temperature in the heat and cool stages) for temperature measurement in the first cycle up to 180 ℃ probably caused by the strain variation of the coating materials (Rizzolo et al. 2016), and then hybrid Brillouin-Rayleigh strategy was proposed for removing this hysteresis effect (i.e., decoupling thermal-induced strain from the temperature effect) (Kishida et al. 2012). Although it is assumed a few heating-cooling cycles would eliminate the hysteresis effect, it is unknown if or how the heat treatment works at high temperatures (up to 1000 ℃). In addition, the fiber coating effect on the temperature response of distributed fiber optic sensors based on coherent Rayleigh and Brillouin scatterings in a cryogenic environment (about -53 ℃) was investigated (Lu et al. 2018). It was found that the temperature sensitivity increased by 50% at cryogenic temperature due to the stiffer inner coating. The effect of polymer coatings on temperature measurement sensitivity of the double-coated optical fiber based on the Brillouin optical time domain analysis technique at temperatures ranging from 10 ℃ to 80 ℃ was assessed (Gu et al. 2013). It was found that the

enhancement of the Brillouin frequency shift temperature sensitivity was achieved for optical fibers with different outer polymer coatings. Due to different coatings on optical fibers used, it is necessary to quantify and validate the coating effect on the temperature measurement sensitivity and enhance confidence in the temperature measurement accuracy when the Rayleigh-scattering-based distributed fiber optic sensors are instrumented in engineering structures for high temperature application.

This study aims to investigate the heat treatment effect on the high temperature measurement performance (up to 1000 ℃) of a single-mode optical fiber based on a tunable-wavelength coherent optical time domain reflectometry (TW-COTDR) technique that is cross-correlating the Rayleigh scattering signal with respect to the reference (Neubrescope 2012). The optical fiber has two-layer coatings with diameters of 190 and 242 μm. The inner coating layer is made by soft visco-elastic materials (Young's modulus smaller than 10 MPa) to decrease the attenuation due to micro-bending, while the outer coating is stiffer to prevent the optical fiber from mechanical damage. In addition, the inner coating is usually formed immediately after the glass core and cladding, while the outer coating can be formed later. The effect of the dual-layer coatings on the Rayleigh-scattering-based temperature measurement needs to be clarified experimentally and numerically before they soften and melt, which motivates this study. The diameters of the glass core and cladding are 8.2 and 125 μm, respectively. The glass cladding usually guides the light into the glass core. Both the glass core and cladding are made of silica glass, and their material properties are almost the same and not easily changed by the external environment (such as high temperature). Figure 1.1 shows the cross-section of the double-coated optical fiber with layers' diameters. Other parameters of the optical fiber are as follows: effective refractive index of 1.468, mode field diameter of 10.4 μm, dispersion and attenuation of smaller

than 18 ps/nm/km and 0.02 dB/km at a wavelength of 1550 nm, respectively. The temperature-dependent frequency sensitivity coefficients of the optical fiber is investigated experimentally. The effect of heat treatment on the temperature sensor stability and measurement generalization of the optical fiber is discussed. Also, the coating effect on the fiber core strain and temperature measurement sensitivity is investigated numerically and experimentally. Parametric studies from finite element modeling are performed to investigate the effect of geometric and material parameters on the fiber core strain coatings to guide the coating layer designs of the Rayleigh-scattering-based distributed fiber optic temperature sensors.
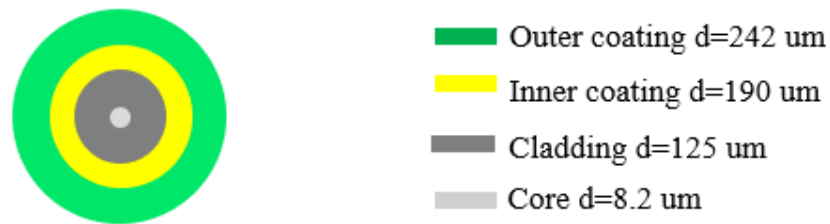
Figure 1.1 Cross section of single mode optical fiber with standard coating. Gray: fiber glass cladding and core; Green: outer coating; Yellow: inner coating

1.2 Principle of TW-COTDR

TW-COTDR technique is used for sensing the Rayleigh scattering signature of the optical fiber. The working tunable laser wavelength ranges between 1530 and 1560 nm. Only single-end fiber access is needed for this technique and the distributed measurement can provide a spatial resolution of two centimeters (Planes et al. 2017). Through a reference measurement, temperature and strain changes along the optical fiber length can be simultaneously measured using the Rayleigh scattering signature. The Rayleigh scattering difference through the cross-correlation with respect to Planes et al. represents a frequency shift at a given time, which relates

to temperature and strain changes applied to the optical fiber. Compared to the Brillouin scattering, this time domain Rayleigh scattering approach has several advantages: single-end fiber access; detectable for small changes, such as creep monitoring over long distances; and same precision and sensitivity as an FBG sensor, but with distributed sensing results. One disadvantage is the relatively slow measurement (up to a few minutes), which relates to the measurement distance and scanning frequency ranges.

As the coherent Rayleigh sensor has the same working principle as an FBG sensor, the well-established grating theory can be used for describing the working principle of the Rayleigh sensor. Therefore, the Bragg wavelength change caused by strain and temperature variations is written as follows:

$$\Delta\lambda_B = \lambda_B\left(\left\{1 - \frac{n^2[P_{12} - \eta_0(P_{11} + P_{12})]}{2}\right\}\varepsilon_z + \left(\alpha_0 + \frac{1}{n}\frac{dn}{dT}\right)\Delta T\right) = \lambda_B\left(S_\varepsilon^R\varepsilon_z + S_T^R\Delta T\right) \qquad (1.1)$$

where, λ_B represents the Bragg wavelength; n is the optical fiber refractive index; P_{11} and P_{12} are Pockel's coefficients of the stress-optic tensor; the factor $1 - \frac{n^2[P_{12} - \eta_0(P_{11} + P_{12})]}{2}$ can be taken as a constant (such as 0.22 (Lu et al. 2018)); $\frac{dn}{dT}$ represents the silica thermo-optic coefficient; and S_ε^R and S_T^R are the corresponding temperature and strain sensitivities. In the above equation, the strain in the radial direction is implicitly considered through Poisson's ratio (η_0), in addition to the explicit strain in the axial direction (ε_z). Note that the above equation is a theoretical solution for the temperature and strain sensitivities as well as a theoretical formula for calculating the wavelength change $\Delta\lambda_B$ (converted to frequency change Δf_B) caused by strain and temperature effects. Therefore, the modified temperature sensitivity equal to frequency shift per temperature

increment (ΔT) due to the thermal expansions of coatings is as follows: if the coatings impose strains to the optical fiber core as temperature changes, the temperature sensitivity is enhanced due to the first term of equation (1.2).

$$\Delta f_B / \Delta T = S_\varepsilon^R \varepsilon_z / \Delta T + S_T^R \qquad (1.2)$$

1.3 Experimental Program

As shown in Figure 1.2, a distributed sensor supposedly free of strain was passed through a temperature-controlled furnace. One end of the optical fiber sensor was connected to the pump end of the data acquisition system (Model NBX-7020 with a spatial resolution of 2 cm). The furnace previously used by Bao and Chen (2016b) included a steel case (A-D), heat insulation fabrics (A-B, C-D), a 200-mm heating coil-wrapped ceramic tube (B-C) in the middle, and an electric thermocouple at the center of the ceramic tube. The thermocouple for monitoring temperature had an accuracy of $\pm$ 0.5 ℃ until 1000 ℃. During the test, the B-C segment of the optical fiber inside the ceramic tube was heated according to the preset temperature increment. As summarized in Table 1.1, two temperature protocols are considered with temperature increment and duration at 1000 ℃ of (1) 20 ℃ and 90 (and 60 min) and (2) 30 ℃ and 90 min. These increments are selected to ensure a stable Rayleigh scattering signal with the TW-COTDR technology since the Rayleigh frequency shift in the cross-correlation based technique cannot be more than about 72 GHz (Piccolo et al. 2019). From later test results, it is found that the length of time at 1000 ℃ does not significantly affect measured frequency difference results, which is different from the conclusion in the Brillouin scattering based temperature measurement (Bao

and Chen 2016b). The insignificant difference in two Rayleigh frequency shifts at 1000 ℃ during the expected duration is partially due to a slight lagging temperature increase.
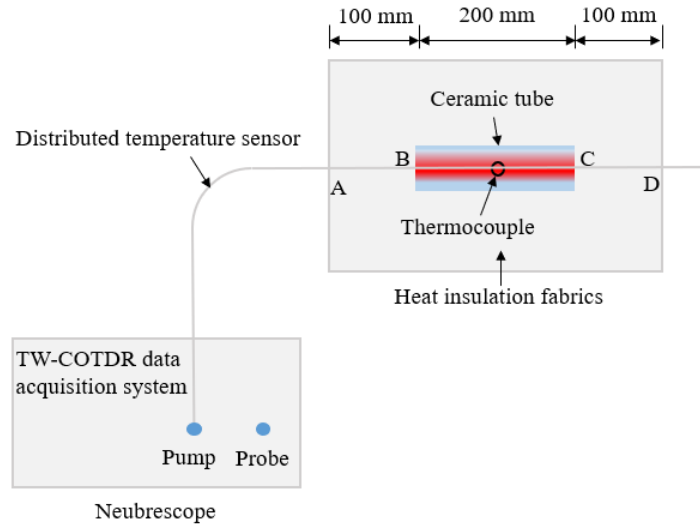
Figure 1.2 Test setup

Table 1.1 Temperature protocols

No.	Temperature increment (℃)	Duration at each temperature increment (min)	Duration at 1000 ℃ (min)	Cooling method
(1)	20	7	90 (and 60)	Naturally cooling
(2)	30	7	90	Naturally cooling

Figure 1.3 shows a typical temperature protocol for the heat treatment, where R^2 represents the determination coefficient. The blue line and red lines represent the temperature over time measured by the thermocouple and the measured accumulated Rayleigh frequency as a function of time. The temperature variation has three stages for one test. First, the temperature linearly increases from 20 ℃ to 1000 ℃ in 345 min (i.e., heat stage). Then it has a short, sustained temperature stage at 1000 ℃ for maintaining expected duration. Finally, a natural cooling stage is experienced before test completion. The cooling stage can be well fitted by an

7

exponentially decayed curve and the equation is presented in Figure 1.3. In the heating stage, the temperature increment is 20 ℃ or 30 ℃ and each temperature increment needs about 4 minutes. At a target temperature, the Rayleigh frequency difference measurement needs about 2 minutes and 30 seconds in this study. Therefore, the time duration for each temperature increment is about 7 minutes as indicated in Table 1.1. This time duration is accumulated for creating temperature-time curve in Figure 1.3. In the cooling stage, the Rayleigh frequency differences along the optical fiber were measured at the same temperatures as the heating stage and the continuous drop temperatures were recorded by the thermocouple as well. Note that the Rayleigh frequency differences at the middle point of the optical fiber in the ceramic tube were accumulated to create the Rayleigh frequency-time curve in Figure 1.3 and these middle point values will be used for the Rayleigh frequency-temperature curves. In Figure 1.3, the Rayleigh frequency almost linearly increases in the linear heat stage, and the Rayleigh frequency shows a similar decreasing trend (absolute value) to the temperature cool stage. Moreover, during the sustained temperature time, the Rayleigh frequency almost remains unchanged as described before. In Figure 1.3, the temperature and the Rayleigh frequency reach the peaks at almost the same time, as indicated by the red dash line. This demonstrates the duration at 1000 ℃ does not have significant influence on the Rayleigh frequency change.
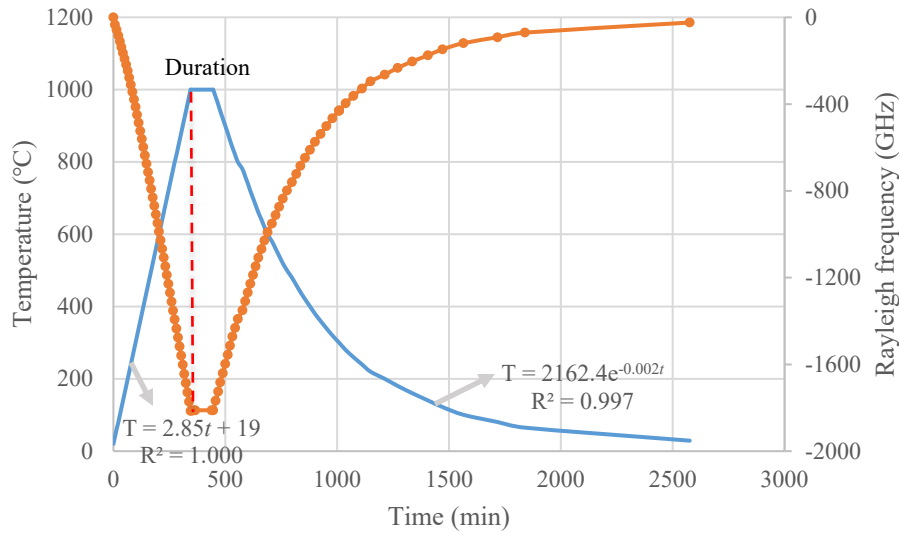
Figure 1.3 Temperature (denoted as T) protocol (1) and its corresponding frequency time (denoted as t) function

1.4 Theoretical analysis

   To clarify the coating effect on the temperature coefficient of the optical fiber subjected to thermal load, it is necessary to establish a thermomechanical model to analyze the axial strain behavior of the glass core and cladding. First, a thermogravimetric test for coatings was conducted to investigate the critical temperature at which the coatings soften and melt away and thus, the working temperature range of the coatings in the thermomechanical analysis was identified. Specifically, the polymer coatings (mass unit: mg) were stripped off an optical fiber tested in this study using a fiber stripper. The sample was tested in the nitrogen gas environment with a flow rate of 100 ml/min. The sample was then heated at a rate of 10 ℃/min from room temperature to 600 ℃ and measured from a Simultaneous Thermal Analyzer (SDT, TA Instruments Q600). Figure 1.4 shows the representative test results from one coating sample. The normalized heat flow (red line) and weight (black line) changes with temperature are presented.

The melting temperature of slightly below 315 ℃ was identified from the sudden reduction in heat flow (Figure 1.4(a)).

In addition, the first derivative of the normalized weight curve with respect to temperature was obtained with the aid of Universal Analysis Software 2000, as shown in Figure 1.4(b). The temperature corresponding to 5% reduction in weight is approximately 282 ℃ for the coatings. To conservatively estimate the effective working temperature range, a temperature of 200 ℃ is considered effective. Subjected to thermal load only (no other external loads), the optical fiber glass core, inner coating, and outer coating layers expand differently with temperature changes because they have different thermal expansion coefficients. The thermal-induced strains and stresses in radial, tangential, and axial directions of each layer of the optical fiber with two coatings subjected to temperature increment can be calculated by the Lame solutions and boundary conditions in equations (1.3)-(1.9):
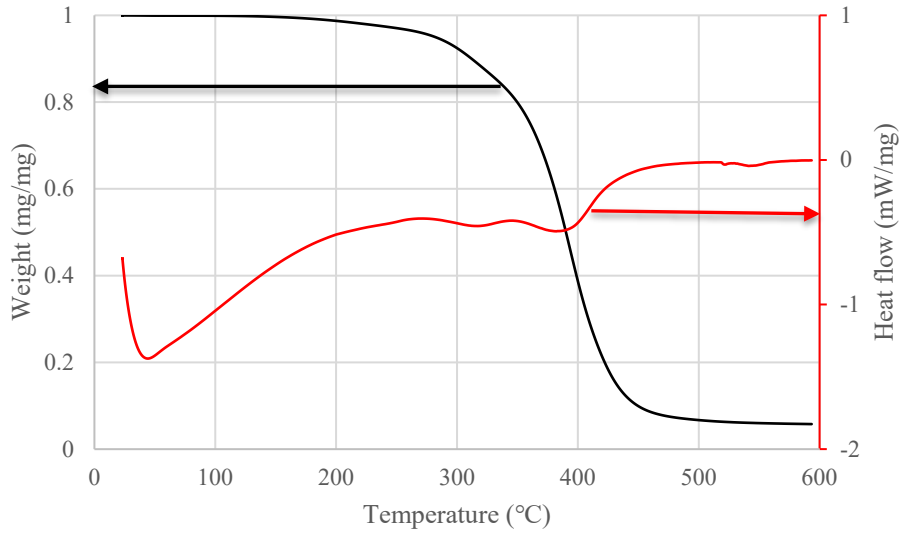
(a)
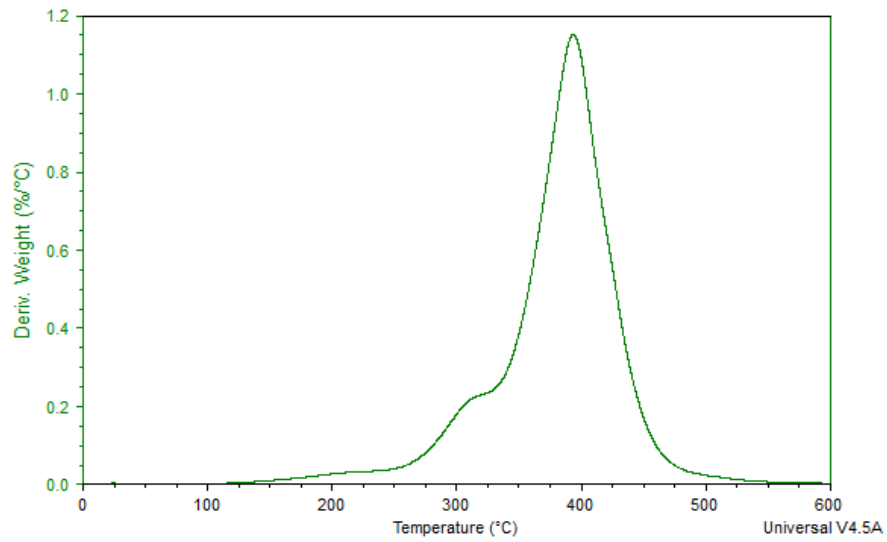
(b)

Figure 1.4 Thermal gravimetric analysis results for coatings(a) weight and heat flow (b) first derivative of normalized weight with respect to temperature

$$
\begin{aligned}
\begin{matrix} \sigma_r^i \\ \sigma_\theta^i \\ \sigma_z^i \end{matrix} =
\begin{matrix} \xi_i + 2\mu_i & \xi_i & \xi_i \\ \xi_i & \xi_i + 2\mu_i & \xi_i \\ \xi_i & \xi_i & \xi_i + 2\mu_i \end{matrix} =
\begin{matrix} \varepsilon_r^i - \alpha_i \Delta T \\ \varepsilon_\theta^i - \alpha_i \Delta T \\ \varepsilon_z^i - \alpha_i \Delta T \end{matrix}
\end{aligned}
\qquad (1.3)
$$

where $i = 0, 1, 2$ represents the different layers, α_i is the linear coefficient of thermal expansion, ξ_i and μ_i are Lame parameters, expressed as:

$$\xi_i = \eta_i E_i / [(1 + \eta_i)(1 - 2\eta_i)] \tag{1.4}$$

$$\mu_i = 2E_i / [2(1 + \eta_i)] \tag{1.5}$$

η_i is Poisson's ratio, E_i is Young's modulus; the factors ε_r^i, ε_θ^i, and ε_z^i represent the strains in radial, tangential, and axial dimensions, respectively, expressed as follows:

$$\varepsilon_r^i = U_i + V_i / r^2, \, \varepsilon_\theta^i = U_i - V_i / r^2, \, \varepsilon_z^i = W_i \tag{1.6}$$

where U_i, V_i, and W_i are constants which can be identified by the boundary conditions. The continuity between different layers has:

$$\sigma_r^i(r_i) = \sigma_r^{i+1}(r_i) \, i = 0, 1 \tag{1.7}$$

$$\mu_r^i(r_i) = \mu_r^{i+1}(r_i) \, i = 0, 1$$

where, r_i is the radius of the ith layer. Moreover, the optical fiber is considered to have no applied external forces, then,

$$\sigma_r^2(r_2) = 0, \sum_{i=0}^{2} \sigma_z^i A_i = 0 \tag{1.8}$$

where, A_i represents the cross-section area of the ith layer.

Because the optical fiber is a long and thin cylinder, a plain strain is assumed, and the following equation is established:

$$\varepsilon_z^0 = \varepsilon_z^1 = \varepsilon_z^2 = \varepsilon_z \qquad (1.9)$$

Moreover, due to the axisymmetric optical fiber and finite strains in the radial direction ε_r^0 and tangential dimension ε_θ^0 at the center layer, from the above equation, $V_0 = 0$ when the axisymmetric thermal load is applied in the present study. Nine unknowns can be solved with nine boundary conditions.

1.5 Finite element modeling

To further investigate the thermal-induced strains of the optical fiber subjected to thermal load due to different thermal expansion coefficients among coatings and fused silica fiber, a finite element analysis was conducted using ABAQUS. First, the finite element model was validated by the analytical calculation as derived above, an analytical study that has been performed in two previous studies (Lu et al. 2018; Gu et al. 2013). Figure 1.5 shows the finite element model of the optical fiber (the whole length of 200 mm from the test setup). The TIE technology available in ABAQUS was applied to the interfaces between the fiber glass and inner coating as well as the inner coating and outer coating. The radii of the fiber glass, inner coating, and outer coating are 62.5 μm, 95 μm, and 125 μm, respectively, in accordance with the geometrical dimensions in (Lu et al. 2018) as listed in Table 1.2.

Note that a small difference in the radius of the outer coating can be observed in this study. Since two cases (room temperature and about -53 ℃) were considered in finite element modeling, different material properties were selected. Table 1.2 lists the main material properties

at room temperature. At about -53 ℃, the elastic modulus of the inner coating was 2.6 GPa; the thermal expansion coefficient of the inner coating was 118×10^{-6} /℃. In addition, the thermal expansion coefficient of the fiber glass was 0.21×10^{-6} /℃. To achieve thermal load, a temperature increment of 1 ℃ was applied to the whole model to investigate the thermal-induced strains and the above-discussed parameters were assumed temperature-independent during the calculation for each case. The general mesh size was 1 mm, and 16 elements were assigned to the circles of each component to achieve mesh-independent simulation. The element shape was hex-dominated, and the sweep technique was used. The C3D8RH stress element (i.e., 8-node linear brick, hybrid, constant pressure, reduced integration, hourglass control) was used for the three materials. The hybrid formulation was chosen to avoid a convergence problem since the bulk modulus exceeds 100 times the shear modulus.
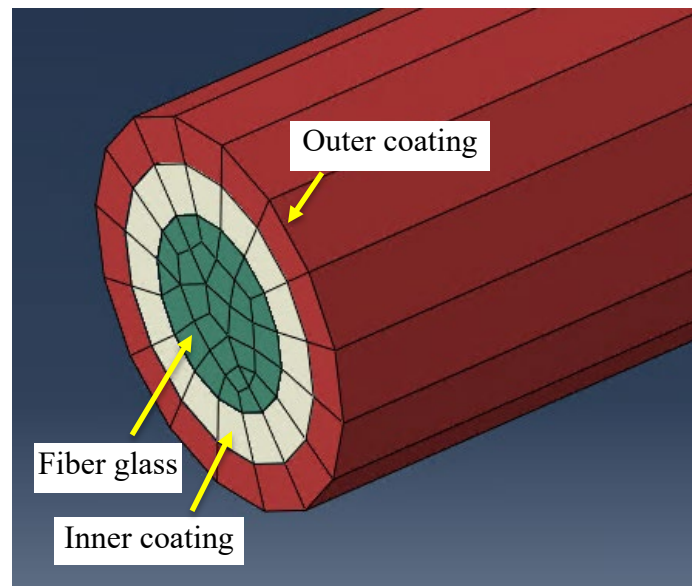
Figure 1.5 Finite element model for optical fiber

Table 1.2 Relevant physical parameters of the optical fiber with its dual-layer coating [18]

r_0	$62.5\ \mu m$	η_0	0.17	E_0	72 GPa	α_0	$0.45 \times 10^{-6}\ °C^{-1}$
r_1	$95\ \mu m$	η_1	0.4995	E_1	1 MPa	α_1	$211 \times 10^{-6}\ °C^{-1}$
r_2	$125\ \mu m$	η_2	0.452	E_2	1 GPa	α_2	$79.3 \times 10^{-6}\ °C^{-1}$

1.6 Results and Discussion

1.6.1 Heat Treatment Effect from Experimental Results

The spatially distributed Rayleigh frequency difference at each target temperature before and after heat treatment was measured along the tested single-mode optical fiber length through the cross-correlation strategy with respect to the previous temperature as shown in Figure 1.6. The negative (underneath the x-axis) and positive (above the x-axis) values represent heating and cooling processes, respectively. From Figure 1.6(a), the Rayleigh frequency differences are not the same at different temperatures. Generally, the Rayleigh frequency difference increases with the temperature. At 800 ℃, it decreases. Moreover, at lower temperatures (smaller than 400 ℃), the greatest Rayleigh frequency difference is observed during B-C, and it gradually decreases from the middle portion to the A or D point due to heat transfer. Note that the single thermocouple is at the center of the oven, while elsewhere the temperature is not well-recorded. This uneven Rayleigh frequency difference along the optical fiber is attributed to the uneven temperature distribution of the furnace during heat process. However, at higher temperatures (more than 600 ℃), the value in the middle portion is not greater than at the two sides. Since the uneven temperature distribution along the furnace still exists (i.e., highest in the middle portion and gradually decreasing outward), the trend is opposite of the lower temperatures because the optical fiber sensitivity reduces at higher temperatures (referred to as the optical fiber sensitivity stabilization process in the heat treatment). In other words, although the middle portion has a higher temperature, the smaller sensitivity leads to the Rayleigh frequency difference reduction

compared to the two sides with relatively higher sensitivity at lower temperatures. The lower values in the middle portion continue to be observed until 800 ℃. Generally, the Rayleigh frequency differences in the first heat process are not constant and stable. For the natural cooling process in Figure 1.6(a), the Rayleigh frequency difference gradually decreases as temperature decreases. For each temperature, a more even distribution can be observed when compared to the same temperature in the heat process. Two reasons might contribute to this difference. During the cooling process, the heat gradually escapes the ceramic tube to achieve a decrease in temperature. Once the temperature inside the ceramic tube decreases to the target temperature, the outside zone temperature is smaller than the ceramic temperature, and a relatively uniform temperature distribution is created in the cooling process. The other reason for a more even distribution is that the optical fiber temperature sensitivity remains stable after the heat treatment. Note that at 200 ℃, a slight frequency difference gradient might be related to the temperature distribution affected by the temperature magnitude, heat transfer distance, heat loss rate, and ceramic temperature properties.
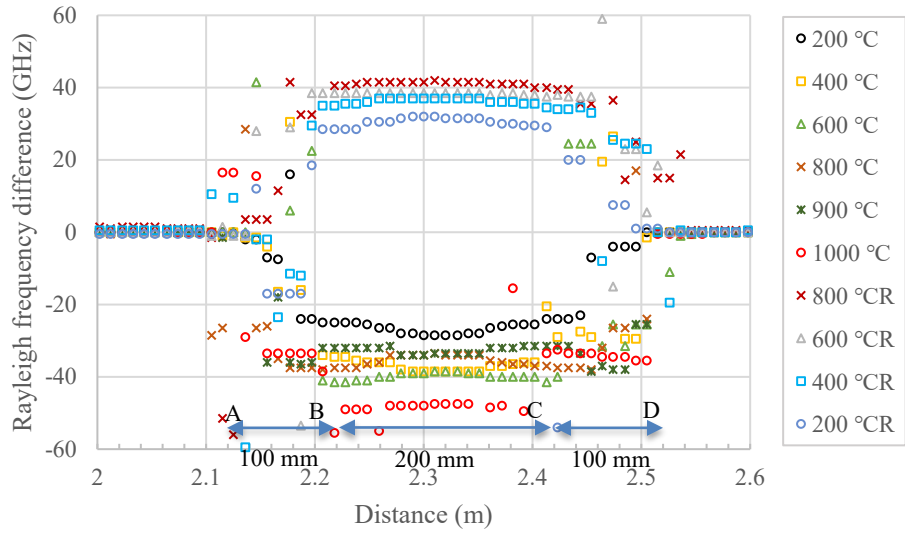
(a)
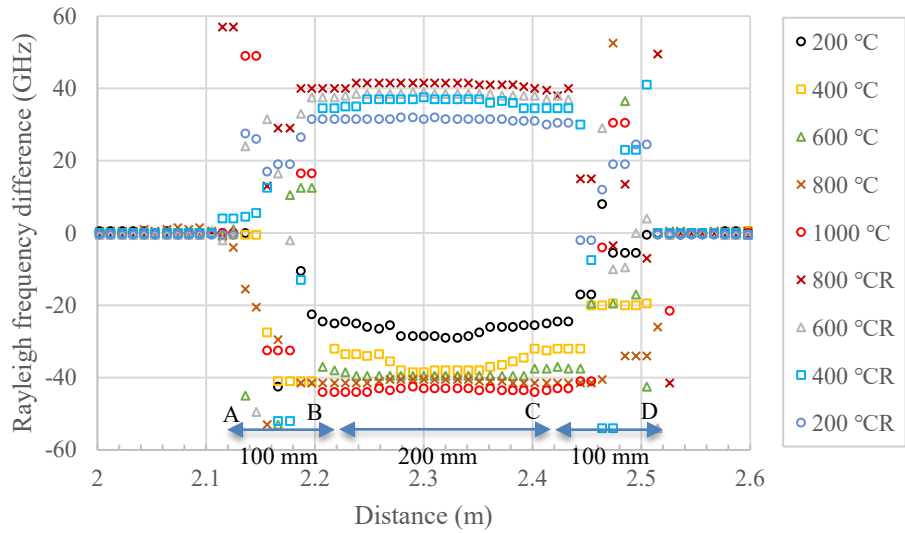
(b)

Figure 1.6 Representative spatial distributions of Rayleigh frequency difference along the optical fiber (a) before and (b) after heat treatment for case (1)

Figure 1.6(b) shows the Rayleigh frequency differences along the optical fiber subjected to heat treatment. Again, the heating and cooling process results are presented. For the heating process, the frequency in the middle portion is not significantly lower than the two sides at 800

°C, which is different from the first heating process in Figure 1.6(a) since the temperature sensitivity change of the optical fiber is complete, and the heat treatment has enhanced the stability of the optical fiber for Rayleigh scattering based temperature measurement. For the second cooling process, the Rayleigh frequency difference distributions are more uniform and stable than those in the first cooling process. The nonlinear relationships between the Rayleigh frequency and corresponding temperature are established and plotted in Figure 1.7. Figure 1.7(a) and (b) show the Rayleigh frequency-temperature curves before and after the heat treatment. The Rayleigh frequency curves in the first heat process show deviations near 800 °C and some frequency fluctuations can be observed at 1000 °C in Figure 1.7(a). Also, the Rayleigh frequency curves of different temperature increments show slight deviations. However, a stable Rayleigh frequency curve in the first cooling process can be fitted by a parabolic equation with a determination coefficient of $R^2 = 1.000$. Figure 1.7(b) shows the Rayleigh frequency curves after the heat treatment. It is found that regardless of temperature increments, the Rayleigh frequency curves in the heating and cooling processes are reasonably overlapped. Moreover, the curves of different temperature increments are in excellent agreement when the fitted equations are compared (each equation fitted by all heat and cool data with $R^2 = 1.000$). The maximum difference of the second term coefficient for the three equations as indicated in Figure 1.7 is no more than 0.5%.
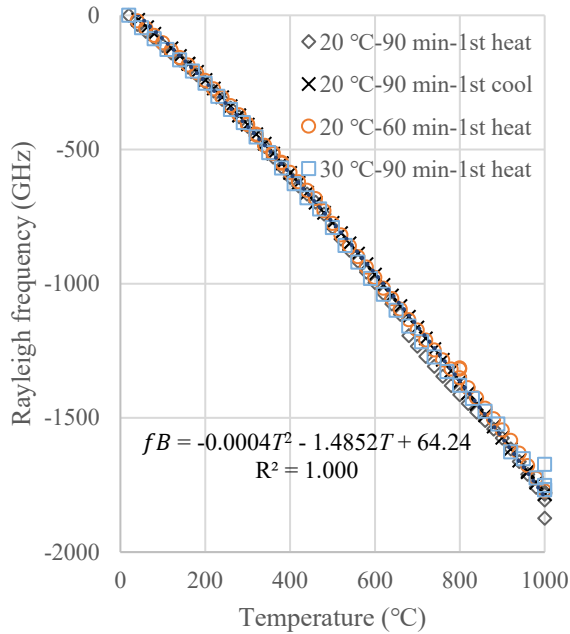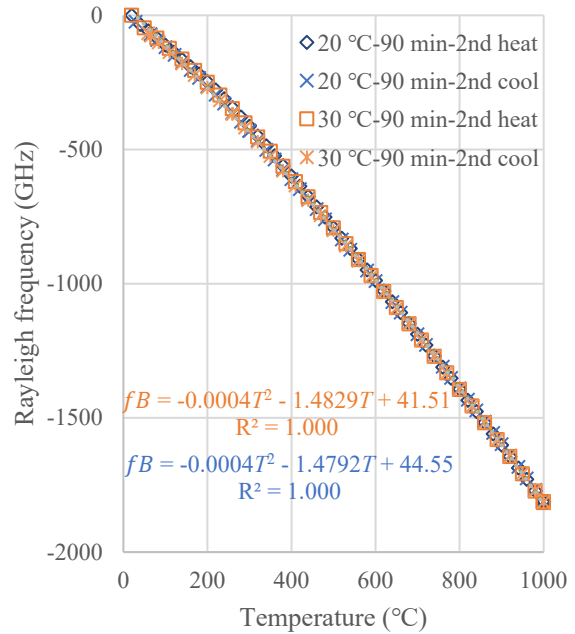
(a)   (b)

Figure 1.7 Rayleigh frequency changes: (a) before heat treatment from 20 to 1000℃ (b) heat-cool processes from 20 to 1000℃ after heat treatment

1.6.2 Coating Effect from Theoretical, Numerical and Experimental Results

Figure 1.8(a) shows the numerical normal strains of the three components along the optical fiber subjected to a temperature increment of 1 ℃ at room temperature. The largest differences among the three components can be observed at the ends while the normal strains are equal at 2.18 $\mu\varepsilon$ in the middle portion. This numerical value is very close to the analytical value of 1.78 $\mu\varepsilon$. The same numerical calculation was conducted when the temperature was about -53 ℃ as shown in Figure 1.8(b). Again, the numerical normal strain of 8.61 $\mu\varepsilon$ is very close to the analytical normal strain of 7.41 $\mu\varepsilon$. The increasing normal strain at about -53 ℃ is mainly attributed to the stiffer inner coating at low temperatures (Young's modulus increasing by three-order of magnitude), as compared to the normal strain at room temperature. Therefore, the finite

19

element model developed in the present study is accurate in the prediction of the thermal-induced strains of the fiber glass, inner coating, and outer coating. The effect of the coatings on the thermal response of fiber optic sensors can be simulated at different temperatures if the temperature-dependent material properties of the three components are accurately determined before these polymer coatings soften and melt away.

(a)

(b)
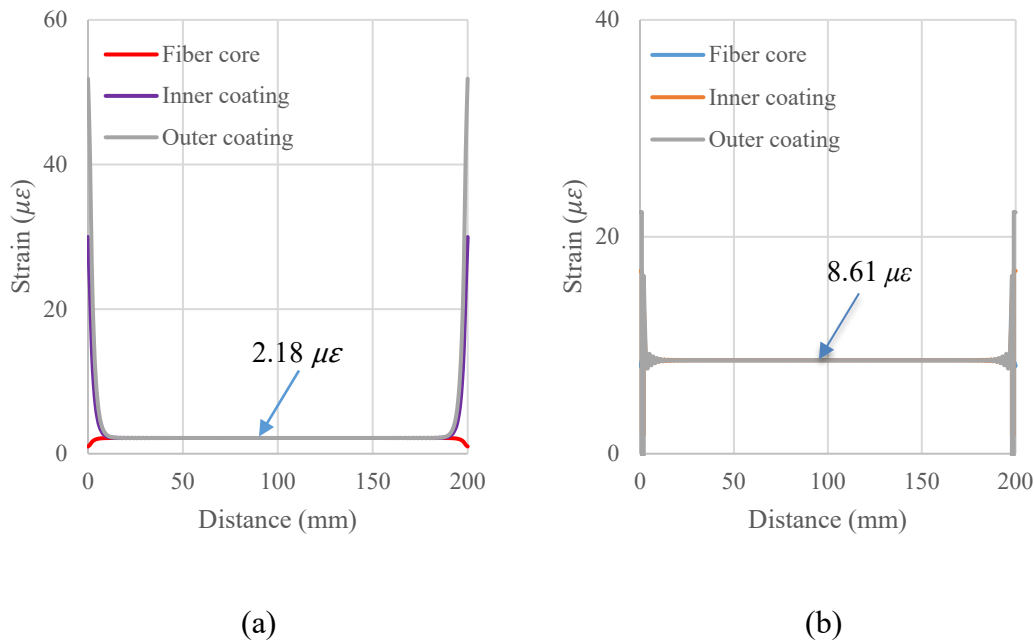
Figure 1.8 Finite element modeling results subjected to temperature increment of 1℃ (a) at room temperature (b) at about -53 ℃

The comparison between the numerical and experimental results give insight into the coating effect on the temperature sensitivity of the optical fiber. Figure 1.9 shows the Rayleigh frequency-temperature curves between room temperature and 200 ℃ with temperature increments of 30 ℃ and 20 ℃ extracted from the experimental results. Both the first and second heat results are presented, representing the optical fiber with and without coatings, respectively, since the coatings subjected to the heat treatment melted away. Another group of the optical

fibers in which the coating were stripped off in advance were tested, namely 20 ℃ (no coatings)

and 30 ℃ (no coatings). The fitting equations for each group of data are presented. There are

slight differences in the temperature coefficients between the temperature increments of 20 ℃

and 30 ℃. The second heat results differ from the first, probably due to the heat treatment effect,

although both do not have coatings. Comparing first case results with the results without coatings

(i.e., 20 ℃ or 30 ℃- no coatings) showed that the temperature coefficients increased by -0.0229

GHz/℃ and -0.0185 GHz/℃ for temperature increments of 20 ℃ and 30 ℃, respectively. These

differences are attributed to the additional thermal-induced strains on the fiber core. If the strain

sensitivity (S_T^R) of the fiber core is -6.9498 $\mu\varepsilon$/GHz, the average thermal-induced strains due to

different thermal expansion coefficients from 20 ℃ to 200 ℃ are 0.159 $\mu\varepsilon$ and 0.129 $\mu\varepsilon$,

respectively. These values are small, and different from the numerical results at room

temperature and in the cryogenic environment. This is because the material properties change at

high temperatures. However, the temperature-dependent material properties are not identified

due to the difficulty of testing these polymer coatings with complicated compositions at high

temperatures. Although a previous study (Lu et al. 2018) demonstrated the temperature

sensitivity improvement in Rayleigh distributed sensing at low temperatures, the sensitivity at

high temperatures is enhanced in the present study. This conclusion is like the small temperature

coefficient change of the Rayleigh scattering signature after the first thermal treatment (up to 150

℃) for a single-mode optical fiber without coatings ($S_T^R = (6.75 \pm 0.02) \times 10^{-6}$/℃) and a single-

mode optical fiber with a high temperature acrylate coating ($S_T^R = (6.72 \pm 0.02) \times 10^{-6}$/℃)

(Rizzolo et al. 2016).
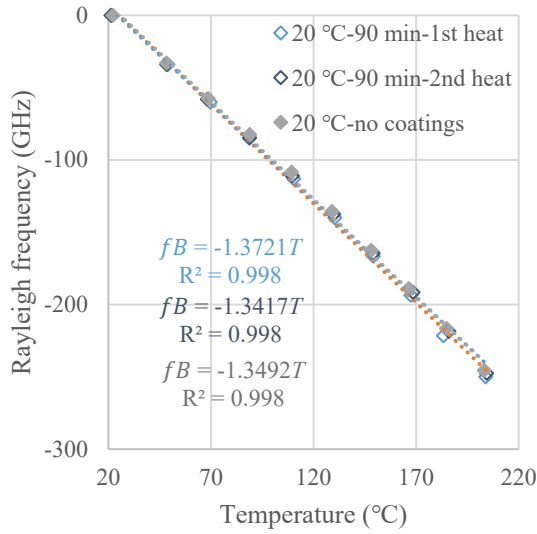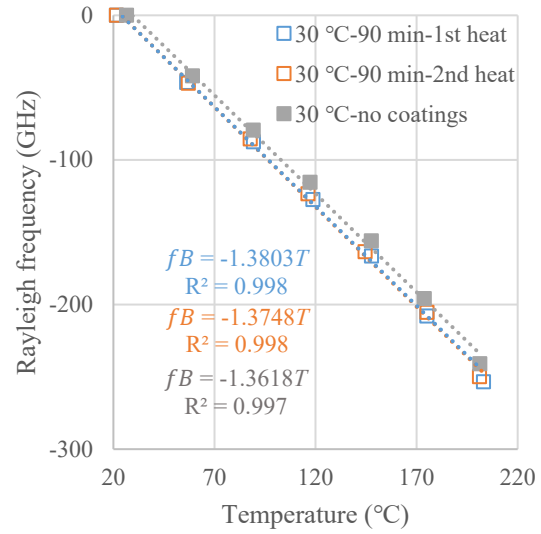
Figure 1.9 Rayleigh frequency-temperature curves before 200 ℃ with temperature increment of (a) 20 ℃ (b) 30 ℃

1.7 Parametric Studies

To provide design suggestions for the Rayleigh-scattering-based distributed fiber optic temperature sensors, parametric studies were performed to investigate the effect of the material and geometrical properties of the coating layers on the thermal-induced fiber core strain. Since the numerical model has been validated by the theoretical results, different numerical models with different parameters were established and the basic case for comparison was the parameters at room temperature. The temperature increment of 1 ℃ was applied as the load in the numerical models.

The theoretical analysis indicates that the shear strain transfer between the adjacent coating layers is influenced by the elastic moduli of the materials (Wang and Dai 2019). Typical elastic moduli are considered for inner (E_1) and outer (E_2) coatings and fiber glass core (E_0) in the parametric studies. Figure 1.10 shows the effect of elastic moduli on the fiber core strain. The

22

elastic modulus of fused silica is slightly temperature dependent, between 72 and 80 GPa. This

can be seen from the results in [22]. The fiber core strain slightly and linearly decreases with the

E_0 in Figure 1.10(a). Both the E_1 and E_2 show significant effect on the fiber core strain, and their

linear slopes show a decreasing trend with elastic moduli. At 10 GPa, the fiber core strain in

Figure 1.10(b) is about three times that in Figure 1.10(c).

(a)   (b)   (c)
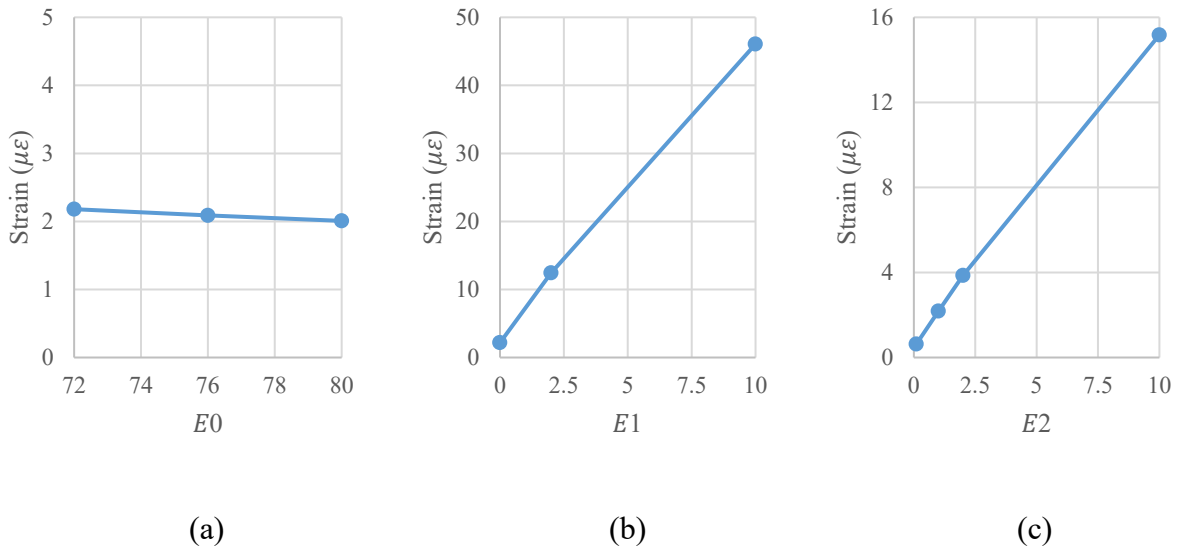
Figure 1.10 Effect of elastic moduli (unit: GPa) of (a) fiber core (b) inner coating (c) outer coating on the fiber core strain

Figure 1.11 shows the thermal expansion coefficients of fiber core (α_0) and inner (α_1)

and outer (α_2) coatings effects on the fiber core strain. The fiber core strain linearly increases

with α_0, while it linearly decreases with α_1. In addition, the fiber core strain significantly

increases with α_2, which is different from α_1.

Figure 1.12 shows the Poisson ratios of fiber core ($\eta 0$) and inner ($\eta 1$) and outer ($\eta 2$)

coatings effects on the fiber core strain. Clearly, the Poisson ratios of the $\eta 0$ and $\eta 1$ show

negligible effect on the fiber core strain. The optical fiber core shows a decreasing trend with the

Poisson ratio of $\eta 2$.

(a)   (b)   (c)
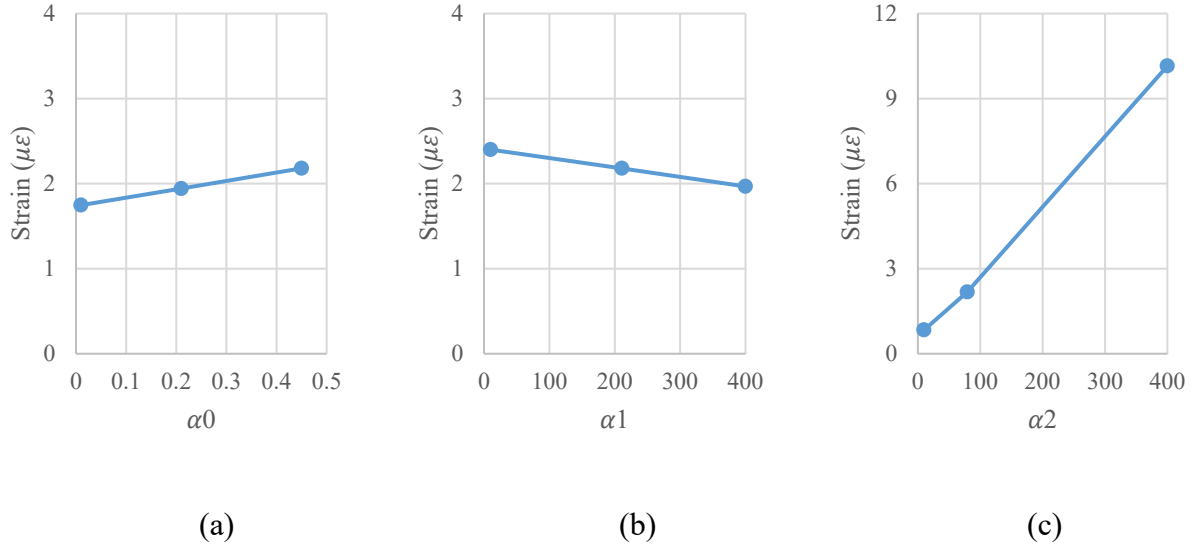
Figure 1.11 Effect of thermal expansion coefficients (unit: ×10-6) of (a) fiber core (b) inner coating (c) outer coating on the fiber core strain

(a)   (b)   (c)
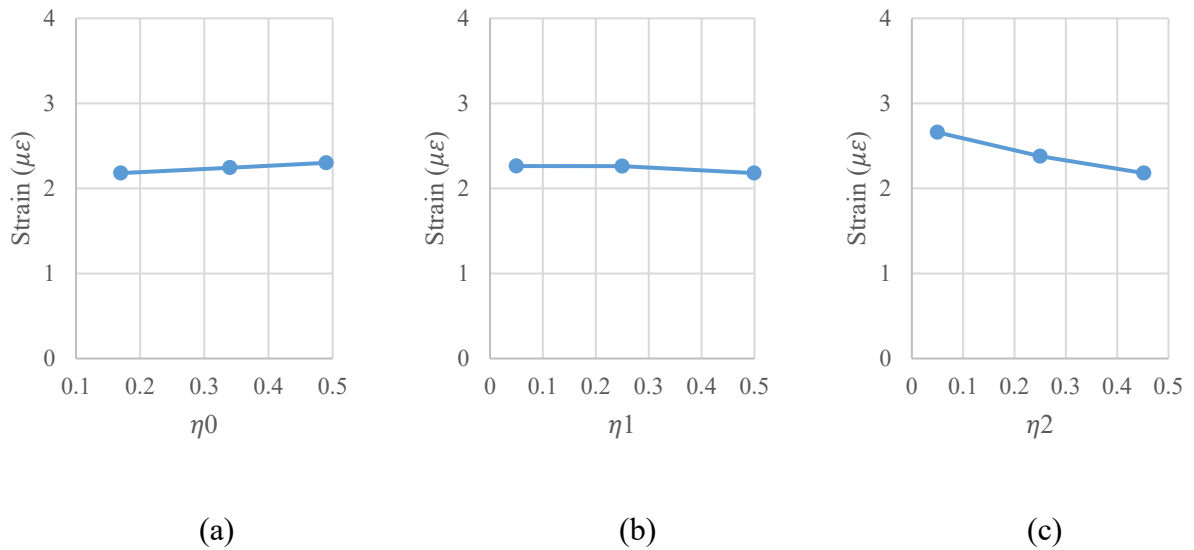
Figure 1.12 Effect of Poisson's ratios of (a) fiber core (b) inner coating (c) outer coating on the fiber core strain

Figure 1.13 shows the effect of inner (r1) and outer (r2) coatings radii as well as number of coating layers on the fiber core strain. Both radii of inner and outer coatings considered here range within 1000 μm. As the r2 radius increases, the outer radius (i.e., the thickness) of the outer coating increases to the pre-set value. However, as the outer radius of the inner coating increases to the pre-set value, the inner radius of the outer coating is equal to the outer radius of the inner coating in the parametric studies. To investigate the effect of the number of coating layers, a third layer is considered in addition to the previous two layers to mimic the practical application of an optical fiber with a tight buffer. This buffer layer has a radius of 450 μm, while its elastic modulus, thermal expansion coefficient, and Poisson ratio are 0.55 GPa, $160 \times 10\text{-}6$ /°C, and 0.47, respectively (Gu et al. 2013). The increasing r1 and r2 show significant effect on the fiber core strain, especially r2, as shown in Figure 1.13(a) and (b). In addition, an extra layer of the tight buffer can induce fiber core strain to about 44 $\mu\varepsilon$, which needs attention in the fiber optic temperature sensor calibration since this additional strain enhances temperature sensitivity.
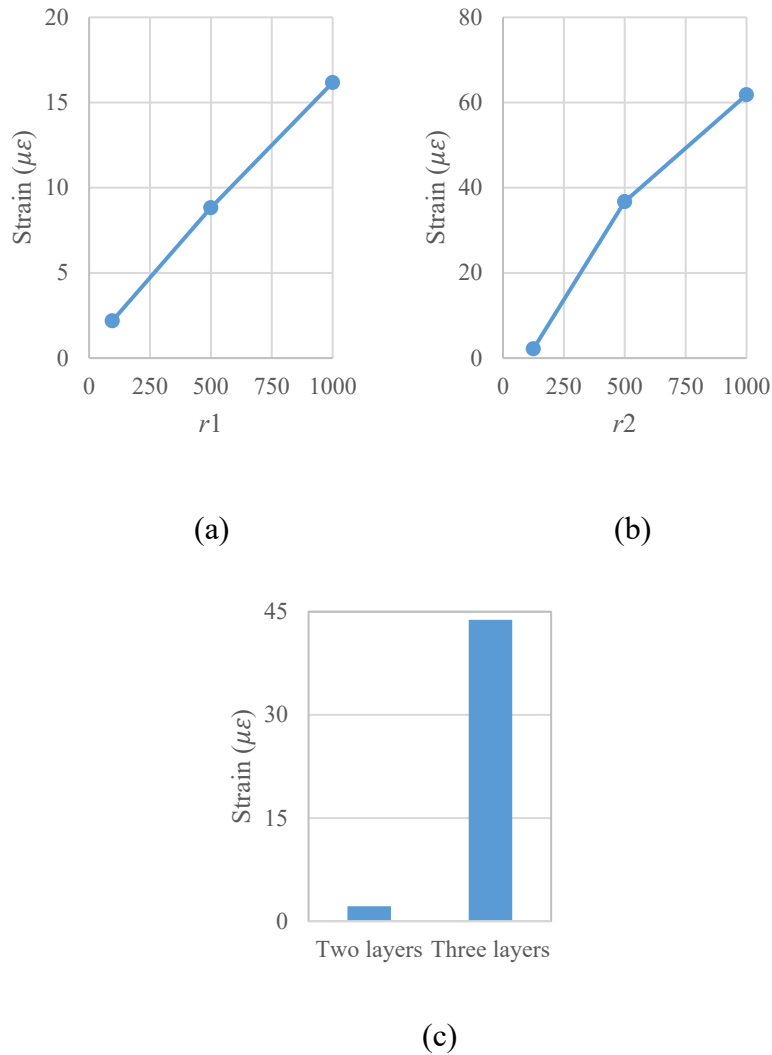
Figure 1.13 Effect of radii of (a) inner coating (b) outer coating, (c) layers on the fiber core strain

1.8 Summary

The present study experimentally investigates the effect of heat treatment on the Rayleigh-scattering-based temperature measurement up to 1000 ℃. In addition, the typical coating effect on the fiber core strain at high temperatures is identified through the theoretical and numerical analysis. The validated finite element model is used to perform parametric studies

that design coating layers (i.e., material properties and geometric parameters) for the fiber optic sensors to measure high temperatures. Several conclusions can be drawn as follows.

- One-time heat treatment can successfully eliminate the hysteresis effect and Rayleigh-frequency temperature change becomes stable up to 1000 ℃, which enables the reliability of the Rayleigh scattering based temperature measurement. Moreover, regardless of temperature increments in the heat treatment process, a unified parabolic equation (with R^2 more than 0.999) is fitted for the measured Rayleigh frequency and temperature relationship of the fiber optic temperature sensors after the heat treatment. The sustained time at the peak temperature does not significantly change the Rayleigh-frequency measurement.

- The established finite element three-layer model for calculating fiber core strains due to the thermal dilation of the coatings subjected to thermal load shows high accuracy, as compared to the theoretical values. The numerical fiber core strain at room temperature becomes the upper limit, as compared to the experimental values before 200 ℃. The typical dual-layer-coating-induced fiber core strain (smaller than 1 $\mu\varepsilon$) at high temperatures can be neglected.

- From parametric studies, most material properties and geometric parameters are linearly related to the fiber core strain. Among them, both elastic moduli and radii of inner and outer coatings as well as the outer coating thermal expansion coefficient show significant sensitivity on the fiber core strain, which must be considered for the temperature sensitivity calibration of the fiber optic sensors. An additional tight buffer layer can induce fiber core strain of about 44 $\mu\varepsilon$.

Chapter 2 Rayleigh Scattering Based, Thermal-induced Displacement Measurement along a Steel Plate at High Temperature

2.1 Introduction

Crack, strain, displacement, and temperature are basic parameters in the evaluation of functionality, safety, and stability of engineering structures (Zhang et al. 2020, 2021). Various measurement methods have thus been developed to monitor the change in these parameters based on their working principles (e.g., physical, chemical, electric, magnetic, and mechanical), complexity, cost, and application ranges and limitations. In civil engineering, the most common measurement tools are strain gauges and dial gauges for displacement and thermocouples for temperature (Gagliardi 2010). In each application, a large quantity of gauges or thermocouples are often required especially in a large-scale test, and they may not survive the harsh condition during a fire.

Fiber optic sensors are an alternative for an effective measurement of these quantities because of their compactness, immunity from electromagnetic interference, and high temperature and radiation resistance (Petrie et al. 2019). In general, Brillouin, Rayleigh, and Raman scatterings provide different opportunities for spatially distributed temperature and strain measurements (Bao and Chen 2012) at a spatial resolution in centimeters. North America has the largest market share in the distributed fiber optic sensor market because of their new technologies in distributed networks, major companies, and many oil and gas pipeline projects (Research and Markets 2022). Although the high cost of distributed fiber optic sensor systems prevents its wide application in the civil engineering field, there is a growing demand for a data-based analysis and high, long-term benefits in infrastructure operation protection (such as the pipeline and offshore industry) and asset management from distributed fiber optic sensors. Although deployment and installation of distributed fiber optic sensors is challenging since it is

still a contacted measurement tool, these distributed sensing technologies can collect a large quantity of data points both spatially and temporally once deployed, which is quite attractive for monitoring and assessing large-scale engineering structures. It is difficult to visually identify the unwarned initiation of any failure or failure location of structures (such as leak detection). The distributed fiber optic sensors can provide the required data to develop a decision for timely maintenance before the function and service of the structures have been lost at failure states (Choi and Kwon 2019).

However, distributed fiber optic strain sensing requires adequate strain transfer between the optical fiber and its host material (Ansari and Yuan 1998). At ambient temperatures, many studies have been conducted to understand the strain transfer mechanisms both experimentally and theoretically (Wang and Zhou 2014, Wang and Xiang 2016, Wang et al. 2018, Wang and Dai 2019, Yuan et al. 2003, Kishida et al. 2014, Bastianini et al. 2019). Among the theoretical derivations, one assumption commonly used is the perfect bond between the optical fiber and the host material. While acceptable under ambient conditions, this assumption is questionable at high temperatures since the fiber optical sensor itself and the strain transfer mechanism must survive harsh environments. Limited studies have been conducted to understand strain sensing effectiveness below 60 ℃ (Wang et al. 2018, Yang et al. 2021). Although temperature-dependent properties (such as elastic modulus and thermal expansion coefficient) of three-layer optical fiber sensors were considered (Yang et al. 2021), a perfect bond was still assumed. Therefore, the understanding of potential debonding of fiber optic sensors from their host materials at high temperatures is still lacking (Kishida et al. 2014, Zhu et al. 2019, Kishida et al. 2012, Bao and Chen 2016b).

In recent years, high temperature and thermal-induced strain in concrete and steel members under fire conditions have been measured successfully from their effects on Brillouin scattering along a bare single-mode optical fiber (Bao and Chen 2016b). Their measurement accuracies with Neubrescope NBX-7020 (Neubrex Co., Ltd., Japan) can potentially be improved by approximately seven times in temperature and 15 times in strain using Rayleigh scattering. However, the minimum measurement time required for stabilized Rayleigh scattering is approximately 12 times that for Brillouin scattering. This level of difference could lead to additional measurement variation even with a minor change in fire conditions over time. Therefore, the objectives of this study are to characterize the effect of polymer sheath on a distributed optical fiber sensor as the polymer experiences softening and melting at elevated temperatures, and to quantify the improvement in measurement accuracy based on Rayleigh scattering under a heating-holding load protocol. A single-mode optical fiber coated with a polymer sheath is divided into two segments for distributed temperature and thermal-induced strain measurements when loosely attached and firmly bonded to a steel plate, respectively. The two segments as distributed sensors are placed inside a high temperature furnace. The upper-bound temperature for effective thermal-induced strain measurement is identified. With a clear understanding of optical fiber bonding mechanisms under various conditions, this study develops distributed, Rayleigh scattering based, fiber optic sensors for an accurate thermal displacement measurement in harsh environments.

2.2 Tunable Wavelength Coherent Optical Time Domain Reflectometry (TW-COTDR)

Rayleigh backscattering was first used to measure strains based on the Optical Frequency Domain Reflectometry (OFDR) (Froggatt and Moore 1998). To improve its sensing distance and accuracy, the random heterogeneity in glass density along an optical fiber core was considered in

a refractive index fluctuation function as observed from the distribution of a random power spectrum of coherent OTDR (COTDR) traces (Koyamada 1998). To implement the COTDR method in time domain, the tunable wavelength of a distributed feedback laser during frequency scanning can be used to calculate the power spectrum, which was referred to as TW-COTDR. Mathematically, this implementation procedure is equivalent to determining the impulse response of a pump light pulse along a single-mode optical fiber with a longitudinally distributed Gaussian white noise that represents the fluctuation of the fiber core density or refractive index. Figure 2.1 shows the Rayleigh scattering spectrum measured from a single mode optical fiber with a spatial resolution of 10 cm as a result of the fluctuation of fiber density. As seen in Figure 2.1, the signal magnitude (mag.) appears to be a periodical function of scanning frequency and time. The function depends upon the change in density of the optical fiber. The characteristics of this multi-peak function may be used to detect the change in environment surrounding an optical fiber through correlation analysis.
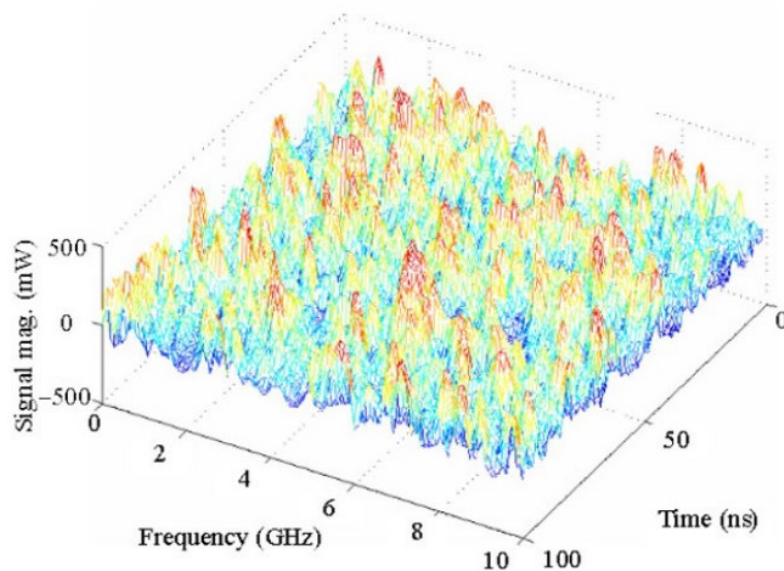

Figure 2.1 Rayleigh scattering spectrum

Rayleigh scattering is sensitive to strain and temperature changes as they modify the density of optical fiber. This modification is manifested in the linear frequency shift of a backscattered light. In comparison with Brillouin scattering, the Rayleigh scattering-based measurement technique shows a higher spatial resolution and a higher sensitivity (Piccolo et al. 2019). In a single mode optical fiber, the Rayleigh scattering frequency shift (Δv_R) can be linearly related to the strain and temperature applied along the optical fiber:

$$\Delta v_R = C_{21}\Delta\varepsilon + C_{22}\Delta T \qquad\qquad (2.1)$$

where C_{21} and C_{22} are the strain-frequency and temperature-frequency coefficients associated with Rayleigh scattering, respectively.

In this study, an optical interrogator, Neubrescope NBX-7020, was used to measure Rayleigh scattering along a single-mode optical fiber using the TW-COTDR. Only one end of the fiber was connected to the interrogator during measurement. According to its manufacturer's technical specifications, the interrogator with an accuracy of 100 MHz in its laser source can achieve a precision of 0.5µε and 0.05ºC in strain and temperature measurements, respectively. This level of sensitivity is the same as would be obtained by Fiber Bragg Grating (FBG) sensors (Kishida et al. 2014). To maintain a good trade-off between measurement accuracy and acquisition duration, the following parameters were selected in the test setup of the TW-COTDR: measurement distance range of 50 m, sampling interval of 1 cm, spatial resolution of 2 cm, average count of 212, output probe power of 0 dBm, output pump power of 25 dBm, frequency range of 194,000-194,300 GHz, and frequency step of 500 MHz. The frequency range was selected to ensure that the measured frequency difference of interest would be detectable. The

cross-correlating two-by-two measurement approach (Piccolo et al. 2019) was adopted to increase measurement accuracy by correlating the current measurement with the immediately past reference (i.e., zero point). Due to the requirement for cross correlation between any two sequential measurements, the applied strain steps (several tens of microstrains) or temperature steps must be sufficiently small to ensure accurate measurement of a corresponding minimal frequency difference in Rayleigh scattering. The overall strain or temperature effect can be accumulated by summing all steps. When the strain difference exceeds 500 $\mu\varepsilon$, the cross correlation in the TW-COTDR is prone to fail as verified experimentally in this study.

2.3 Experimental Program

Figure 2.2 shows a single-mode optical fiber (Corning Company, USA) used in the present study. The optical fiber consists of a fiber core, cladding, inner coating, and outer coating with outside diameters of 8.2, 125, 190, and 242 μm, respectively. The soft inner coating protects the glass from mechanical impact and the stiff outer coating protects the glass from abrasion and environmental exposure. Each of the inner and outer coatings is comprised of complex material mixtures, such as monomers, oligomers, photoinitiators, and additives (Bao and Chen 2015).
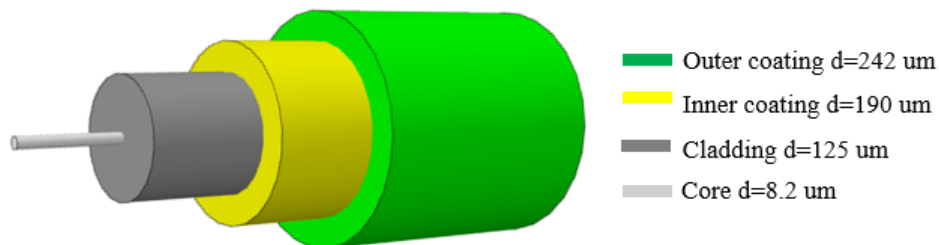

Figure 2.2 Single-mode optical fiber used in the present study.

2.3.1 Sensor Calibration Tests for Temperature and Strain Coefficients

Figure 2.3 shows the calibration test setup of an optical fiber for the determination of temperature and strain coefficients. While the top end of the test optical fiber was fixed to a grip on a load frame (INSTRON Model 5965), the bottom end of the fiber was restrained differently for temperature and strain measurements. In Figure 2.3(a), the bottom end of the fiber was free to expand when subjected to increasing temperature in the furnace. The applied temperature increment used in this study was 10 ℃, starting from the room temperature. Each increment was sustained for about eight min, including five min for rising to the temperature increment and a minimum of 2.5 min for each TW-COTDR measurement. Only the bottom end of the optical fiber was connected to the pump end on the interrogator. In Figure 2.3(b), the bottom end of the fiber was fixed to another grip of the load frame and moved with the load frame. At each target furnace temperature (i.e., 20, 100, 200, 300, 400, and 500℃), the optical fiber was subjected to a displacement applied and controlled by the load frame. The displacement-control loading was performed with a loading rate of 0.5 mm/min. The displacement and applied load were simultaneously measured and recorded by the internal extensometer and transducer of the load frame, respectively. Given an initial length of the optical fiber, the average strain in the optical fiber can be calculated by dividing the displacement increment (i.e., 0.1 mm) by the initial base length. Meanwhile, the Rayleigh frequency shift in the optical fiber caused by the strain increment was measured from the interrogator at each temperature. The measured Rayleigh frequency shift was then correlated with the strain obtained from the extension of the load frame to determine the frequency-strain coefficient at each temperature. Note that a protective sleeve with an inside steel bar, traditionally for fusion splicing of two glass fibers, was used to strengthen the gripping area of each optical fiber. Once gripped by the load frame, the sleeve can

prevent radial stress concentration from the applied grip force, reducing the possible damage of the fragile glass fiber.
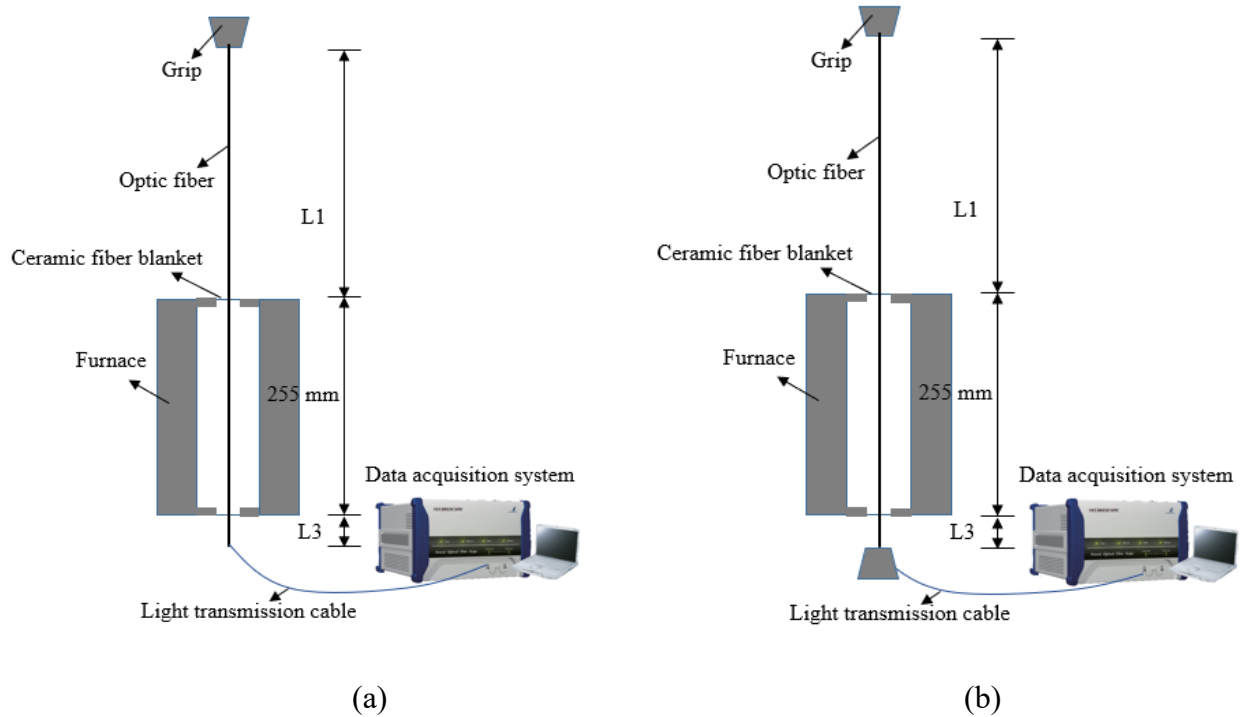
Figure 2.3 Calibration test setup: (a) for temperature coefficient, and (b) for strain coefficient.

2.3.2 Sensor Application Tests for Displacement Measurement at High Temperatures

Figure 2.4 shows the test setup for measuring the free thermal displacement of a cantilevered steel plate at elevated temperatures. The steel plate (ASTM A366 1008 steel) measures 600 mm long, 1 mm wide, and 20 mm high. The material properties as provided by the supplier includes 180-240 MPa in yield strength, 302-358 MPa in ultimate tensile strength, and 42-48% in elongation. The chemical composition of the steel is 99% iron, 0.08% carbon, 0.6% (max) manganese, 0.035% (max) phosphorus, 0.2% copper (min), and 0.04% sulfur.
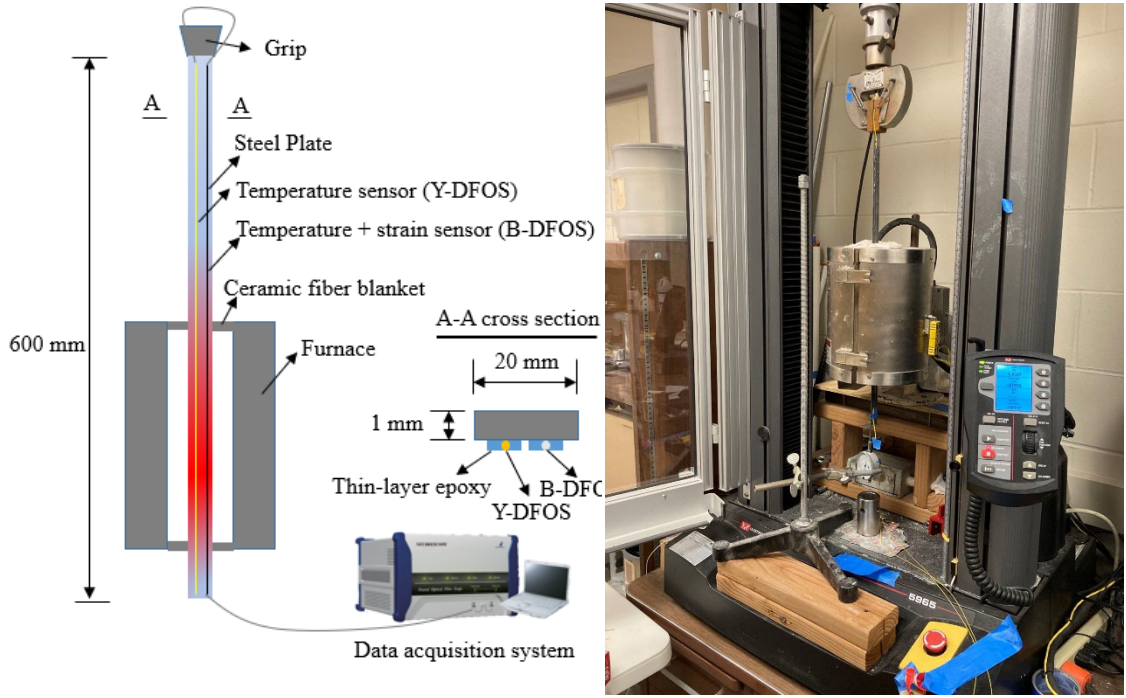
Figure 2.4 Steel plate test setup for free thermal displacement measurement: (a) schematic view, (b) specimen overview, (c) dial gauge installation

The same testing devices (such as furnace, load frame, and interrogator) as used in the calibration tests are adopted for the application test. Two steel plate samples were tested. The first steel plate was instrumented with one distributed fiber optic sensor (DFOS) with two

segments: Y-DFOS with a yellow sheath for temperature measurement and B-DFOS with the bare fiber as shown in Figure 2.2 for thermal-induced strain measurement. The second steel plate was instrumented with two B-DFOS sensors in parallel. The optical fiber for temperature measurement was placed into a sheath with a diameter of 1 mm. This sheath allowed the inside optical fiber to deform freely. Thus, the temperature sensor was free of strain at the ambient temperature. Note that the top end of the optical fiber outside the furnace was taped to the grip body to prevent the fiber from moving downward, which would otherwise cause notable fiber bending near the grip and affect the quality of light signals. Both the temperature sensor and the thermal-induced strain sensor were covered by steel reinforced two-part marine epoxy (Brand Name: J-B WELD), which served as a thin layer of bonding agents between the optical fiber and the steel plate. The basic properties of the epoxy were 34.6 MPa in strength, 4.6 h in set time, 15-24 h in curing time, and dark grey in cure color, as provided by the supplier. After 24 hours of curing to ensure the epoxy was hardened, the steel plate was tested in the vertically cantilevered form subjected to its own weight. The top end of the steel plate was gripped to the load frame. A dial gauge was affixed to a small piece of the bottom end of the steel plate with liquid glue as shown in Figure 2.4(c). The spring constant of 0.046 N/mm (Weiss 1938) of the spring-loaded dial gauge is smaller than the axial stiffness of the steel plate by five orders. The effect of the spring on the steel displacement is thus negligible. The dial gauge outside the furnace zone measured an axial displacement at different temperatures to serve as ground truth data for fiber optic sensor validation. Different target temperatures were applied by the furnace with the temperature controller. The temperature increments were set to 12 ℃ and 13 ℃, alternately, to ensure stable Rayleigh scattering signal with the TW-COTDR technology. Specifically, considering a temperature coefficient of -0.5758 °C/GHz and a strain coefficient of -6.997

37

µε/GHz to be determined in Section 4.1, a temperature increment of 13 °C corresponds to a

frequency change of -22.6 GHz for the temperature sensor, which is equivalent to a strain change

of 158.0 µε. In addition, the thermal strain of steel with an expansion coefficient of 12.6 µε /C at

13 °C increments is 163.8 µε. The total equivalent strain is 321.8 µε, which is less than 500 µε as

indicated in (Piccolo et al. 2019) and verified in this study. With a temperature increment of

20 °C in Rayleigh scattering, a temperature sensor works fine but a strain sensor fails to obtain

stable readings at high temperatures. The sustained time for each temperature increment was

approximately eight min, which included about fivemin to complete the temperature rise and

about 2.5 min for the TW-COTDR measurement. The temperature was increased from the

ambient temperature (20 ℃) to 405 ℃. Ceramic fiber blankets were used to seal both the top and

bottom openings of the furnace to reduce the loss of heat.

2.4 Results and Discussion

2.4.1 Determination of Temperature and Strain Coefficients

Figure 2.5 shows representative Rayleigh frequency differences measured along a fiber

optic sensor at applied temperatures and zero strain and another fiber optic sensor at the ambient

temperature and applied displacements (i.e., proportional to strains) when the cross-correlation

based TW-COTDR technique was used. As indicated in Figure 2.5(a), the temperature sensor

extends from approximately 2.7 m to 3.1 m. The sensor measures approximately constant

temperature increments in the center portion inside the furnace. Towards the two ends of the

furnace, however, the sensor measurement becomes sporadic likely due to heat exchange with air

outside the furnace through the top and bottom openings, though sealed to the extent possible.

The extent for the constant temperature measurement decreases with the applied temperature.

As indicated in Figure 2.5(b), the strain sensor portion has a distance mark of the fiber from approximately 2.4 m to 3.1 m. Excessive differences corresponding to several tens of microstrains are observed at the two ends of the sensor likely due to the grip force applied during the strain calibration tests. Otherwise, the Rayleigh frequency difference is uniform in the middle portion of the optical fiber and the differences between two sequential tests are small as a result of the 0.1 mm displacement increment applied in every step. Moreover, this technique has high sensitivity and accuracy as shown from the Rayleigh frequencies under 1.02 mm and 1.1 mm displacements in Figure 2.5(b).
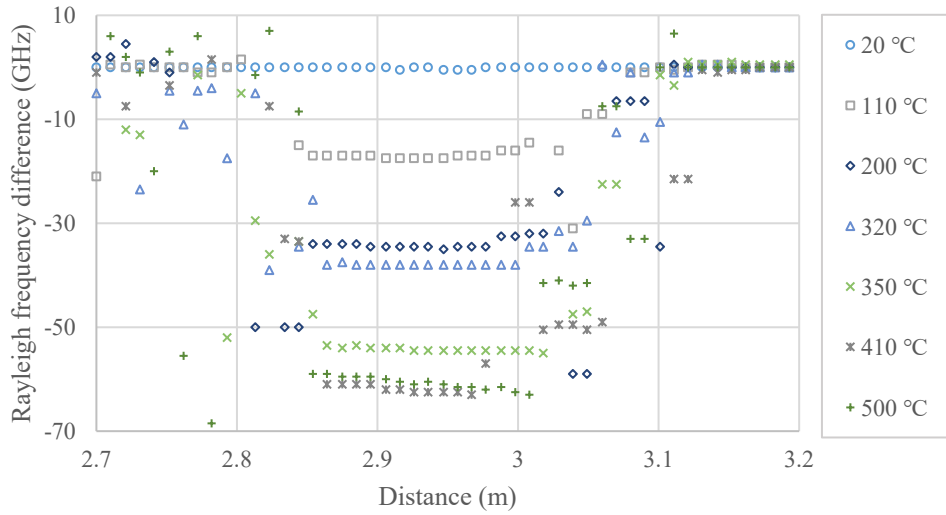
(a)
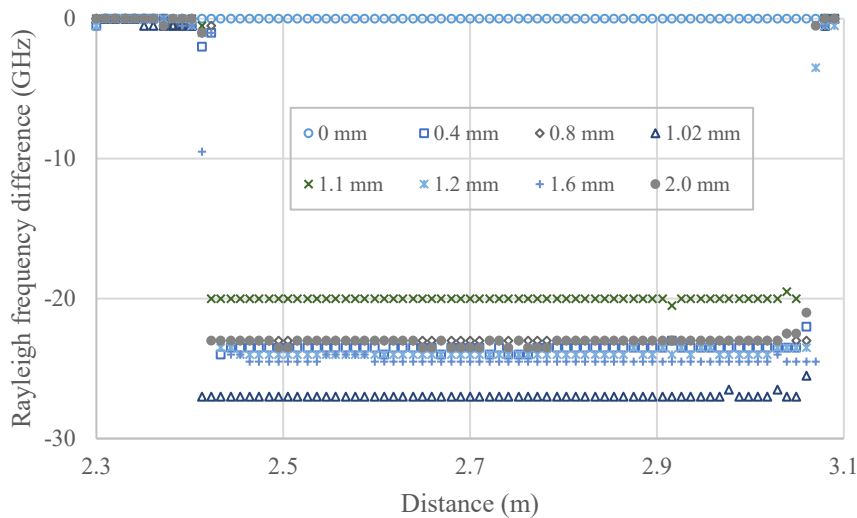
(b)

Figure 2.5 Representative Rayleigh frequency differences along an optical fiber: (a) applied temperatures and zero strain, and (b) applied displacements and ambient temperature.

In comparison with Brillouin scattering (Bao and Chen 2016b), Rayleigh scattering responds to temperature and strain effects quite differently. The distribution of Rayleigh frequency difference along the optical fiber for strain measurement as shown in Figure 2.5(b) is

as accurate as that of Brillouin frequency in terms of measurement deviation from its targeted

value (constant strain in calibration tests). However, for temperature measurement as shown in

Figure 2.5(a), the spatial distribution of Raleigh frequency difference has a significantly larger

fluctuation than that of Brillouin frequency. This is mainly because Rayleigh scattering is six

times more sensitive than Brillouin scattering and takes 11 times longer than Brillouin scattering

to complete each measurement of temperature distribution. At the same time, the heat flow near

the top and bottom openings of the furnace generates high-frequency vibration of the optical

fiber during the measurement. As clearly indicated in Figure 2.5(a), the Rayleigh frequency

difference is generally uniform in the center portion of the furnace.

Figure 2.6(a) and Figure 2.6(b) show relationships between the Rayleigh frequency shift

and temperature and between the Rayleigh frequency shift and strain at different temperatures,

respectively. The average Rayleigh frequency difference (x) along the optical fiber inside the

furnace was used and related to the applied temperature (y) in Figure 2.6(a). This linear

relationship has a slope of -0.5758 ℃/GHz, which represents the frequency-temperature

coefficient of the optical fiber as shown in equation (1.1). The coefficient of determination for

the linear regression is 0.999, indicating a good representation of the test data. Figure 2.6(b)

shows several linear relationships between the frequency (x) and strain (y) at different applied

temperatures. The slopes of all the linear relationships, called strain coefficients, are presented in

Figure 2.7. The slope values were close, except for 300 ℃ when the coating of the optical fiber

experienced melting and caused uncertain bonding conditions with the fiber. For simplicity, this

study used an average (constant) strain coefficient of

-6.997 $\mu\varepsilon$/GHz as indicated in Figure 2.7. The coefficient of determination (R^2) from all the calibration test data points in Figure 2.6(b) is 0.983, which indicates a strong linear correlation between the applied strain and the Rayleigh scattering frequency.
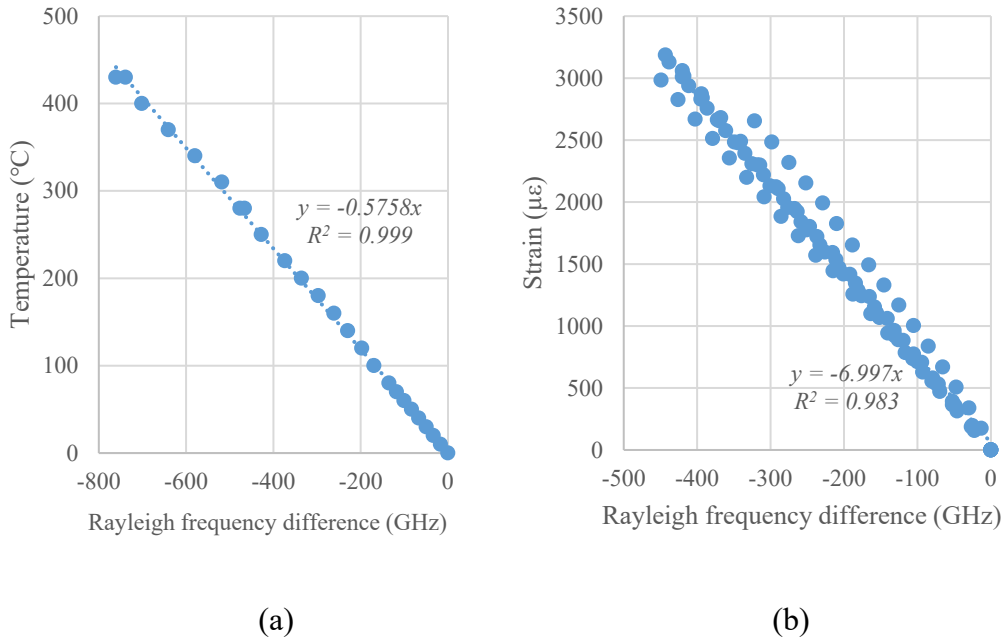

Figure 2.6 Temperature and strain as a function of Rayleigh frequency shift: (a) temperature, and (b) strains at different temperatures.
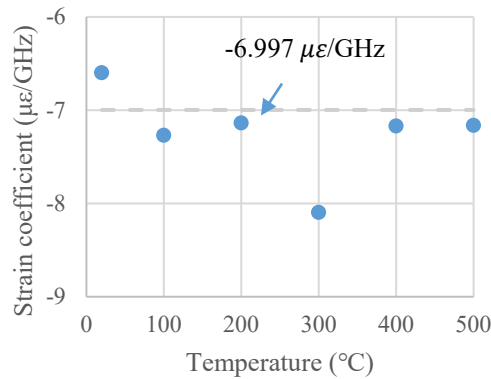

Figure 2.7 Variation of strain coefficient with the applied temperature.

2.4.2 Rayleigh Scattering Based Calculation

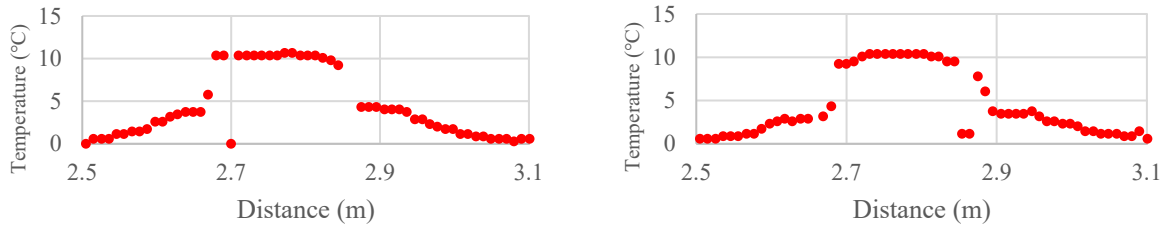2.4.2.1 Measured temperature distribution

Figure 2.8 shows Y-DFOS-measured temperature distributions of the heated steel plate at different applied temperatures. The Y-DFOS temperature sensor between 2.5 m and 3.1 m along the optical fiber was verified to be free of strain at the ambient temperature by pulling the fiber out of the sheath with a negligible force. These temperature distributions were calculated by multiplying the Rayleigh frequency difference (negative value) by the frequency-temperature coefficient (-0.5758 ℃/GHz). Obviously, the temperature distribution was not uniform along the steel plate, which is usually neglected in the literature when thermocouples are used to measure temperatures at discrete points. As shown in Figure 2.8, each temperature distribution consists of one central region located inside the furnace and two transition regions towards the two ends and further outside of the furnace. Although the central region shows an overall uniform temperature distribution, the gradually decreasing trend is clearly seen towards the two ends due to air circulation. When ignored, the missing transition regions would result in an underestimated displacement at the free end of the steel plate. When the maximum temperature at the center of the furnace is assumed over the entire length of the heated zone or the height of the furnace, the thermal displacement would be overestimated. Therefore, the optical fiber sensor Y-DFOS is a practical tool to measure temperature distribution, which is beneficial in performance-based fire design of engineering structures.
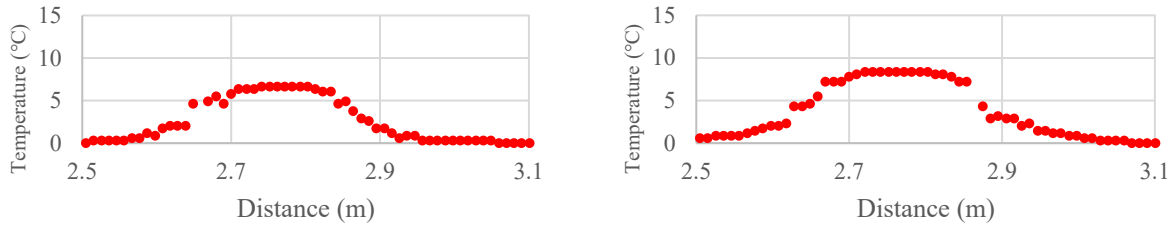
(a) 30 and 40 ℃
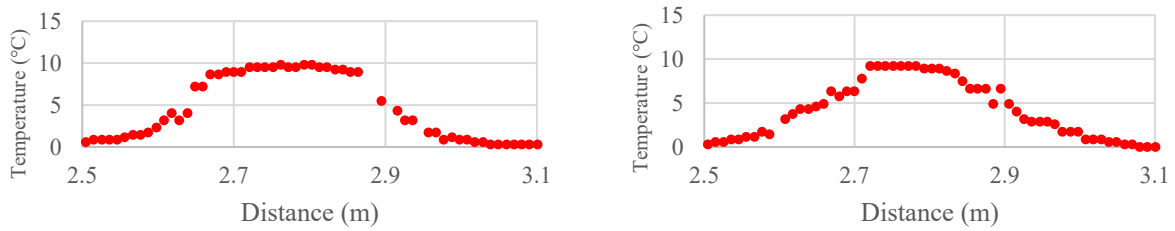
(b) 55 and 67 ℃

(c) 80 and 92 ℃
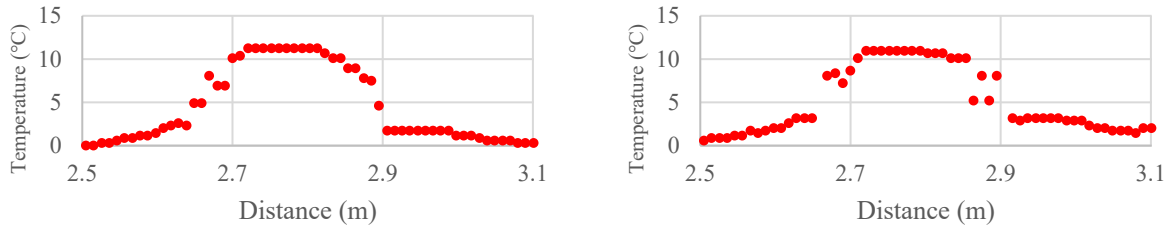
(d) 105 and 117 ℃

Figure 2.8 Temperature distribution along the steel plate at elevated temperatures
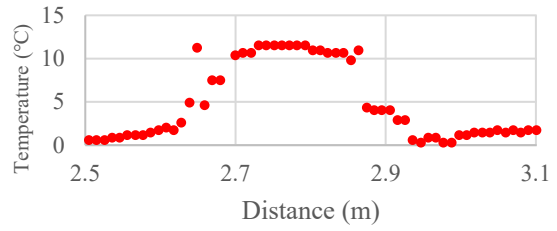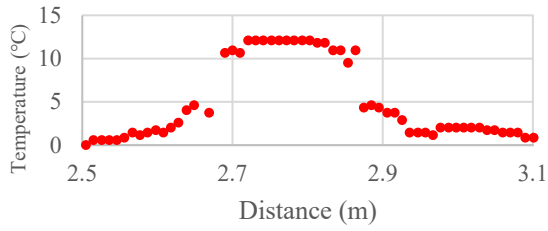
(e) 130 and 142 ℃
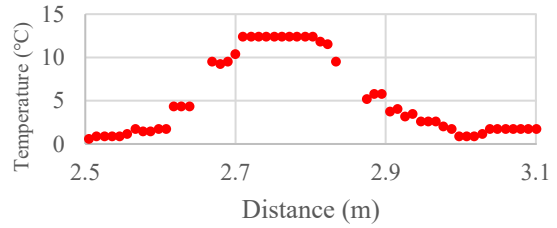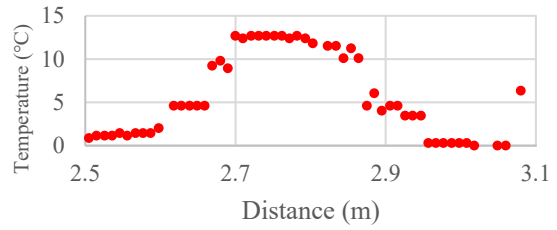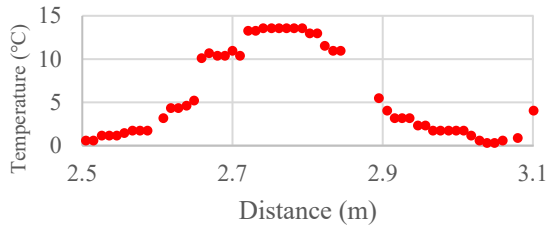
(f) 155 and 167 ℃

(g) 180 and 192 ℃

(h) 205 and 217 ℃

Figure 2.8 cont. Temperature distribution along the steel plate at elevated temperatures
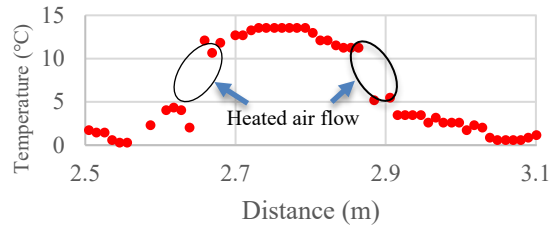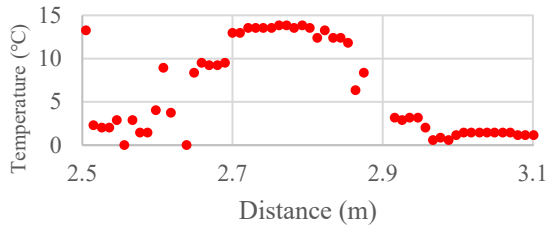
(i) 230 and 242 ℃
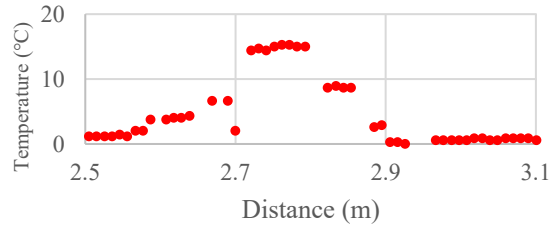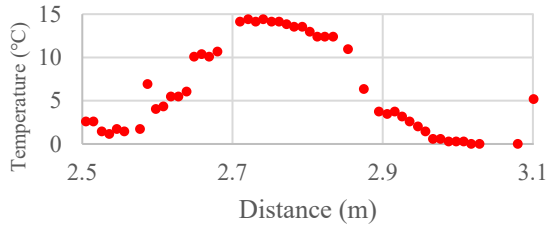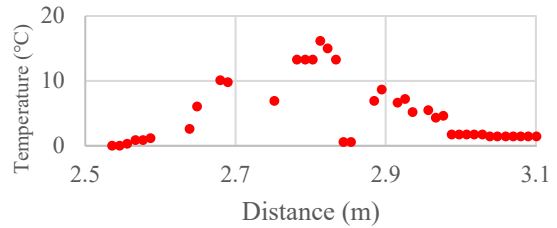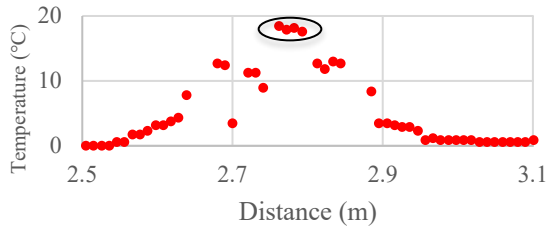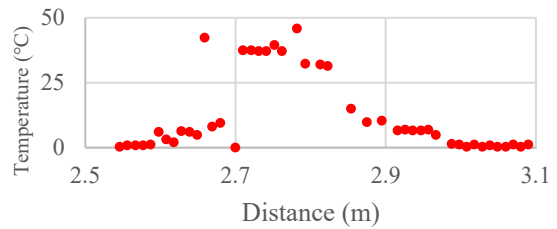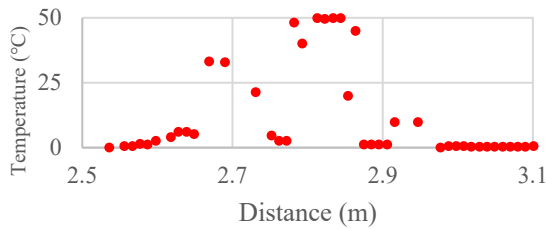
(j) 255 and 267 ℃

(k) 280 and 292 ℃

(l) 305 and 317 ℃

Figure 2.8 cont. Temperature distribution along the steel plate at elevated temperatures
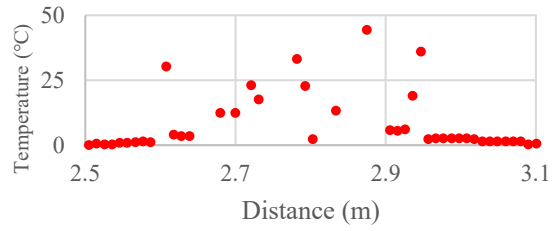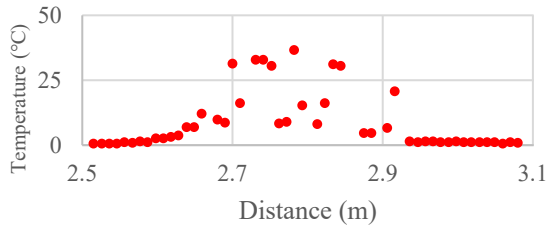
(m) 330 and 342 ℃
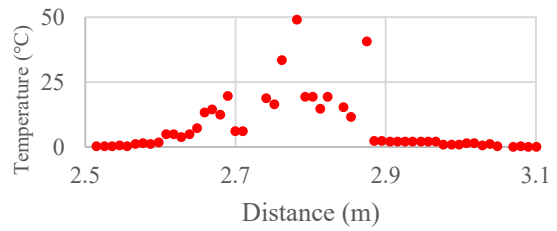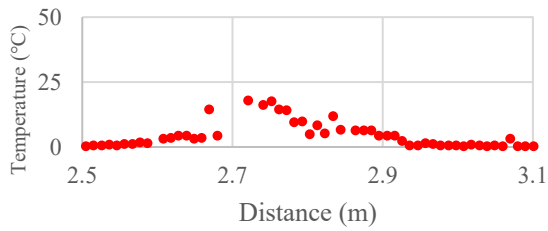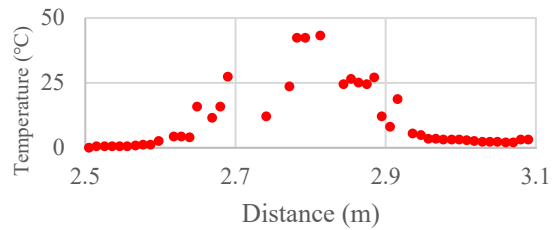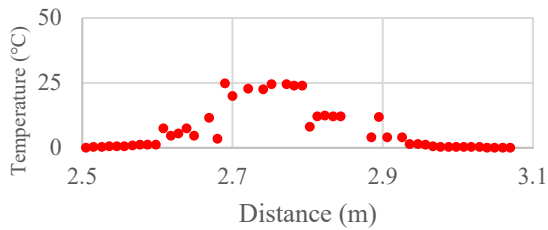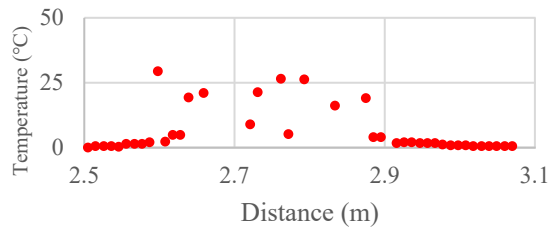
(n) 355 and 367 ℃

(o) 380 and 392 ℃

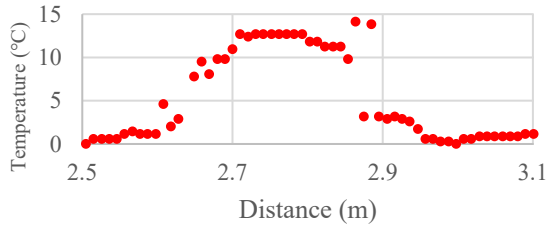(p) 405 ℃

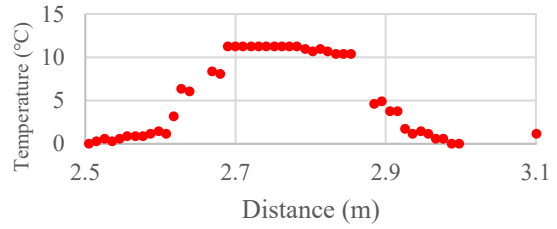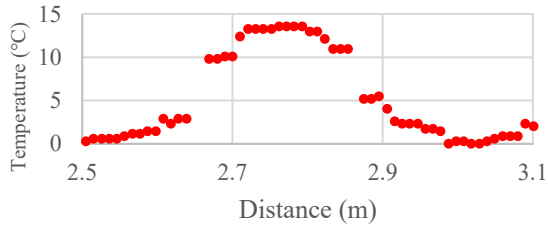**Figure 2.8 cont.** Temperature distribution along the steel plate at elevated temperatures

Specifically, the temperature distributions in the transition zones can be considered generally linear towards the furnace ends and further outside. As mentioned before, the end zones of the furnace are subject to air circulation and heat loss over time. As a result, the process of Rayleigh scattering becomes uncertain, resulting in a sudden drop of the measured temperatures at some furnace temperatures. As an example, the Rayleigh frequency difference at 242 ℃ fluctuates significantly around a linear line in each transition region. This fluctuation is unsymmetrical about the mid-height of the furnace because of the vertical test setup in Figure 2.3. Due to the gravity effect, the heated air tends to flow from the bottom to the top (a convection phenomenon), and the dramatical air molecular movement at high temperatures causes the signal fluctuation. The linear temperature interpolation in the transition regions can be used to recover some of the missing data. Moreover, the linear distribution in the right side of each plot in Figure 2.8 generally shows a smaller slope (absolute value) than that in the left side because the right side corresponds to the top opening region of the furnace and the heated air flows out of the furnace here. Thus, a relatively large heat influence length is observed in the top opening region (i.e., right side).

Figure 2.8 is compared with Figure 2.5(a) to understand the effect of sheath and its bonding on the optical fiber on the Rayleigh scattering at various furnace temperatures. It is clearly observed that the temperature distribution along the steel plate is different during the calibration of an optical fiber sensor though they are placed inside the same furnace. When bonded to the steel plate with significant heat transfer, the temperature transition region is longer, and the constant temperature range is shorter. This is partly because the steel plate extends from inside to outside of the furnace, increasing the likelihood to leave small openings at the top and bottom of the furnace.

To further demonstrate the effectiveness of fiber optic sensors in temperature distribution measurement, the maximum temperature increment (or accumulative) measured in the central region inside the furnace is extracted and compared with the applied furnace temperature increment (or accumulative) as shown in Figure 2.9. In terms of the furnace temperature, the horizontal and vertical axles in Figure 2.9 represent the desirable temperature and the applied temperature increment that is accumulated to achieve the desirable temperature. It is clearly observed from Figure 2.9(b) that the optical fiber sensor provides relatively accurate measurements of temperature up to 267 ℃. The small error between the measured and furnace temperature is most likely associated with the sustained time at each furnace temperature increment (about eight min, including 2.5 min for TW-COTDR readings) and the uncertainties from the furnace setup and calibration test. However, significant differences can be seen from a comparison of temperature increments between the sensor measurement and furnace application, as indicated in Figure 2.9(a), and the temperature increment distributions (plateau at the maximum temperature) below and above 267 ℃, as shown in Figure 2.8. This was mainly because the sheath tube outside the optical fiber started to melt, expand, and bind to the optical fiber. The melting products on the surface of the fiber restrained its movement inside the sheath tube, making temperature measurement coupled with the uncertain effect of strain. The strain effect increased the measured "false" temperature increment and appeared to fluctuate periodically as observed in Figure 2.9(a) likely due to intermittent bonding of the sensor-plate interfaces towards the two ends of the optical fiber. This bonding process causes additional elongation of the fiber because the thermal coefficient of the glass fiber is approximately 4.4% that of the steel. This statement is further supported by the length of the temperature sensor that measures the maximum (constant) temperature in the center portion of the optical fiber as

49

summarized in Figure 2.10. The tests in this study were terminated at 405 ℃ since the measured

temperature distribution was verified to be inaccurate and the general debonding behavior was

observed.
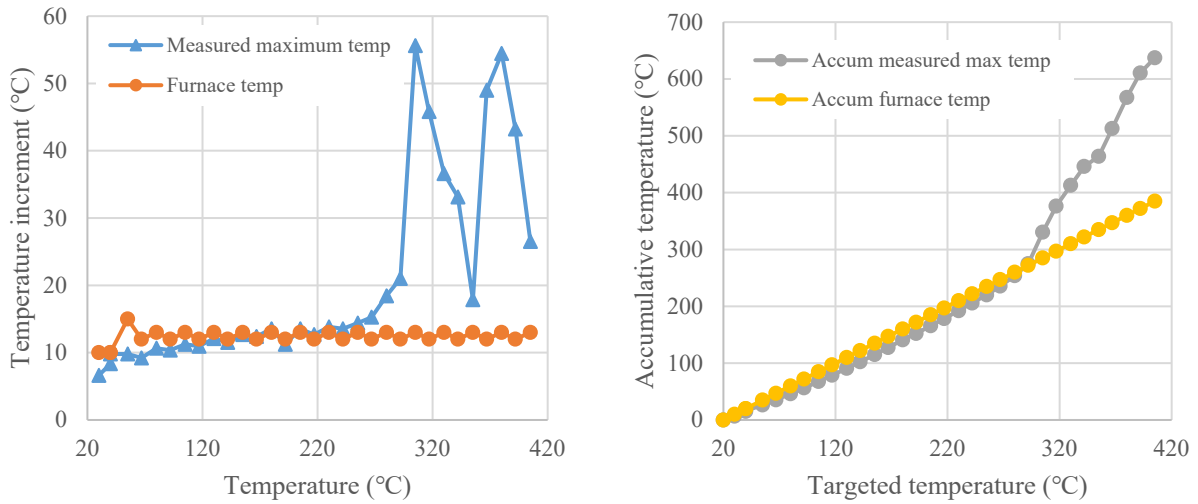
Figure 2.9 Comparison between the measured maximum temperature and the furnace
temperature: (a) Incremental, and (b) Accumulative (Accum)
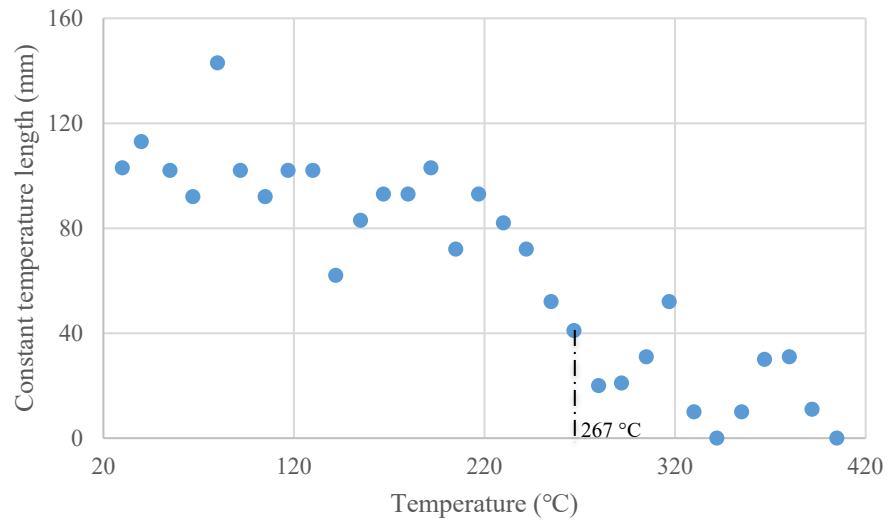
Figure 2.10 Constant temperature length (mm) in the center portion of the temperature sensor as
a function of applied temperature

To support the observation and conclusion about material softening and melting, a small piece of the sheath and the coating of the silica optical fiber sensors were prepared and tested to understand the heat transfer behavior. Specifically, sheath materials (mass unit: mg) used in the Y-DFOS were cut from a polymer tube. Polymer coatings were stripped off the optical fibers in the B-DFOS using a fiber stripper. Both samples were tested in the nitrogen gas environment with a flow rate of 100 ml/min. The samples were heated at a rate of 10 °C/min from room temperature to 600 °C and measured from a Simultaneous Thermal Analyzer (SDT, TA Instruments Q600). Figure 2.11 presents the representative test results from one sheath sample and one coating sample. A sudden reduction in heat flow is indicative of change in material behaviors: melting. Figure 2.11 indicates that the melting temperature of the sheath is slightly below 297 °C while that of the coatings is slightly below 315 °C. These melting temperatures are in the order of 300 °C for polyimide as thermoplastic polymers as discussed in Polymicro Technologies (2009). The temperatures corresponding to 5% reduction in weight are approximately 263 °C and 282 °C for the sheath and coating materials. The "apparent" melting temperature 267 °C (as indicated by the vertical dashed line in Figure 2.11) identified from the temperature distribution in Figure 2.8 is close to the material melting temperatures below 297 °C and 315 °C for the sheath and coating, respectively.
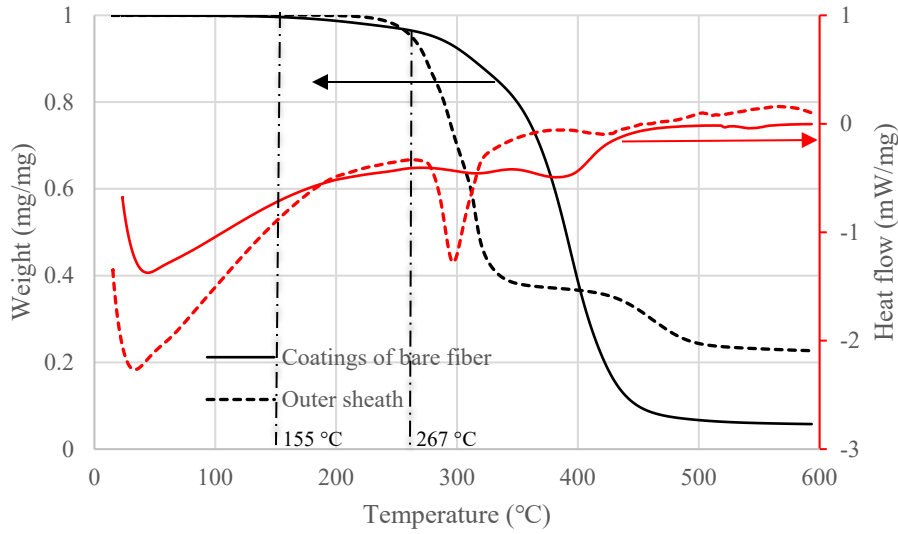
Figure 2.11 Thermogravimetric analysis of B-DFOS coating and Y-DFOS outer sheath

2.4.2.2 Measured strain distribution

Figure 2.12 shows a series of thermal-induced strain increment distributions measured from the distributed fiber optic sensors at different applied temperatures. For example, Figure 2.12(a) has two (left and right) strain increment distributions at 30 ℃ that were increased from room temperature. The left side (blue) represents the strain increment calculated from the measured temperature increment with a thermal expansion coefficient of steel (i.e., 12.6 $\mu\varepsilon$/°C), which is regarded as a true strain increment. The right side (orange) represents the strain increment calculated from the strain sensor (i.e., B-DFOS in Figure 2.3) after temperature compensation using the temperature sensor data (i.e., Y-DFOS in Figure 2.3). That is, the Rayleigh frequency measured from the temperature sensor was subtracted from the strain sensor frequency; the frequency difference was then multiplied by the frequency-strain coefficient to obtain the strain distribution. Since the Y-DFOS and B-DFOS sensors were connected in a single optical fiber to form a U-turn and then bound to the steel plate side by side in parallel, as shown

52

in Figure 2.4, the left-side and right-side strain distributions are in theory symmetric about their center point at 3.193 m, as illustrated in Figure 2.12(a) for the strain increment distribution at 30 ℃. Therefore, the measured temperature at 2.885 m as shown in Figure 2.12 was used to compensate for the measured thermal-induced strain at 3.501 m. This calculation procedure for temperature compensation is limited to 267 ℃ below which the temperature measurement is accurate. For compensation above 267 ℃, a tri-linear temperature distribution corresponding to the strain distribution in Figure 2.12(k) is assumed when determining strain distributions, which is based on the temperature distributions below 267 ℃. The assumed temperature distribution has three segments: 1) linear increase from 3.388 m to 3.532 m; 2) constant from 3.532 m to 3.868 m; and 3) linear decrease from 3.686 m to 3.788 m. The left segment has a smaller slope than that of the right segment due to gravity effect because the left segment corresponds to the top opening of the furnace as discussed before.

As indicated in Figure 2.12, the left-side and right-side strain increment distributions appear symmetric below 267 ℃. At 30 ℃ and 40 ℃, the measured peak strains in the right side are slightly lower than those in the left side. This is because the low-temperature heat transfer process from the furnace to the optical fiber sensor likely took longer than eight min to set during the test. Given sufficent time, the temperatures along the steel plate would approach those near the wall of the furnace. This heat balance process was affected by the fact that the two ends of the steel plate were exposed to air and thus part of the heat generated inside the furnace was exchanged with outside air. The heat balance problem was compounded further by potential air paths at the top and bottom ends of the furnace though they were sealed to the extent possible during the test. Above 155℃, the strain increment at the center portion of the furnace appears lower than that towards the two ends of the furnace, which is indicative of notable strain transfer

53

between the steel plate and its bonded optical fiber. This is because the coating materials on the optical fiber start to soften at 155℃ and then melt at 267℃. This strain reduction in the center portion of the furnace becomes more pronounced at high temperatures. The extent of the strain reduction from the center to the two ends increases gradually as the temperature increases. At 267℃, the extent of the strain reduction suddenly increases as shown in Figure 2.12(j), which is indicative of the effect of coating melting and the optical fiber core and cladding are anchored towards the two ends of the furnace. The strain measurements above 267℃ corresponding to the applied temperatures used in Figure 2.8 were taken during the two steel plate tests. They are not presented in Figure 2.12 since further studies are warranted to understand the regression trends and the melting process of polymer coating.
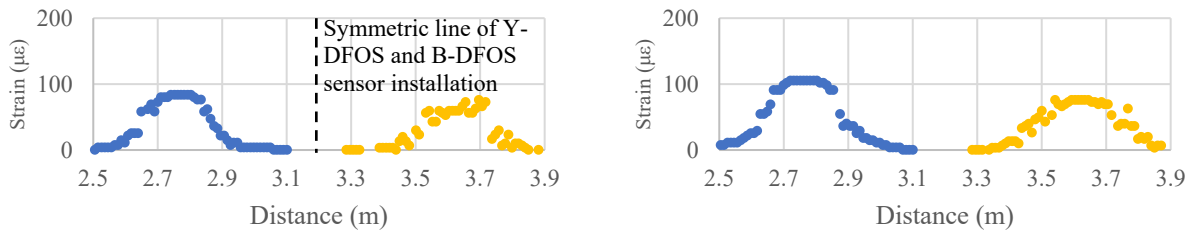
(a) 30 and 40℃
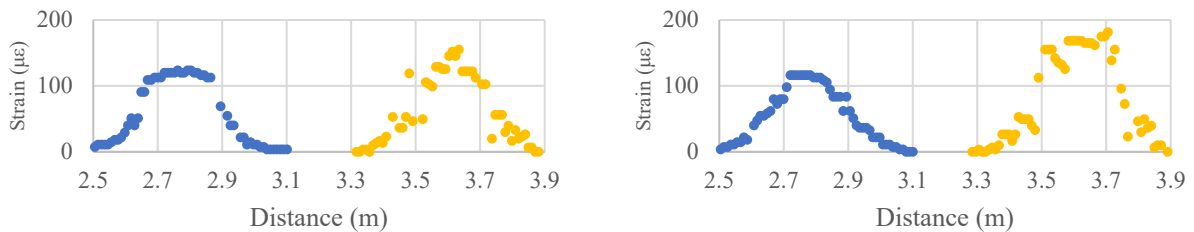
(b) 55 and 67℃

Figure 2.12 Measured and calculated strain distributions at different temperatures up to 267 °C
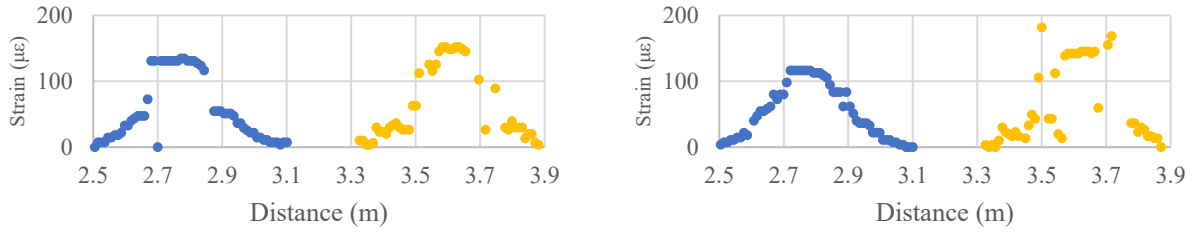
(c) 80 and 92℃
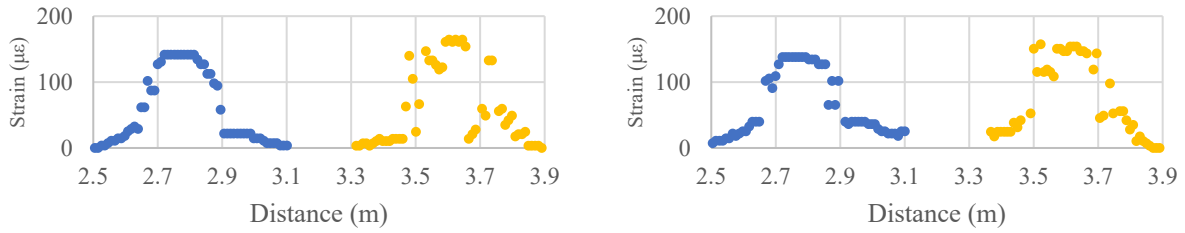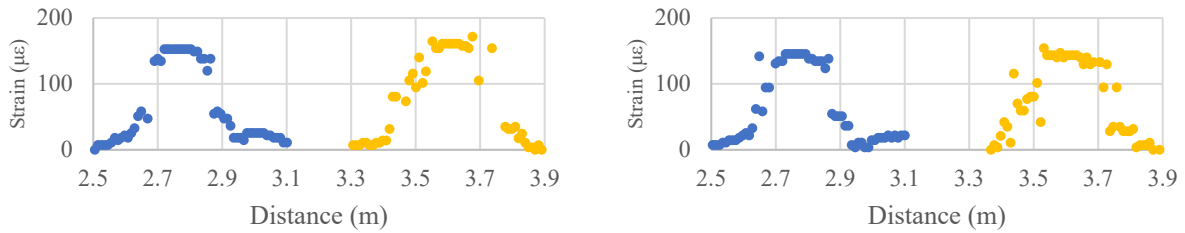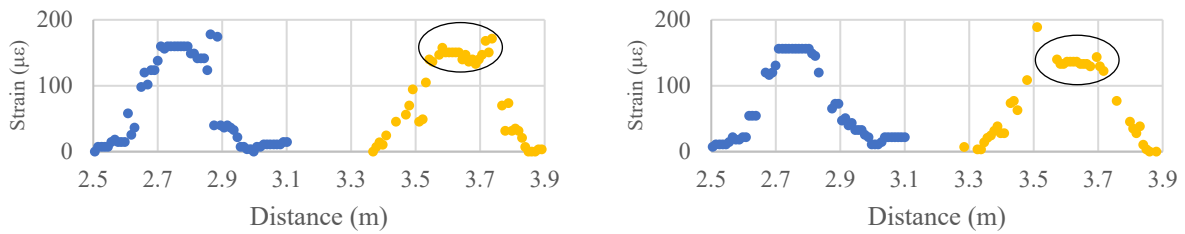
(d) 105 and 117℃

(e) 130 and 142℃

(f) 155 and 167℃

Figure 2.12 cont. Measured and calculated strain distributions at different temperatures up to 267 °C
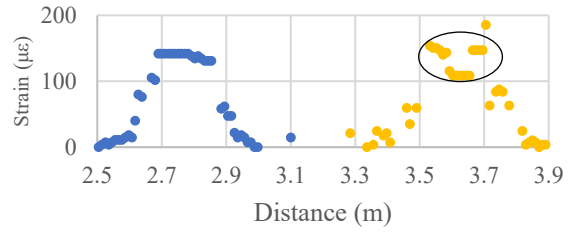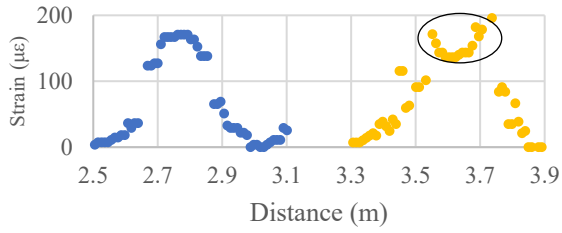
(g) 180 and 192℃
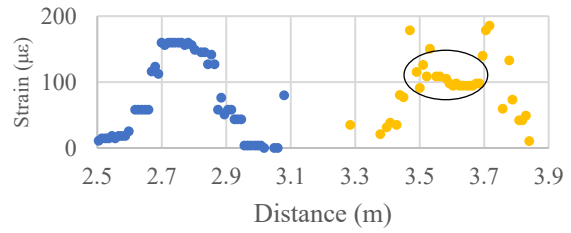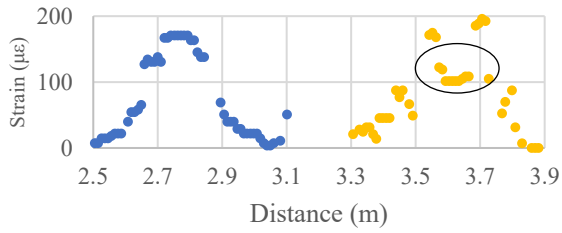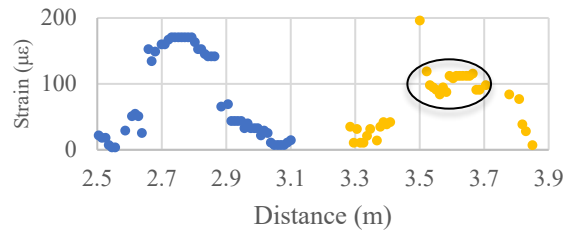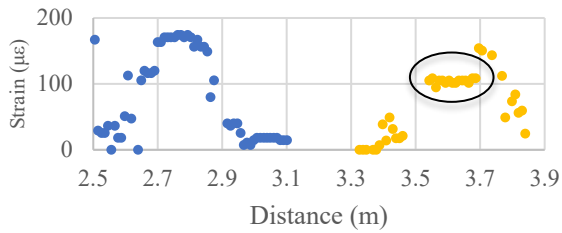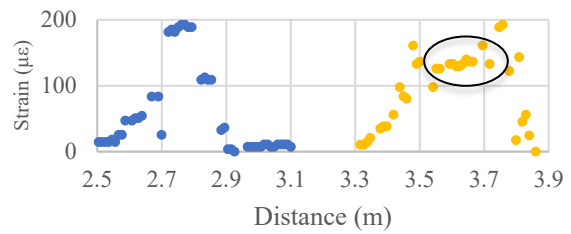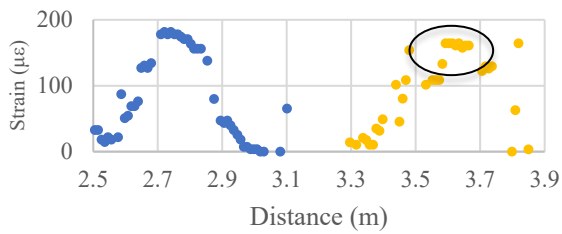
(h) 205 and 217℃

(i) 230 and 242℃

(j) 255 and 267 ℃

Figure 2.12 cont. Measured and calculated strain distributions at different temperatures up to 267 °C

The melting and anchoring process was confirmed by a micro-structure investigation of the test specimen after exposure to 405℃ using an optical microscope, as shown in Figure 2.13. The melting of the polymer coating left behind a gap between the optical fiber (center portion in the furnace) and its surrounding epoxy and then steel plate, as clearly indicated in Figure 2.13(a). Towards the end of the furnace, the temperature is lower and the polymer coating can effectively bond/anchor the optical fiber to the steel plate, as indicated in Figure 2.13(b). As a result, the strain sensor in the center portion of the furnace functioned like an extensometer. Considering the fact that the temperature sensor Y-DFOS functions as designed below 267 ℃, as shown in Figure 2.8, and the temperature-compensated strain sensor B-DFOS with its coating experiencing softening between 155 ℃ and 267 ℃ can still measure strain up to 100 $\mu\varepsilon$, as shown in Figure 2.12(g), (h), and (i), both the temperature and strain fiber optic sensors are considered effective in fire engineering applications. For temperature compensation, the measured temperature from the Y-DFOS was directly used.

(a)   (b)
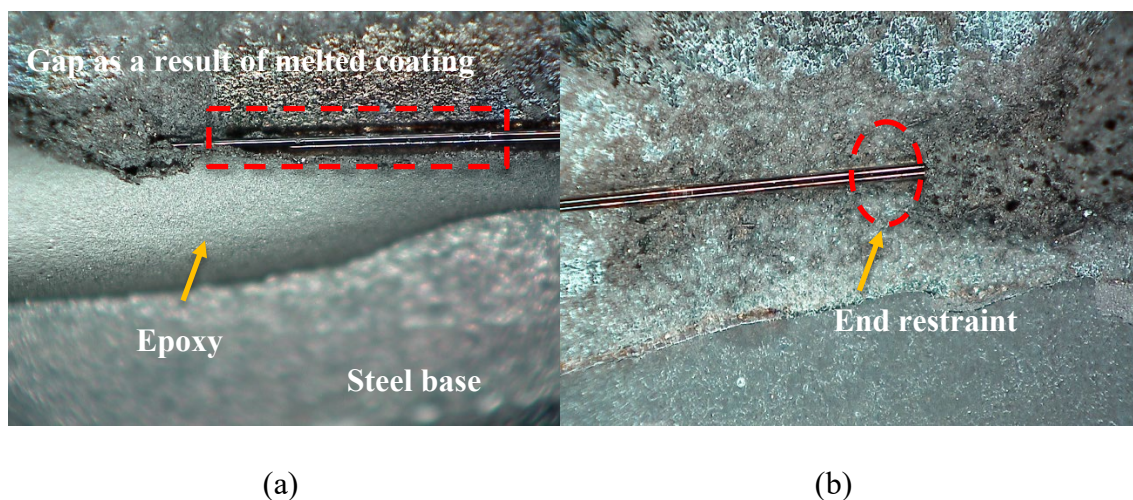
Figure 2.13 Post-test investigation on the micro-structure around the optical fiber strain sensor

Figure 2.14(a) compares the thermal-induced strain calculated from the measured temperature of the furnace by the thermometer with the measured strains from three fiber optic strain sensors compensated with the measured temperature at the center point of the furnace. The three strain sensors are labeled as B-DFOS 1 attached onto the first steel plate and B-DFOS 2 and B-DFOS 3 onto the second steel plate. Figure 2.14(b) includes exactly the same quantities as in Figure 2.14(a) except the furnace temperature is replaced by the temperature measured at the center of the furnace by the Y-DFOS. The thermal-induced strain is calculated by multiplying the temperature change by the thermal expansion coefficient of 12.6 με/°C. It can be seen from Figure 2.14(a) that the measured strains from three B-DFOS sensors are quite consistent except for one point at 405 °C when the furnace temperature is used to compensate strain measurement. However, the measured strains are all less than the thermal-induced strain because the furnace temperature represents the upper bound of the temperature of the steel plate. In Figure 2.14(b), the measured temperature from the Y-DFOS represents the temperature of the steel plate. The three measured strains with temperature compensation coincide with each other; they are in excellent agreement with the thermal-induced strain up to 267 °C with a maximum error of 13%. Above 280 ℃, the thermal-induced strain and the measured strains differ from each other without any general trending for several reasons. First, the measurement of high temperatures is inaccurate as indicated in Figure 2.8. Second, the anchor condition at the two ends of the optical fiber, affecting strain measurement, is weak and uncertain at high temperatures. Third, the Rayleigh frequency signal becomes increasingly fluctuated at high temperatures. Lastly, the bond effectiveness between the epoxy and steel plate is unknown at high temperatures.
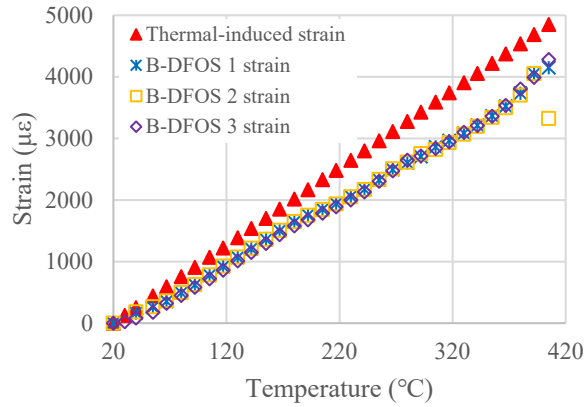
(a) Based on the furnace temperature
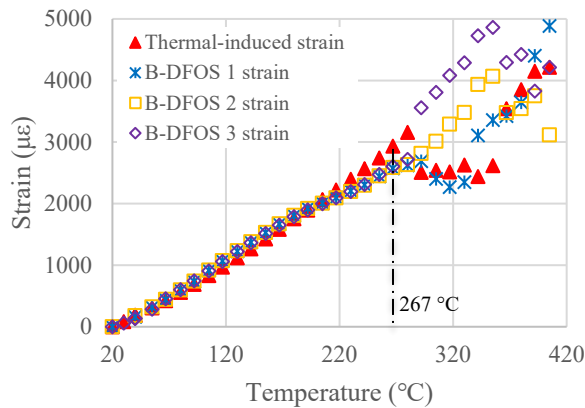
(b) Based on the Y-DFOS temperature

Figure 2.14 Strains at applied temperatures at the center point of the furnace

2.4.2.3 Experimental versus calculated displacements at the cantilevered end of the steel plates

Figure 2.15 compares the calculated displacement with the experimental displacement at the cantilevered end of the two steel plates. The displacements of the two steel plates measured from the dial gauge are denoted by "Measured from dial gauge 1" and "Measured from dial gauge 2", respectively. The thermal-induced displacement of the first steel plate based on the temperature measured from the Y-DFOS is referred to as "Calculated from Y-DFOS temperature". The displacement of the first steel plate calculated from integrating the strain

distribution over the plate length, which is measured from B-DFOS 1 after temperature compensation, is denoted by "Integrated from B-DFOS 1 strain". The displacements of the second steel plate based on the strains measured from B-DFOS 2 and B-DFOS 3 after temperature compensation are denoted by "Integrated from B-DFOS 2 strain" and "Integrated from B-DFOS 3 strain", respectively.
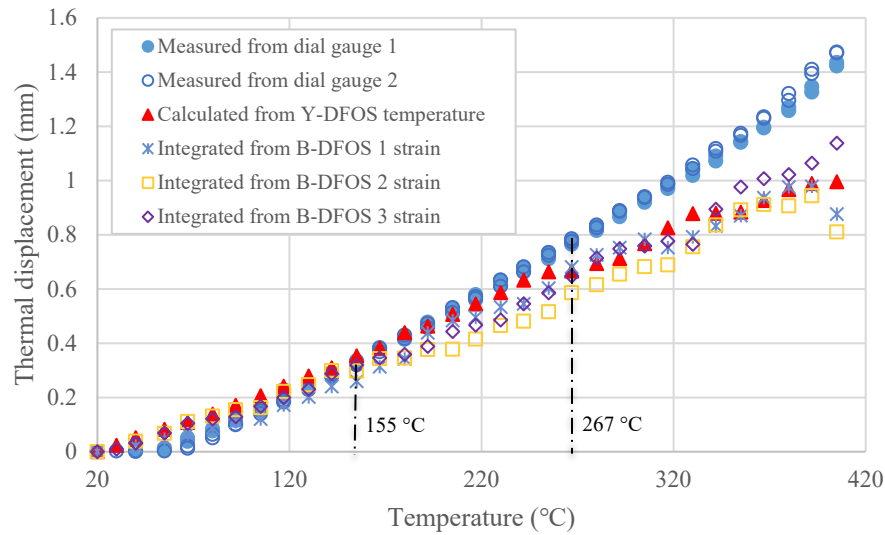
Figure 2.15 Thermal displacement of the two steel plates

The dial gauge reading taken outside the furnace is regarded as the ground truth of the displacement. Even so, its reading cannot be recorded until 67 °C as shown in Figure 2.15. This is likely caused by the crookedness of the steel plate, since it reduces the axial displacement at low temperatures. It can be observed from Figure 2.15 that the two measured displacements from the dial gauge nearly coincide with each other. The three displacements integrated from the three B-DFOS strains are in good agreement below 155 °C and in general agreement above 155 °C. They are validated by the dial gauge measurements below 155 °C. They have the same trend as

the thermal-induced displacement of the first steel plate, which is further agreement with the ground truth data till 267 °C. Above 267 °C, the difference between the thermal-induced displacement and the ground truth increases with the applied temperature.

2.5 Summary

The present study proposes an innovative application of distributed fiber optic sensors based on Rayleigh scattering for high accuracy and sensitivity measurement of the temperature, strain, and displacement of steel plates when locally heated. The distributed sensors have advantages over conventional displacement measurement techniques (i.e., dial gauge) in that they provide a high density of data points with high spatial resolution and are not required to be deployed out of heat zones for successful data recording. The proposed application can be useful in performance-based fire design. Based on this study, several conclusions can be drawn:

- Rayleigh scattering is several times more sensitive to changes in temperature and strain than Brillouin scattering. The temperature distribution measured from Rayleigh frequency differences experiences significant fluctuation near the ends of a furnace due to high frequency vibration associated with heat exchange inside and outside the furnace through its top and bottom openings. A temperature increment of 13 °C ($<<$ 20 °C) is recommended to ensure successful correlation analysis of Rayleigh scattering signals.

- Constant frequency-strain and frequency-temperature coefficients (-6.997 $\mu\varepsilon$/GHz and 0.5758 ℃/GHz) can be used to discriminate both strain and temperature through Rayleigh scattering up to 267 ℃. Further characterization is required to understand the coefficients at higher temperatures.

- The coating and sheath of single-mode optical fibers start to soften at 155 °C and melt at 267 ℃ as verified by thermogravimetric analysis. Similar to temperature sensors, optical

fibers with an insulation sheath can accurately measure temperatures up to 155 °C, up to 267 °C with thermo-mechanical analysis of potential sheath-fiber bonding behavior, and much higher temperatures after the coating and sheath are completely burned off.

- Similar to strain sensors, optical fibers with temperature compensation are accurate for strain measurement up to 155 °C, above which strain transfer analysis is required due to softening of the fiber coating. Under a temperature gradient covering 155 °C to 267 °C, such as the temperature distribution of the furnace in this study, the optical fibers attached on steel plates with epoxy function like an extensometer as a center portion of the coating is melted. When the entire coating is completely melted above 267 ℃, the strain sensors function like temperature sensors as a cavity develops, verified by optical microscopic analysis, and surrounds the optical fibers on the steel plate sample tested at 405 ℃.

- The thermal-induced displacement of steel plates based on the measured temperature below 267 ℃ is in good agreement with the dial gauge reading. Its inaccuracy is mainly caused by the incomplete heat transfer from the furnace to the fiber optic temperature sensor. The displacement obtained from integrating the measured strain distribution with temperature compensation is in good agreement with the thermal-induced displacement.

Based on the present study, several opportunities for future research are identified to promote further understanding of the thermal measurement by distributed fiber optic sensors:

- The temperature increment fluctuation above 267 °C as shown in Figure 2.9(a) warrants further studies to fully understand the bonding and debonding mechanisms between the optical fiber coating and its outside sheath as the temperature sensor experiences softening and melting during the heating process.

- Under a significant temperature gradient covering 155 °C to 267 °C, the extensometer-like measurement principle with locally anchored points must be understood and quantified during the bonding and debonding process of a fiber optic strain sensor. Quantifying the temperature-dependent anchoring effectiveness will help improve strain measurement accuracy and consistency after 155 ℃ to 267 °C.

The softening effect of a sheath tube can be precisely measured at various temperatures with a displacement measurement outside a furnace. Whether the softening process expands or shrinks the sheath tube in volume will help understand the potential mechanism of bonding it to the inside optical fiber with coating.

Chapter 3 Quantifying Thermal Strain of Steel Plate Subjected to Constant Temperature by Distributed Fiber Optic Sensors

3.1 Introduction

The stress and thermal behaviors of steel at high temperatures have been widely studied by the fire research community since the strength degradation and collapse of steel structure during a fire would directly threaten human lives and destroy public property. As a result, the high temperature properties of steel, as one of the primary construction materials, must be investigated for the purpose of design, enhancing resilience of steel structures (Chen et al. 2006) (Chen and Young 2007). The experimental approach is commonly used for testing steel behavior at elevated temperatures. During the test, thermocouples are used for measuring temperatures at different locations (such as thermocouples inside the furnace and on the specimen surface). To measure tensile specimen strain at high temperatures, an axial extensometer with range limitation of several millimeters is usually used in a test setup. Although these traditional measurements exhibit high accuracy and have been widely accepted at ambient temperatures, the measurement concerns still exist at high temperatures. For example, uneven temperature distribution of the high temperature furnace cannot be easily measured by thermocouples. In a small furnace, an internal thermocouple is used to measure the inside air temperature of the furnace, while an external thermocouple is used to measure the specimen surface temperature. For most cases, the measured one-point surface temperature is considered the real specimen temperature. Although this assumption may be acceptable for most studies in the structural behavior evaluation, the large differences between the internal and external thermocouple temperatures can be observed (up to 28%), which depends on the heat time, heat rate, and temperature increment (Chen et al. 2006). Therefore, the investigation on measurement techniques for recording steel behavior at high temperatures is still needed.

Fiber optic sensors show excellent structural health monitoring as well as damage detection and evaluation capacities because of small dimension, light weight, high sensitivity, and immunity to electromagnetic interference (Kim et al. 2013a). Fiber Bragg grating sensors with excellent sensitivity and multiplexing capacity can provide discrete-point measurements, while distributed fiber optic sensors (DFOS) can measure strain or temperature along an optical fiber with spatial and sampling resolutions based on the principle of Rayleigh, Brillouin, and Raman scatterings (Kim et al. 2013b). Many innovative developments and applications by using optical fiber sensors have been proposed in recent decades (Barrias et al. 2016, Yan et al. 2022, Bado et al. 2022, Bado and Casas 2021, Fan and Bao 2021). For example, a metal coated fiber Bragg grating sensor was developed for further improving sensor sensitivity. A theoretical strain transfer considering both shear stress and axial stress of the metal coating was proposed, and elasto-plastic characteristics of the metal coating were included in the numerical and analytical models, which were verified by the experimental test on the composite specimens instrumented with the developed metal-coated sensors (Kim 2017). In addition, DFOS based on the pre-pulse pump Brillouin optical time domain analysis have been successfully applied to measure cracks, strains caused by concrete shrinkage, and steel reinforcement corrosion in concrete (Bao and Chen 2015, Bao et al. 2015, Fan et al. 2018). Moreover, DFOS have been used to measure temperature distributions of steel-concrete composite structures subjected to a fire (Bao et al. 2020). However, DFOS based strain measurements of steel and concrete at high temperatures have rarely been investigated, although the strain calibration coefficient of a bare optical fiber without coatings was investigated at high temperatures (Bao and Chen 2016). Also, Bao et al. (2017b) custom-designed a strain sensor with a gauge length of 50 mm for measuring steel elongation. The Brillouin scattering based fiber optic sensor data provided discrete-point average

65

strain for analyzing steel behavior subjected to a fire. The cracks in concrete structures subjected to a fire were successfully detected and identified by the sharp peaks in the temperature distribution monitored by DFOS due to hot air filling the cracks (Bao et al. 2017a), while concrete spalling broken the optical fiber sensor loop required for the Brillouin scattering based measurements.

Recently, the Rayleigh scattering with Neubrescope NBX-7020 (Neubrex Co., Ltd., Japan) improves measurement accuracies by approximately seven times in temperature and 15 times in strain, as compared to the Brillouin scattering. Zhu and Chen (2022) investigated the effect of the polymer sheath and coatings on the Rayleigh scattering based measurement accuracy of DFOS under a heating-holding protocol since the polymer softens and melts away at high temperature. The effective distributed temperature and thermal-induced strain measurements were identified. However, the two-part epoxy was covered along the whole length of the tested steel plate. To further provide direct understanding for thermal-induced strain measurement effectiveness of the Rayleigh scattering based DFOS, the experimental test should be well-controlled, and the influencing factors can be reduced. The DFOS is locally bonded to a steel plate by using an epoxy with different bond lengths in the present study to secure the thermal-induced strain measurement segment in a constant temperature zone created by the furnace. The short constant temperature segment is also useful to reduce the gradient temperature effect and the anchoring effect at the optical fiber ends covered by the epoxy located at ambient temperature when a long epoxy covering is applied. Moreover, the polymer coatings on the optical fiber are stripped off in this test to reduce the coating effect, although the pure glass cladding and core are vulnerable to mechanical deformation. The fracture of the optical fiber without coatings caused by thermal-induced strain at a relatively low temperatures (smaller than

150 ℃) occurs, which is beneficial for guaranteeing a reliable interface between the epoxy and steel plate. Again, this experimental design will provide a basic understanding for coupled strain and temperature measurement effectiveness and limitation of DFOS without coatings locally bonded to the steel plate in sunshine temperature. In addition, a finite element model is established to simulate the thermal behavior of the tested steel plate instrumented with DFOS in the elastic stage and the numerical results are compared with the test ones. The effect of different parameters (such as mechanical and geometrical properties of the epoxy) on the strain transfer between the optical fiber and host material is investigated through the calibrated numerical model, and a normal-distribution epoxy shape is designed for a guiding robot assisted intelligent instrumentation and construction in the future, which further propels distributed fiber optic sensing technology development for structural measurements at high temperatures in practice.

3.2 Tunable Wavelength Coherent Optical Time Domain Reflectometry (TW-COTDR)

The Rayleigh scattering response in the sensing optical fiber was exploited, based on the tunable wavelength coherent optical time domain reflectometry (TW-COTDR) principle. The operating wavelength range the tunable laser could achieve for measurements was between 1530 and 1560 nm. Only single end access measurement was needed (from the pump end in the Rayleigh system NBX-7020), which was an important advantage over the Brillouin scattering since two-ended configuration for a loop was required and the whole Brillouin scattering signature disappeared once optical fiber facture occurred at a single point in civil engineering applications. This technique had distributed measurement with a high spatial resolution of two centimeters. The Rayleigh frequency spectral shift Δv_R at a given time related to temperature and strain changes (ΔT and $\Delta \varepsilon$) of the optical fiber was traced by using a cross-correlation procedure with respect to a reference Rayleigh scattering measurement. Therefore, the applied temperature

and strain changes along the optical fiber length can be simultaneously recorded through the cross-correlated Rayleigh scattering traces based on the TW-COTDR technique as follows.

$$\Delta v_R = C_\varepsilon \Delta \varepsilon + C_T \Delta T \tag{3.1}$$

where, C_ε and C_T were strain coefficient and temperature coefficients, respectively, and these coefficients depended on the sensing element (i.e., optical fiber) properties, such as chemical compositions of glass core and cladding, coating, and drawing conditions). It is necessary to calibrate the optical fiber in the lab before use in the field since the unique optical fiber coefficients of the Rayleigh scattering responses are affected by different uncertain factors (such as packaging).

3.3 Specimen Preparation and Test Procedures

The telecommunication-grade single-mode optical fiber as distributed fiber optic sensors (DFOS) is investigated in this study as described in Figure 3.1. The outer and inner coatings with diameters of 242 and 190 μm, respectively, can protect the glass from mechanical impact, abrasion, and environmental exposure. The diameters of the glass core and cladding are 8.2 and 125 μm, respectively. Since the existing of the outer and inner coatings induces strain lag between the optical fiber core and the host material if the optical fiber with coatings (left image in Figure 3.1) is bonded to a host material, the outer and inner coatings were burned off using fire in advance and the bare optical fiber (middle image in Figure 3.1) was used in the following calibration and application tests.

For the temperature and strain calibration tests, the test setup, furnace, and interrogator used in this study were the same as those in Zhu and Chen (2022). The main differences between

the present and previous studies during calibration were as follows. The bare optical fiber with glass core and cladding was used in this study as it was much easier to fracture. Moreover, an additional thermocouple probe (Type K) was adopted for recoding the furnace temperatures by a thermometer (Model 8110-10, Cole-Parmer Instrument Company) in addition to the thermocouple inside the furnace near the ceramic wall (as shown in Figure 3.2(a)) during the tests. In the temperature calibration test, the external thermocouple probe was placed at the furnace center as shown in Figure 3.2(b). However, in the strain calibration test, the external thermocouple probe was placed at the position left and upper offset from the furnace center by 2 cm and 1.5 cm, respectively, because of the position limitation of the bottom grip as shown in Figure 3.2(c).

Figure 3.1 Optical fiber cross-sections before and after burning off outer and inner coatings
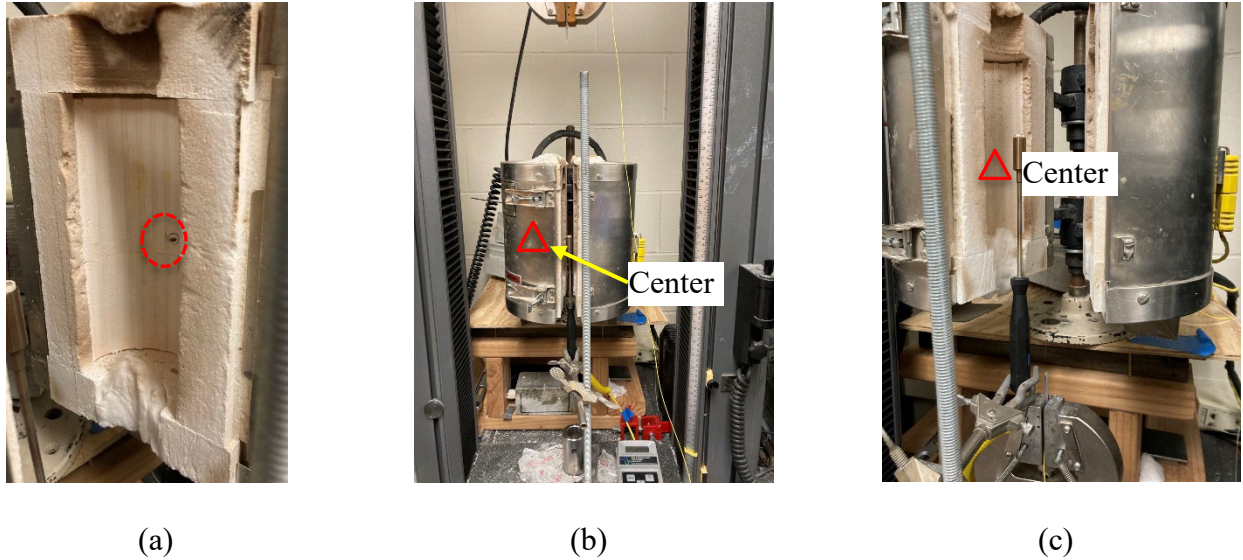
Figure 3.2 Different thermocouple locations (a) mid-length of the furnace near the ceramic wall (b) center of the bore of the furnace (c) offset from the furnace center

For the application test, the steel plate (ASTM A366 1008 steel: 600 mm long, 1 mm thick, and 20 mm wide) bonded with the bare optical fibers were prepared and tested as shown in Figure 3.3. The three different bond lengths, namely 8 cm, 10 cm, and 12 cm, respectively, were investigated. Two sensors were parallelly bonded to the steel plate, and they formed a U-turn at the left end. These bond lengths were selected to keep a constant temperature along the epoxy achieved by the furnace. Therefore, the optical fiber segments covered by the epoxy measured temperature and strain simultaneously at high temperatures, while the segments without epoxy inside the furnace measured temperature only. As a result, the strain and temperature results could be separated from the test results. Since the constant temperature region was shifted upward due to the gravity effect of the vertical furnace setup, the epoxied regions with different bond lengths were being shifted upward as shown in Figure 3.3. For example, the total bond length of 8 cm would be a sum of 2 cm at the right side of the center and 6 cm at the left side of the center. Before they were placed into the furnace for measuring strain and temperature of the

steel plate, at least 24 hours of ambient curing time was needed to harden the epoxy. The basic

properties of the epoxy were 34.6 MPa in strength, 4.6 h in set time, 15-24 h in curing time, and

dark grey in color. The test setup for measuring temperature and strain of the steel plate by using

the DFOS covered by the epoxy with a bond length of 12 cm is shown in Figure 3.4. The

thermocouple probe was also used in the application test. The position of the thermocouple probe

was near the mid-length of the furnace (0 cm lower from the center and 2 cm left offset from the

center due to the grip dimension). After the steel plate instrumented with two sensors, the

temperature was applied by the furnace with an increment of 10 °C recorded by the furnace

thermocouple. About four minutes later, the data from the optical fiber was measured by the

integrator - Neubrescope data acquisition system (NBX-7020) to perform TW-COTDR

measurements. In this test, the spatial and sampling resolutions were set at 2 and 1 cm, meaning

the Rayleigh frequency shifts of two points spaced at no smaller than 2 cm can be distinguished,

and the data points were sampled at every 1 cm. Other parameters were set to achieve a good

balance between data acquisition duration and measurement accuracy as follows: measurement

distance range of 50 m, average count of 212, output pump power of 25 dBm, frequency range of

194,000-194,300 GHz with a frequency step of 500 MHz. The selected frequency range was to

ensure a detectable measured frequency difference, and the cross-correlating two-by-two

measurement approach was used to enhance measurement accuracy by correlating the present

measurement with the immediately past reference. Each measurement time was about 2 minutes

and 30 seconds.
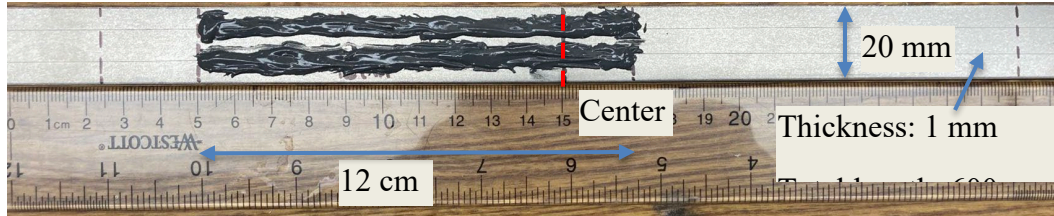
Figure 3.3 Different thermocouple locations (a) mid-length of the furnace near the ceramic wall
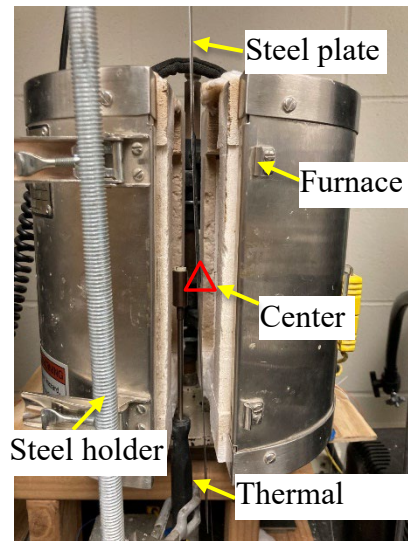
Figure 3.4 Test setup for measuring temperature and strain of the steel plate by using DFOS covered by epoxy with a bond length of 12 cm

3.4 Sensor Calibration

3.4.1 Temperature Calibration Results

Figure 3.5 shows the furnace and additional thermocouple temperatures. The temperature increment monitored by the furnace thermocouple was 10 °C. It is found that their temperatures are different due to different thermocouple locations. At the initial stage, the temperature measured by the furnace thermocouple near the ceramic wall as shown in Figure 3.2(a) is slightly higher than the center temperature from the additional thermocouple. As temperature increases, the center temperature becomes greater than the furnace temperature. The additional

72

thermocouple is receiving radiative heat from the ceramic wall as well as measuring air temperature since it is hovering in the middle of the furnace. The thermocouple installed in the furnace is flush with the insulation and does not receive direct radiative heat from the heat element. At a result, a temperature difference of 37.5 ℃ can be observed at the end in Figure 3.5(b) where the temperature difference (y axis) is the center temperature subtracted by the furnace temperature. Therefore, the bore of this small furnace does not have an even temperature distribution, which further demonstrates the necessity to monitor temperature distribution in different regions by using DFOS.

Figure 3.6 shows the temperature calibration results. As temperature increases, the constant temperature region length increases towards two ends from Figure 3.6(a). Figure 3.6(b) shows the center temperature-accumulated Rayleigh frequency relationship. The center temperature represents the temperature measured from the additional thermocouple at the furnace center. The accumulated Rayleigh frequency represents the sum of the Rayleigh frequency shifts at the furnace center under each temperature increment. A parabolic equation excellently fits the data points with a determination coefficient of 1.000, indicating a good correlation between the center temperature and the accumulated Rayleigh frequency.
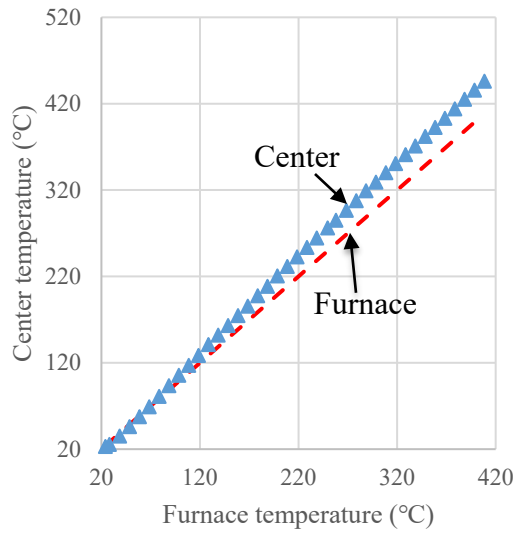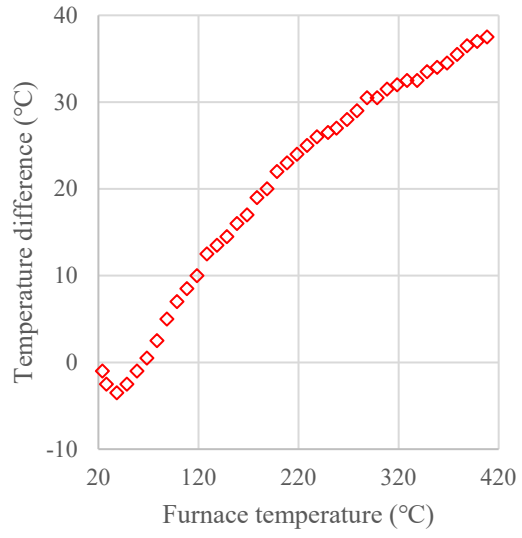
(a)   (b)

Figure 3.5 (a) Furnace and additional thermocouple temperatures (b) their differences
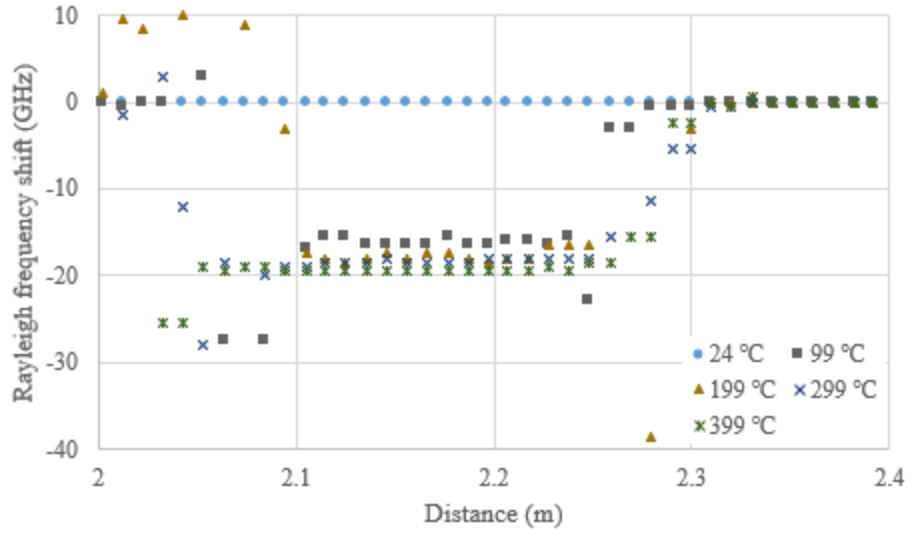
(a)
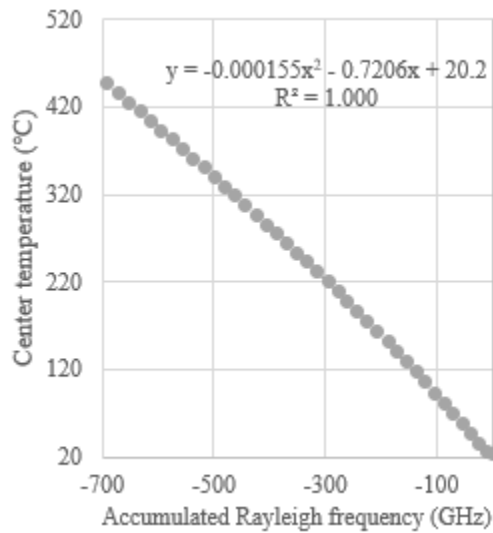
(b)

Figure 3.6 (a) Representative Rayleigh frequency shift along the optical fiber at high temperature (b) Center temperature - accumulated Rayleigh frequency relationship for the optical fiber without coatings

3.4.2 Strain Calibration Results

Figure 3.7(a) shows the representative Rayleigh frequency shift along the optical fiber subject to different displacements and the displacement increment was about 0.100 mm each

time. Very uniform Rayleigh frequency shift distribution can be seen and the average Rayleigh frequency shift at each displacement is used for obtaining the strain calibration coefficient. Figure 3.7(b) shows the load-extension relationship during tensioning the optical fiber where both the force and extension were recorded from the INSTRON Model 5965. Linear relationship between them is observed until the fracture of the optical fiber (about 1.0 mm at 20 ℃). Without coatings, the final extension value is significantly reduced as compared to the value of the optical fiber with coatings (Zhu and Chen, 2022). This can be regarded as a tradeoff. To increase the survival rate, the coatings reduce strain transfer efficiency. Similarly, the tension tests were conducted on the optical fibers without coatings subjected to 100, 200, 300, and 400 ℃. The same test setup was used, while the constant target temperature monitored by the additional thermocouple probe was applied by the furnace before the tension test. All the optical fiber fracture locations were within the test portion, not at the ends. Figure 3.8 shows the strain-accumulated Rayleigh frequency relationships at different temperatures. The strain (y axis) was calculated by the applied displacement divided by the original optical fiber length, while the accumulated Rayleigh frequency (x axis) represents the sum of the average Rayleigh frequency shifts over the sensing optical fiber under each displacement increment. At different temperatures, the linear trendlines well fit the (x, y) data with determination coefficients more than 0.995. Different equations with slopes for the trendlines are presented in Figure 3.8. Since the optical fiber without coatings shows the maximum measured strain of about 1600 $\mu\varepsilon$, the maximum temperature increment applied by the furnace may be about 130 ℃ (approximately equal to 1600 $\mu\varepsilon$/12.6 ($\mu\varepsilon$/℃) = 127 ℃) to measure thermal-induced strain of steel by the DFOS, and this maximum temperature was verified in the later application test. Also, the strain coefficients at 20 and 100 ℃ were used for the following strain calculation.
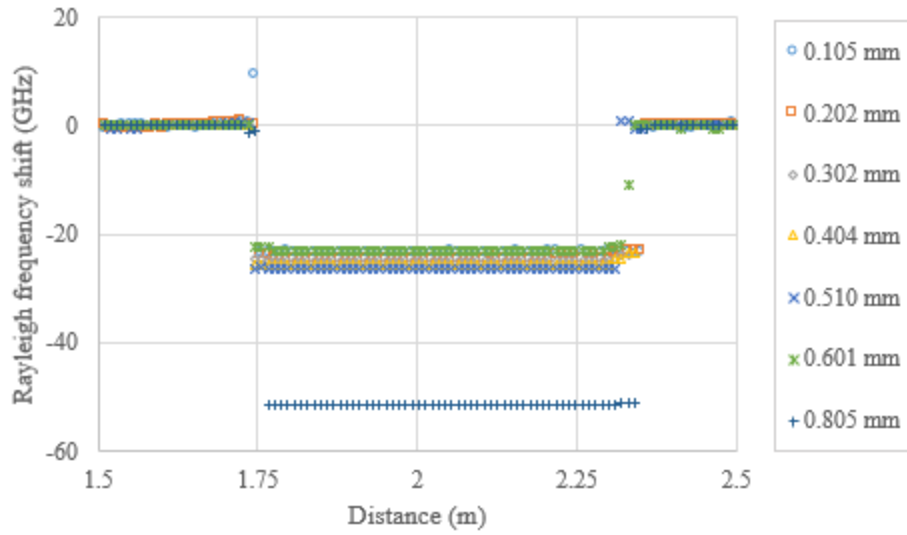
(a)
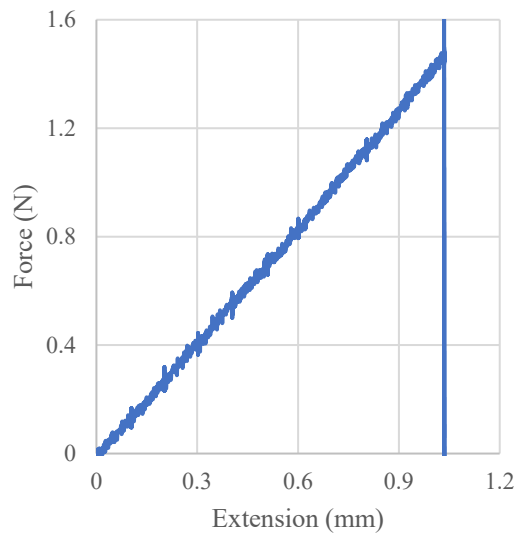
(b)

Figure 3.7 (a) Representative Rayleigh frequency shift along the optical fiber at different displacements (b) Load-displacement relationship at 20 ℃
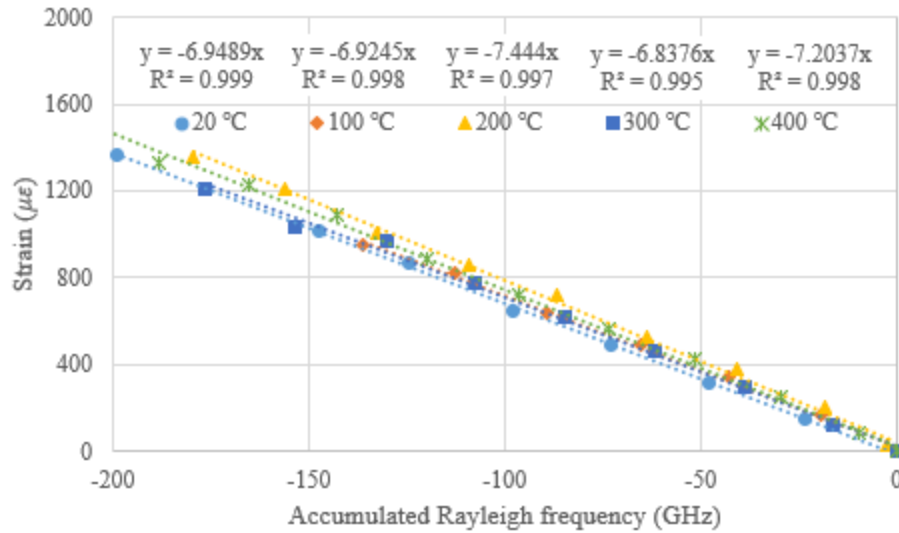
Figure 3.8 Different strain-accumulated Rayleigh frequency at different temperatures

3.5 Application Test Results

Figure 3.9 shows the representative Rayleigh frequency shift along the optical fiber

bonded to the steel plate locally by the epoxy with a length of 8 cm subject to different

temperatures (30, 50, 80, and 110 °C). The epoxied steel plate segment with distributed fiber

optic sensors (DFOS) was placed inside the constant temperature zone of the furnace. There are

two segments along the optical fiber in the constant temperature zone. The left side represents

the coupling effect of the temperature and strain transferred through the epoxy due to the thermal

deformation of the steel plate, while the right side represents the temperature effect only.

Generally, the left and right Rayleigh frequency shift distributions are uniform. Therefore, the

representative temperature-induced Rayleigh frequency shift is used for the compensation of the

Rayleigh frequency shift at the left side to calculate the strain distribution. Ideally, there are nine

points at the left side with the bond length of 8 cm because the sampling resolution is 1 cm. Eight

points are counted at the left side probably because of the limited spatial resolution (i.e., 2 cm) at

the edge; 1 cm on the left edge was not covered by the epoxy and 1 cm on the right edge was

covered by the epoxy. Figure 3.10 shows the measured temperatures by the thermocouples and

DFOS. The measured temperatures (y axis) represent the temperatures measured by the

additional thermocouple and DFOS. The furnace temperatures (x axis) represent the

temperatures measured by the furnace thermocouple. Since each measurement time for DFOS

with TW-COTDR technology needs 2.5 min, two-time records from the furnace and additional

thermocouples were made (corresponding to TC1 and TC2 data group). The temperature

increment for the furnace thermocouple was about 1 ℃, while it was about 2-3 ℃ for the

additional thermocouple during TW-COTDR measurement time as shown in Figure 3.10. The

DFOS data group was calculated by the right-side Rayleigh frequency shift induced by the

temperature effect only (as shown in Figure 3.9) and the temperature coefficient equation in

Figure 3.6. It is found that an excellent temperature agreement between the DFOS and TC2 from

the additional thermocouple is obtained, although the additional thermocouple slightly shifts

from the center location of the furnace. Figure 3.11 shows the measured strain-temperature

relationships from the DFOS covered by the epoxy with different bond lengths. Thermal-induced

strain represents the DFOS measured temperature calculated by multiplying the optical fiber

segment without epoxy by the thermal expansion coefficient of the steel (i.e., 12.6 $\mu\varepsilon$/℃), while

DFOS strain represents the DFOS measured strain calculated by subtracting the measured

temperature-induced Rayleigh frequency shift from the product of the strain coefficient and the

strain-induced Rayleigh frequency shift, determined from the coupled strain and temperature

optical fiber segment. Generally, the DFOS measured strain shows excellent agreement with the

thermal-induced strain in the bond lengths of 8 cm and 10 cm, while slight differences are

observed in the bond length of 12 cm. Also, the DFOS measured strains show small scattering

from the small standard deviations. The DFOS without coatings can measure the strain smaller

than 1600 $\mu\varepsilon$.
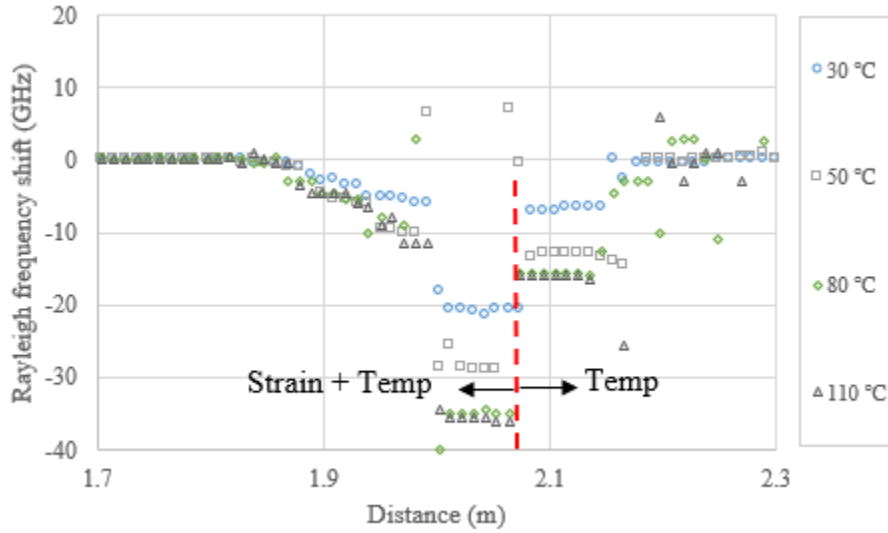
Figure 3.9 Representative Rayleigh frequency shift along the optical fiber covered by epoxy with a bond length of 8 cm on the steel plate subjected to temperature increment
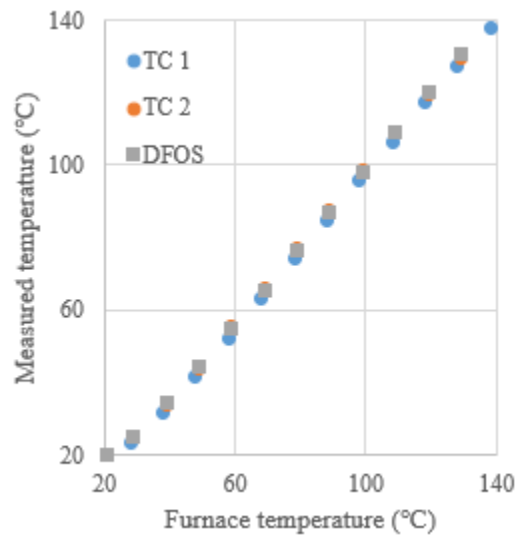
Figure 3.10 Measured temperature (Temp) from center thermocouple and DFOS with the bond length of 8 cm
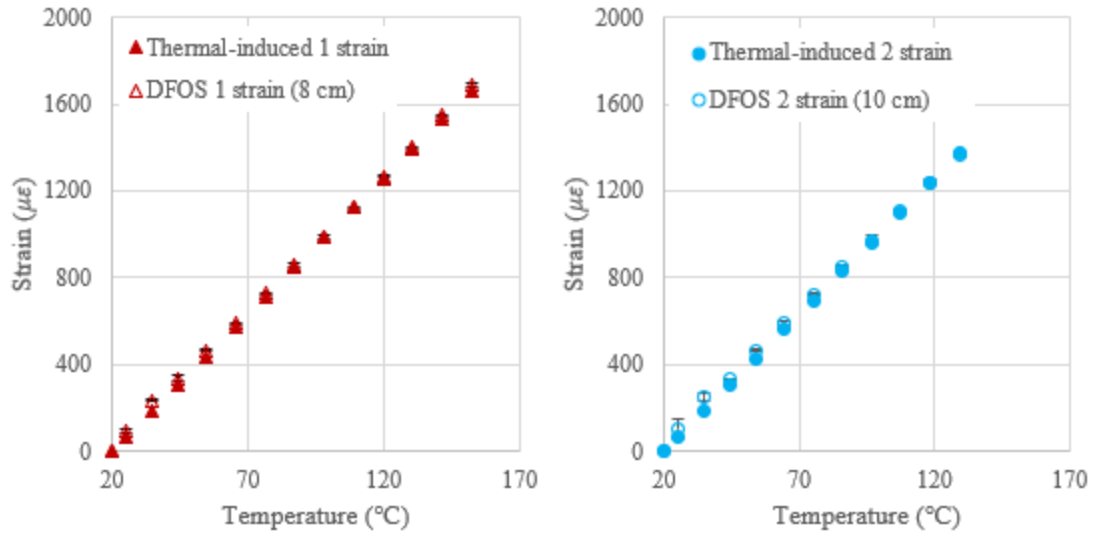
(a)

(b)
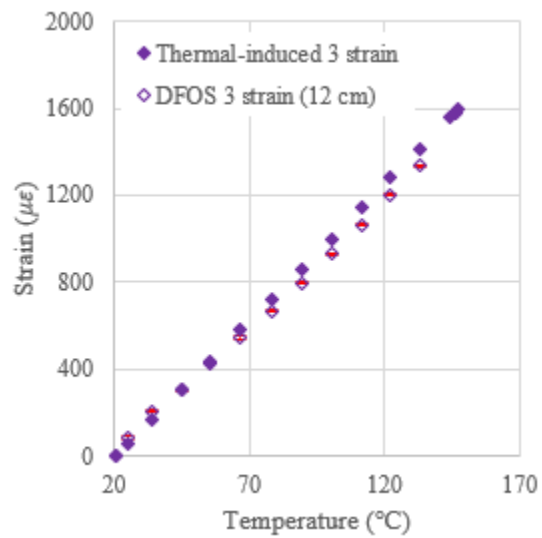
(c)

Figure 3.11 Measured strain-temperature relationships from DFOS covered by epoxy with a bond length of (a) 8 cm (b) 10 cm (c) 12 cm

3.6 Finite Element Validation

3.6.1 Finite Element Model Establishment and Calibration

To further verify the effectiveness of using distributed fiber optic sensors (DFOS) for

measuring thermal-induced strain of steel plates, a numerical model in ABAQUS was

established to obtain optical fiber strains after subjecting plates to thermal load. Because the

polymer coatings were not considered in the experimental test, three components were included

in the numerical model, namely steel plate, epoxy, and optical fiber. The local specimen length

inside the furnace, having a constant temperature, was simulated and a uniform temperature load

can be applied in this local area. Moreover, due to the symmetry of the test specimen, only a 1/8

model was established to simplify modeling and save computational cost. Figure 3.12 shows the

finite element model, based on the dimensions of the test specimen. In the 1/8 model, for a bond

length of 8 cm, the length and cross-section of the steel plate were 40 mm and 5 mm × 1 mm

(width × thickness), respectively. The diameter of the half optical fiber was 0.125 mm. The

epoxy's dimensions were approximately 2 mm wide, 0.5 mm high, and 40 mm long according to

the actual measurement. The 3D stress element-C3D8R (i.e., an 8-node linear brick, reduced

integration, hourglass control) was used to simulate the three components. The TIE technique

available in the ABAQUS was used for connecting the optical fiber and the epoxy as well as the

steel plate and epoxy. This TIE constraint can be applied to make the translational and rotational

motion equal for a pair of surfaces and ties two separate surfaces together to avoid relative

motion between them. One surface in the constraint is designated to be the slave surface; the

other surface is the master surface. The master surface usually has a higher stiffness than the

slave surface. Therefore, the steel surface is the master surface, while epoxy is the slave surface.

Similarly, epoxy is the master surface, while optical fiber is the slave surface when they are

paired. Analysis default is chosen for the discretization method, and the position tolerance uses computed default. Both adjust the slave surface initial position and tie rotational degree of freedoms if applicable are toggled on. X and Z symmetry constraints (i.e., U1 = UR2 = UR3 = 0 and U3 = UR1 = UR2 = 0) were created on the vertical cut surface and longitudinal cut in the middle surface respectively due to the symmetry. A uniform temperature of 10 ℃ was applied on the whole model region. This applied temperature load was in accordance with the test procedure, and ideally the local epoxied region in the furnace would have a uniform temperature distribution. The static, general step was selected, and the geometry non-linearity was considered in the numerical modeling. The mesh sensitivity was analyzed first to obtain mesh-independent simulation results. Specifically, the general mesh size for the steel plate was 0.5 mm, while the general mesh size for the epoxy and optical fiber was 1 mm. Locally, at the interface between the optical fiber and epoxy, there were 12 elements. There were eight elements for the chord of the cross-section of the optical fiber. Four elements were set for both the thickness and width of the cross-section of the epoxy. The basic properties of the three materials are listed in Table 3.1. Since the epoxy properties were unknown, it was necessary to calibrate the properties for the epoxy, especially for the elastic modulus. After calibration, the elastic modulus of 6.7 MPa was adopted. The calculated steel and DFOS normal strains (shown as path 1 and path 2 in Figure 3.12) along the longitudinal direction on the vertical cut surface from the free end to the symmetrically restrained end were shown in Figure 3.13(a). The excellent agreement between the steel and optical fiber strains can be observed after about 8 mm from the free end. Their constant strains are equal to the theoretical strain value (i.e., 126 $\mu\varepsilon$) calculated by the production of the temperature increment and the thermal expansion coefficient of steel. Figure 3.13(b)-(d) shows the numerical normal strains of the optical fiber, steel plate and epoxy at a temperature

increment of 10 ℃. At the free end (less than 10 mm), the uneven strain distribution along the

longitudinal and transverse directions is significant for all three components. Figure 3.13(e)

shows the optical fiber strains on the steel plate with different bond lengths, and they show good

consistency except for the region close to the free end. The effect of bond length of the optical

fiber covered by the epoxy on the steel plate subjected to a constant temperature is not

significant. From this validation, it is believed that the established numerical model is accurate to

simulate thermal strains.

Table 3.1 Summary of material properties

Properties	Steel	Optical fiber	Epoxy
Elastic modulus (GPa)	200	72	6.7*
Poisson's ratio	0.3	0.17	0.34
Density (kg/m³)	7850	2440	1150
Conductivity (W/(m·℃))	45	0.05	7.47
Specific heat (J·(kg·℃))	420	1620	1100
Thermal expansion coefficient ($\mu\varepsilon$/℃)	12.6	0.5	55.0
*Elastic modulus of epoxy was calibrated and not all properties had significant influence in the present numerical model.			

Path 2

Path 1

$U3 = UR1 = UR2 = 0$

$U1 = UR2 = UR3 = 0$

Epoxy

Optical fiber

Steel plate

Vertical cut surface

Longitudinal cut in
the middle
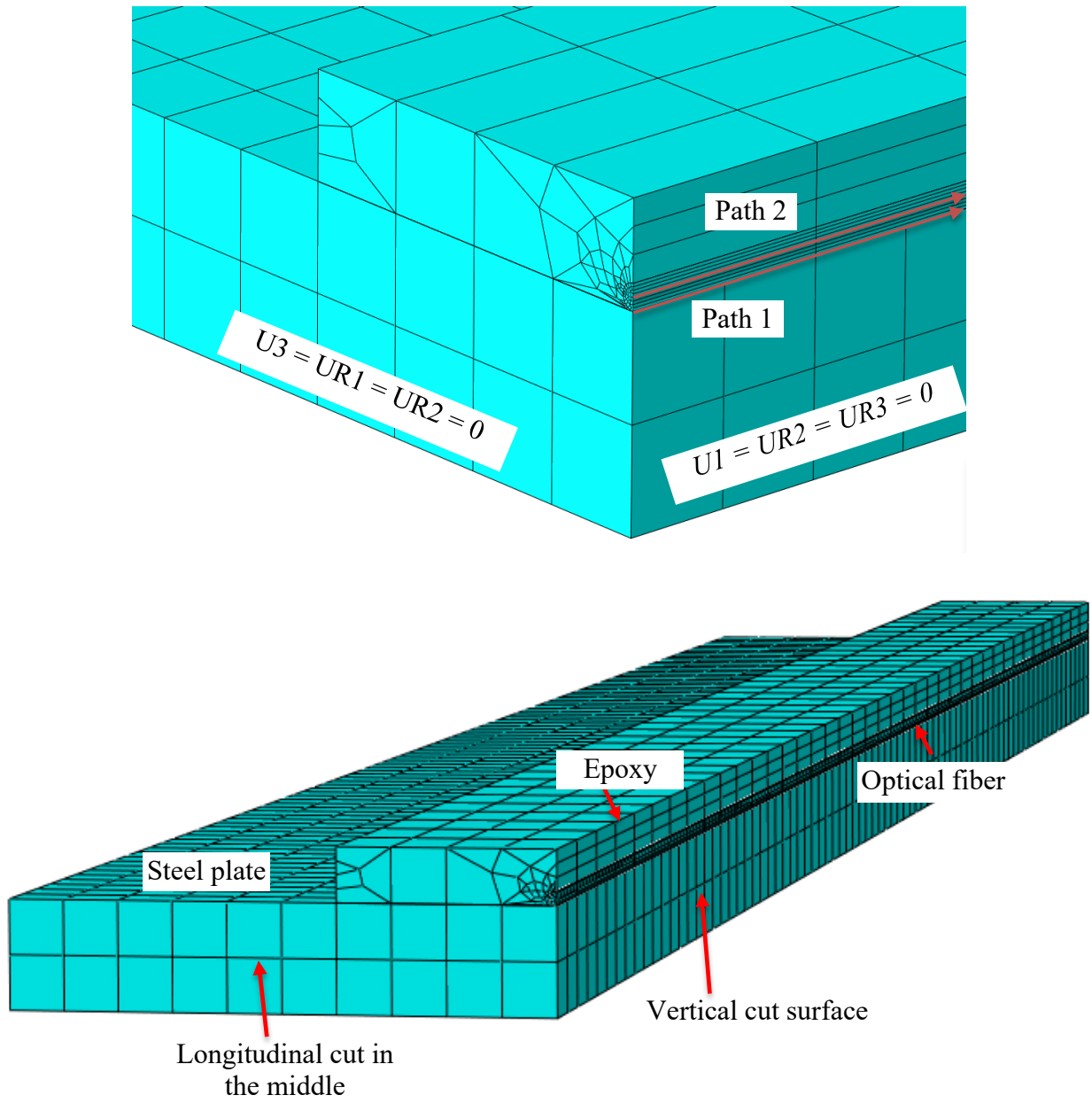
Figure 3.12 Locally 1/8 finite element model with local mesh
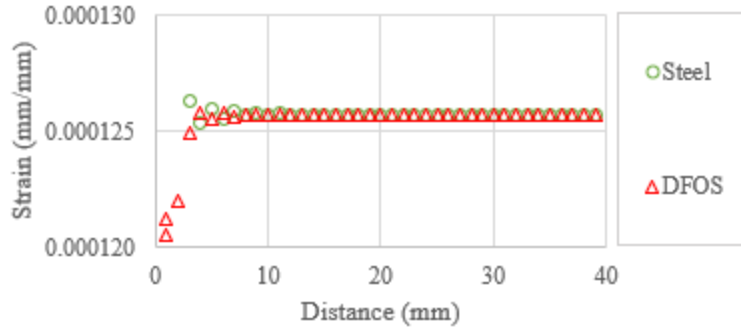
(a)
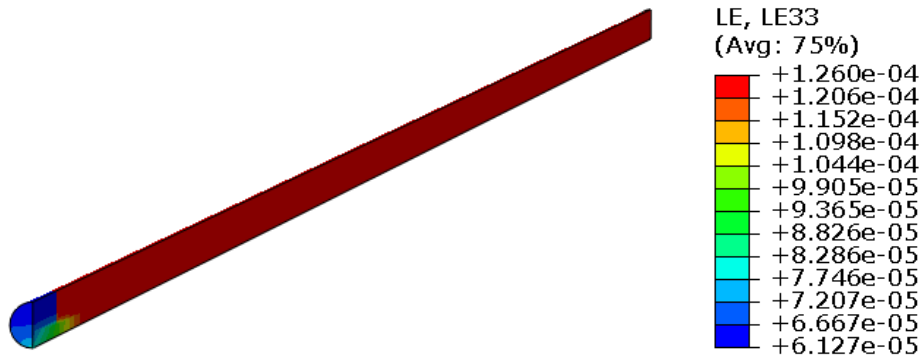
(b)
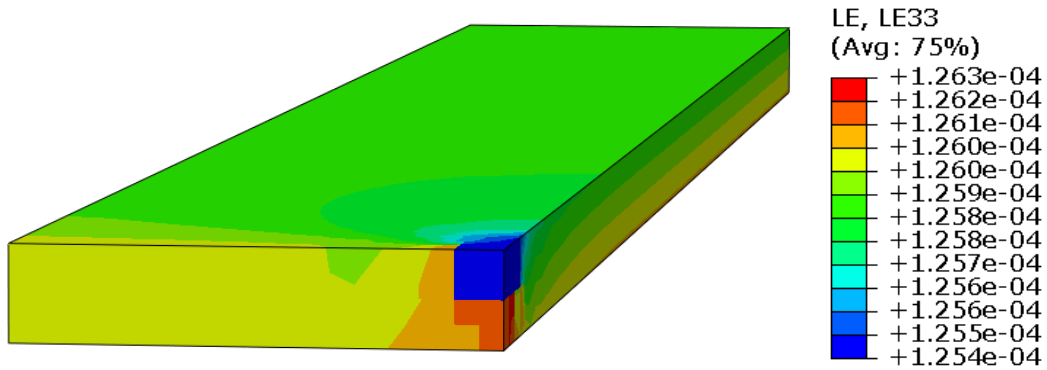
(c)

Figure 3.13 (a) Normal strain distribution along the steel plate (Path 1) and optical fiber (Path 2) (b) Optical fiber (c) steel plate (d) epoxy normal strain contour (e) bond length effect (unit in (b), (c), (d) is mm/mm)
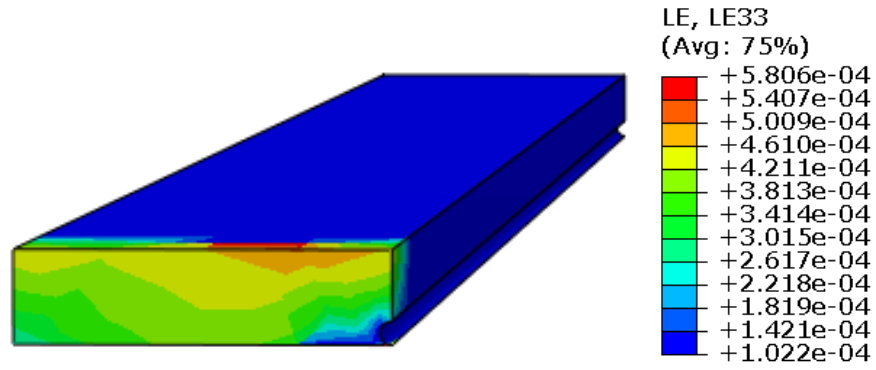
(d)
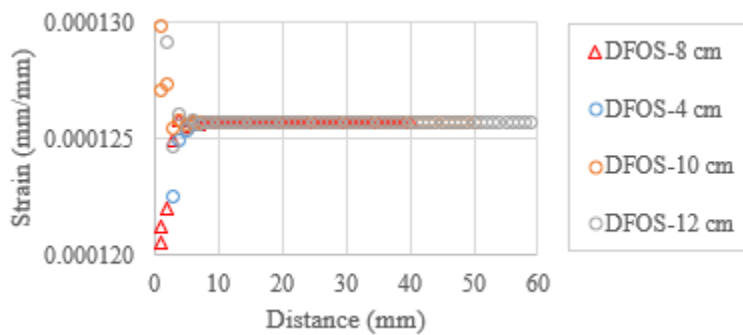
(e)

Figure 3.13 cont. (a) Normal strain distribution along the steel plate (Path 1) and optical fiber (Path 2) (b) Optical fiber (c) steel plate (d) epoxy normal strain contour (e) bond length effect (unit in (b), (c), (d) is mm/mm)

3.6.2 Parametric Study

The parametric studies were conducted to further understand the factors affecting the strain transfer coefficient between the optical fiber and the host material. The strain transfer coefficient is defined as the ratio of the constant optical fiber strain (as shown in Figure 3.13(a)) to the thermal-induced strain (i.e., 126 $\mu\varepsilon$) to facilitate comparison. The basic case for comparison was the validated model with the parameters shown in Table 3.1. Therefore, the effect of the thermal expansion coefficients and elastic moduli of the optical fiber, epoxy, and host material was investigated. Moreover, the initial defect of the epoxy covering on the optical

87

fiber was investigated, and a normal-distribution epoxy shape was designed to secure the strain transfer for future intelligent instrumentation and construction.

3.6.2.1 Coating layers

The coatings of the optical fiber were stripped off, and the glass core and cladding were directly covered by the epoxy in this study. However, the coatings were usually included in the numerical and analytical strain transfer analyses at ambient temperature. One study by Her and Huang (2013) conducted a numerical investigation on the strain transfer of the optical fiber with the coatings subjected to thermal load of 20-70 ℃, and the experimental validation was not provided. Here, the coatings of the optical fiber were included in the numerical model and the epoxy shape (a maximum thickness of 0.0625 mm) further validated the finite element model accuracy and effectiveness in the study. Figure 3.14 shows the meshed finite element model with protective coating. The diameter of the protective coating was 0.242 mm. The elastic modulus was 6.7 MPa, the Poisson's ratio was 0.38, and the thermal expansion coefficient was 76 ppm/℃. The interactions between the optical fiber and coating as well as between the coating and epoxy used the TIE bond available in ABAQUS. The local mesh seeds for the optical fiber, coating and epoxy were the same at the interaction edges. Other parameters were consistent with those in Section 6.1. Figure 3.15 shows the numerical optical fiber strain distribution along the path (as indicated in Figure 3.14) from the free end to the symmetry end. A significant strain transfer can be observed from this figure and the maximum strain is smaller than 126 $\mu\varepsilon$. In other words, the strain transfer coefficient is smaller than one, and the strain transfer coefficient is consistent with the results in most studies (Wang and Dai 2019). This small strain transfer coefficient is attributed to the presence of the protective coating layer and limited contact area of the epoxy. In addition, the epoxy construction with small dimensions seems impossible unless robot assisted

instrumentation and construction is applied. Therefore, the present numerical model is reliable and can be used for further parametric analysis.
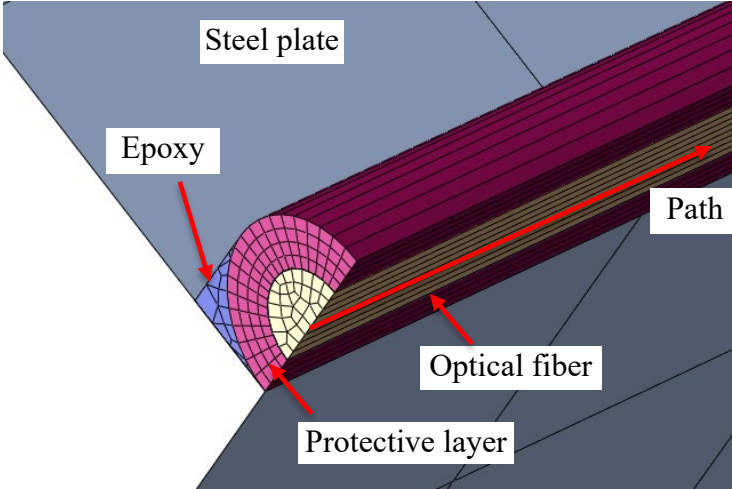
Figure 3.14 Finite element model with protective coating
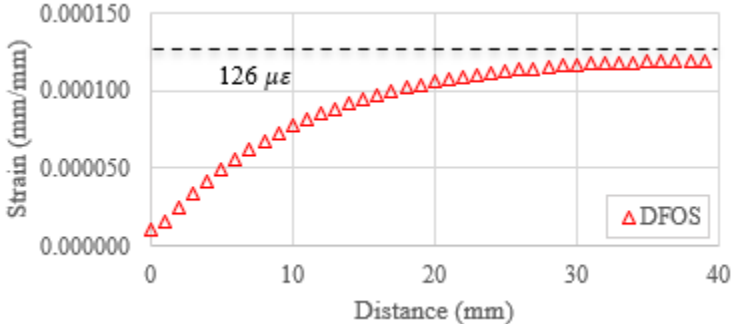
Figure 3.15 The strain distribution of the optical fiber along the path (as indicated in Figure 3.14) from the free end to the symmetry end

3.6.2.2 Thermal expansion coefficients of optical fiber, epoxy, and host materials

Generally, the glass optical fiber has a low coefficient of thermal expansion (CTE, less than 3 ppm/°C). From Figure 3.16(a), the strain transfer coefficient slightly increases with the CTE of the optical fiber. The same trend is observed for the effect of CTE of the epoxy on the

strain transfer coefficient as shown in Figure 3.16(b). The strain transfer coefficient linearly

increases with the epoxy CTE since the optical fiber directly contacts with the epoxy and the

sensing function for the steel plate is achieved through the epoxy connection. However, Figure

3.16(c) shows the strain transfer coefficient decreases with the CTE of the host material. The

strain transfer coefficient significantly reduces before the CTE of 12.6 ppm/℃ and then, it

decreases slowly. At 5.5 ppm/℃, the strain transfer coefficient equals 1.0. The strain transfer

coefficient variation and decreasing trend of the CTE and host material are similar to the

conclusion found in Wang and Dai (2019).
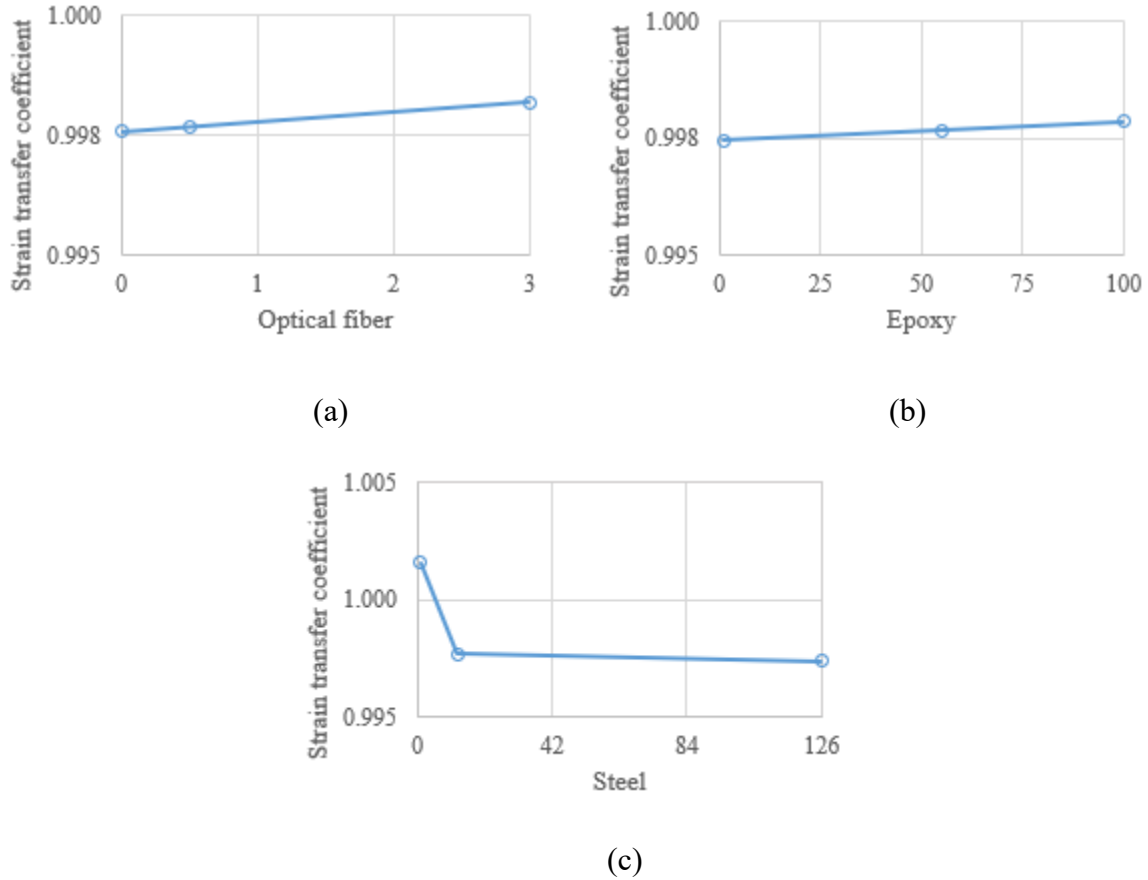
Figure 3.16 Strain transfer changes with coefficient of thermal expansion (unit: (mm/mm)/°C)
(a) optical fiber (b) epoxy (c) host material

3.6.2.3 Elastic moduli of optical, epoxy, and host materials

Figure 3.17(a) shows the strain transfer coefficient with the elastic modulus (E) of the

optical fiber. The strain transfer coefficient decreases with the E of the optical fiber. However,

the strain transfer coefficient linearly increases with the E of the epoxy. From the previous study

(Wang and Dai 2019), the increase of the shear modulus of the adhesive layer increases the strain

transfer efficiency, and a stiffer adhesive layer can obtain a high strain transfer coefficient

because the strain transfer from the host material to the optical fiber depends on the interfacial

shear stress. At the elastic modulus of 100 MPa, the strain transfer coefficient equals 1.0 in

Figure 3.17(b). Figure 3.17(c) shows that the strain transfer coefficient increases with the elastic

modulus of host material, and then the increasing rate slows with a further increase of the elastic

modulus since the restraint on the epoxy deformation and resulting optical fiber deformation

applied by the host material with high stiffness increases when subjected to thermal load.
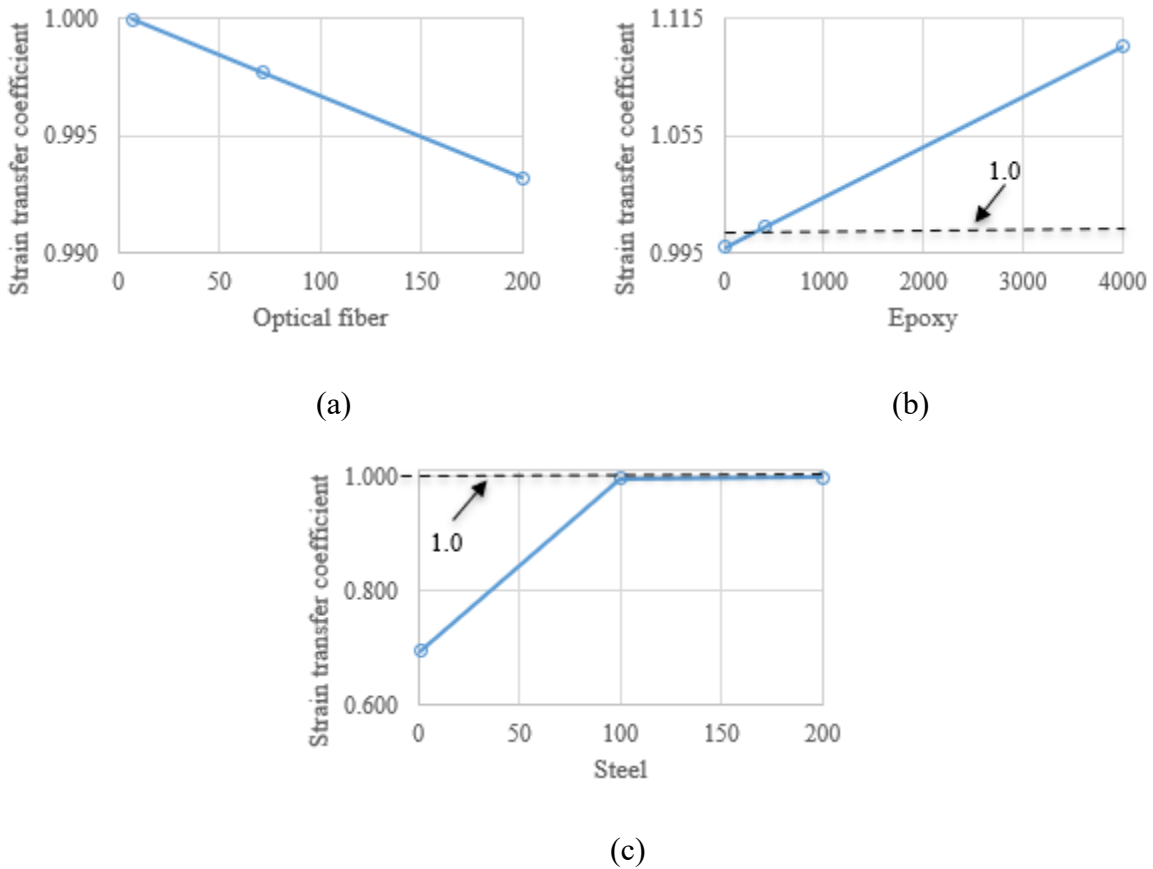
Figure 3.17 Strain transfer changes with elastic modulus (a) optical fiber (unit: GPa) (b) epoxy (unit: MPa) (c) host material (unit: GPa)

3.6.2.4 Non-constant temperature effect

Since the present experimental and numerical studies only consider the steel plate

instrumented with optical fiber covered by epoxy subjected to a constant temperature, an

investigation on the effect of a non-constant temperature distribution may be of interest to the

readers. Here, four temperature distributions were investigated in addition to constant

temperature as listed in Table 3.2. Four different regions of equal length were created for the

whole numerical model through cell partition and the four regions were assigned for different

temperature increments to achieve each non-constant temperature distribution. As shown in

Figure 3.18(a), four regions (A, B, C and D from free to symmetry ends) had temperature

increments of 2.5℃, 5℃, 7.5℃, and 10℃, respectively, representing the linear temperature

distribution case. Figure 3.18(b) shows optical fiber strain distributions over 40 mm subjected to

different temperature distributions. Generally, the strain distributions follow corresponding

temperature distributions. At the free end, an obvious strain transfer on the optical fiber is

observed for the linear temperature and non-linear temperature 1 cases where the overall length

of the instrumented optical fiber sensors was subjected to thermal load. For the non-linear

temperature 2 and 3 cases, not only was the non-linear temperature distribution effect

investigated, but the effect of the bond length (greater than the length subjected to thermal load)

on the optical fiber strain distribution was also revealed. The influence regions in A and B by the

thermal strain of the steel plate subjected to temperature distributions in C and D are circled in

black in Figure 3.18(b), i.e., the strain measured by the optical fiber covered by epoxy out of the

thermal load region can be quantified.

Table 3.2 Cases for investigating non-constant temperature effect (unit: ℃)

	A	B	C	D
Constant temperature	10	10	10	10
Linear temperature	2.5	5	7.5	10
Nonlinear temperature 1	10	5	5	10
Nonlinear temperature 2	0	0	10	10
Nonlinear temperature 3	0	0	2.5	10

(a)
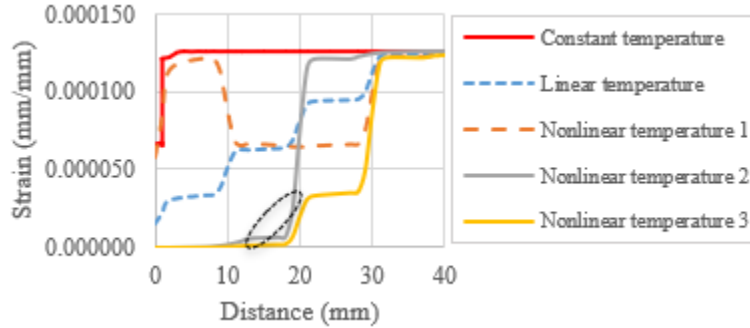
(b)

Figure 3.18 (a) Four temperature regions along steel plate (b) Optical fiber strain distributions subjected to different temperature distributions

3.6.2.5 Initial defects of the epoxy and epoxy shape effect

In the practical construction for covering optical fiber on the host material (such as steel) by using epoxy, it may induce a defect due to the circular shape of the optical fiber as shown in Figure 3.19. A void defect in the epoxy along the longitudinal direction can be created in the numerical model and its effect on the optical fiber strain is investigated. From Figure 3.20, it is found that the initial defect has significant effect on the strain distribution of the optical fiber along the center path, and the strain distribution is similar to the optical fiber with a protective coating layer outlined in Section 3.6.2.1. From previous discussion, the epoxy shape may affect the optical fiber strain. Therefore, a normal distribution shape of the epoxy is investigated, and the epoxy shape is shown in Figure 3.21. The positions of the five points (O, A, B, C, and D) to determine the cross-section (unit: mm) of the epoxy shape are as follows: (0, 0), (0, 0.399), (-1, 0.242), (-2, 0.054), and (-2, 0). The curve segment AC of the normal distribution shape is created by a spline with a middle point B, facilitating model establishment and fabrication. The

94

numerical optical fiber strain distribution along the center path is shown in Figure 3.19. It is found that this normal distribution shape shows an insignificant effect on the optical fiber strain. However, this normal distribution epoxy shape may be beneficial for enhancing the bond between the epoxy and steel plate in the transverse direction (i.e., point D) at high temperatures.
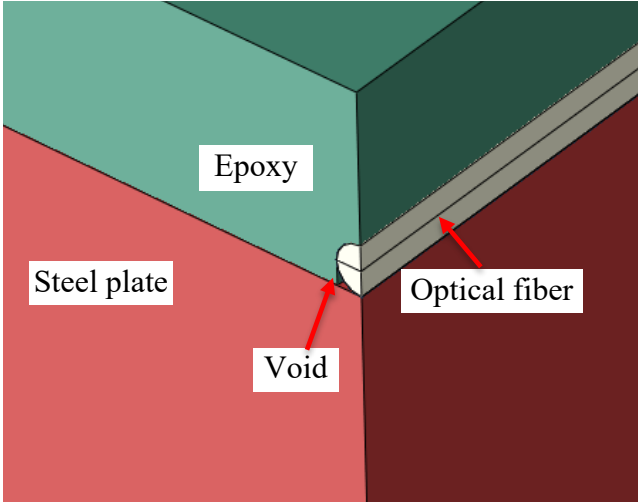
Figure 3.19 Finite element model with void defect
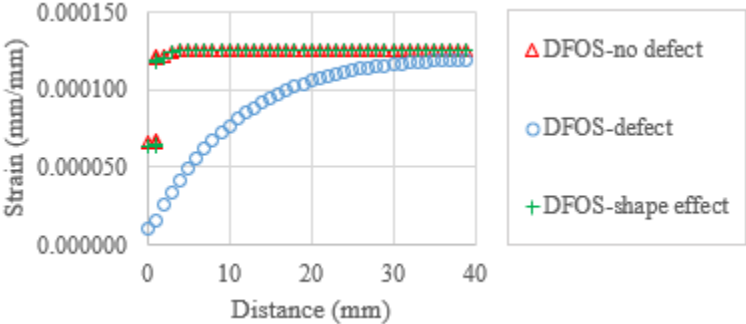
Figure 3.20 Strain distribution of the optical fiber along the center path
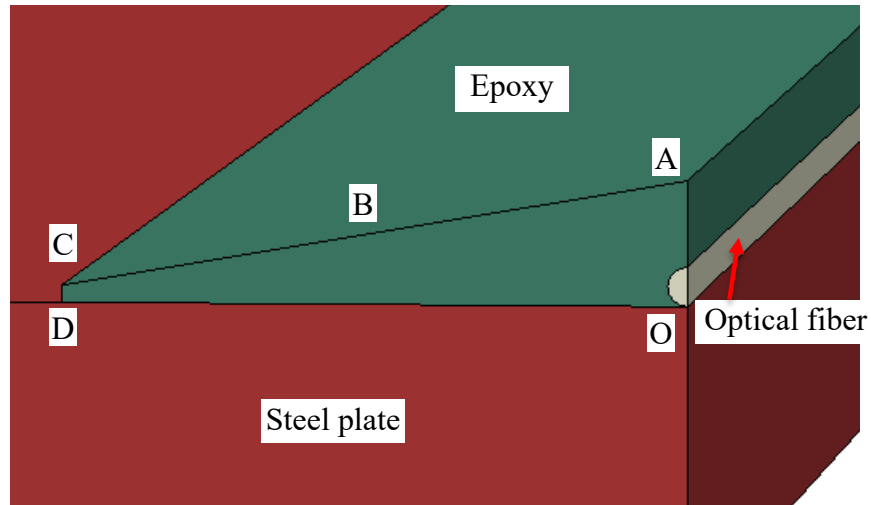
Figure 3.21 Finite element model with normal-distribution epoxy shape

3.7 Summary

This study experimentally investigated the effectiveness and limitation of Rayleigh scattering-based, distributed fiber optic sensors without coatings bonded to a steel plate for measuring temperature and strain simultaneously subjected to a local constant temperature. Moreover, a local finite element model was established to simulate the sensing strain of the optical fiber, and parametric studies were conducted to investigate factors affecting the strain transfer coefficient between the host structure and the optical fiber by using the calibrated numerical model. Several conclusions are drawn as follows.

- From the temperature calibration test, the advantage of distributed fiber optic sensors for measuring temperature distribution was demonstrated by the uneven temperature distribution inside the furnace. A parabolic equation with a determination coefficient of 1.000 was fitted for the temperature and accumulated Rayleigh frequency relationship. From the strain calibration test, a maximum strain of less than 1600 $\mu\varepsilon$ could be measured in distributed fiber optic sensors without coatings.

- From the application test, the distributed fiber optic sensors instrumented on the steel plate by the epoxy with different bond lengths in the constant temperature zone can accurately measure the temperatures as verified by the thermocouple readings and the thermal-induced strains.

- The local numerical model well simulated the optical fiber strain subjected to a uniform temperature load in the elastic stage. From the parametric studies, the most significant factor affecting the strain transfer coefficient was elastic modulus of epoxy and the strain transfer coefficient can increase to more than one at a high elastic modulus of epoxy. The strain transfer coefficient was also sensitive to the thermal expansion coefficient and elastic modulus of the host material. Moreover, the initial defect effect on the optical fiber strain distribution was like the protective coating effect. The strain measured by the optical fiber covered by epoxy out of the thermal load region can be quantified to observe the effects of using a bond length greater than the length subjected to thermal load.

Although the present study examines the measurement effectiveness of distributed fiber optic sensors, some limitations can be observed as follows. Higher temperature can be considered in the future since the maximum temperature was about 150 ℃ in the present study due to the use of distributed fiber optic sensors without protective coatings. Therefore, the higher temperature effect on the interaction between the steel and epoxy as well as the temperature-dependent material properties (such as thermal expansion coefficient and elastic modulus) should be considered in the numerical model. Also, the coupled temperature and structure behavior analysis during the transient heat transfer process can be conducted since the present test only applies a uniform temperature field.

Chapter 4 Conclusions

In the present study, experimental, analytical, and numerical studies were performed to investigate the feasibility of strain and temperature measurements of steel specimens under high temperatures using Rayleigh scattering based distributed fiber optic sensors.

The first study experimentally investigates the effect of heat treatment on Rayleigh scattering based distributed single-mode fiber optic temperature measurement. A finite element model was established to investigate the effect of thermal expansion coatings on the optical fiber core strains and thus, temperature sensitivity before the coatings soften and melt away. A theoretical derivation for the fiber core strains, using Lame equations, was performed to validate the accuracy of the finite element model. It was found that the one-time heat treatment eliminates the hysteresis effect and stabilizes the Rayleigh scattering based fiber optic temperature measurement up to 1000 ℃. The typical dual-layer coating effect on the temperature sensitivity of the Rayleigh frequency shift can be neglected at high temperatures in a civil engineering application. Numerical parametric studies are performed to design coatings of fiber optic temperature sensors. The present study is promoting distributed fiber optic temperature sensor development and application.

The second study aims to quantify Rayleigh scattering-based measurement accuracy of distributed fiber optic sensors under a heating-holding load protocol and characterize the effect of a polymer coating on the sensors as the polymer softens and melts away at elevated temperatures. Two segments of a coated single-mode optical fiber were loosely attached and firmly bonded to a steel plate, respectively. When locally heated up to 405 ℃ in a furnace, the two segments were used to measure temperature alone and thermal-induced strain. The axial displacement associated with the strain measurement was compared with that of a dial gauge. A temperature increment of 13 °C (<< 20 °C) is recommended to ensure successful correlation

analysis of Rayleigh scattering signals. The polymer was found to start softening at 155 ℃ and melting at 267 ℃. As temperature sensors, optical fibers with an insulation sheath can accurately measure temperature up to 155 °C without and up to 267 °C with thermo-mechanical analysis of sheath-fiber bonding behavior. As strain sensors, optical fibers with temperature compensation are accurate for strain measurement up to 155 °C, above which strain transfer analysis is required due to softening of the fiber coating. Under a large temperature gradient covering 155 °C to 267 °C, the fibers attached on steel plates with epoxy function like an extensometer as a center portion of the coating with the high-end temperature is melted as verified by microscopic analysis.

The third study aims to experimentally and numerically investigate effectiveness and limitation of Rayleigh scattering-based, distributed fiber optic sensors (DFOS) without coatings for measuring temperature and strain of a steel plate subjected to a local constant temperature. The DFOS were bonded to the steel plate by an epoxy with different bond lengths to measure coupled strain and temperature effect, while the DFOS near the end of the epoxied segment measured the temperature effect only for temperature discrimination. It was found that the DFOS accurately measured the temperature and strain of the steel plate with different bond lengths of the epoxy, as compared to the thermocouple temperature and thermal-induced strain, respectively. The maximum strain (or temperature) that the DFOS without coatings could measure for the steel plate was less than 1600 $\mu\varepsilon$ (or 150 ℃). Moreover, a local finite element model with the calibrated elastic modulus of the epoxy subjected to a uniform temperature field well captured optical fiber strains in the elastic stage. From parametric studies, the effect of the thermal expansion coefficients and elastic moduli of the optical fiber, epoxy, and host material as well as initial defect between the optical fiber and epoxy on the strain transfer coefficient was

investigated. The elastic modulus of epoxy within 100 MPa and the rectangular cross-section of epoxy (0.5 mm thick and 4 mm wide) could achieve a strain transfer coefficient of 0.997, while the initial defect had a similar effect on the strain transfer to the protective coating. The normal-distribution epoxy shape was designed for guiding robot assisted intelligent instrumentation and construction in the future.

References

Ansari, F. and L. Yuan, 1998. "Mechanics of bond and interface shear transfer in optical fiber sensors." *Journal of Engineering Mechanics*, 124(4), 385–394.

Bado, M.F., and J.R. Casas, 2021. "A review of recent distributed optical fiber sensors applications for civil engineering structural health monitoring." *Sensors*, 21, 1818.

Bado, M.F., D. Tonelli, F. Poli, D. Zonta, and J.R. Casas, 2022. "Digital twin for civil engineering systems: an exploratory review for distributed sensing updating." *Sensors*, 22, 3168.

Bao, X., and L. Chen, 2012. "Recent progress in distributed fiber optic sensors." *Sensors*, 12(7), 8601–8639.

Bao, Y., and G. Chen, 2015. "Strain distribution and crack detection in thin unbonded concrete pavement overlays with fully distributed fiber optic sensors." *Optical Engineering*, 55(1), 011008.

Bao, Y., and G. Chen, 2016a. "High-temperature measurement with Brillouin optical time domain analysis of an annealed fused-silica single-mode fiber." Opt. Lett. 41, 3177-3180.

Bao, Y., and G. Chen, 2016b. "Temperature-dependent strain and temperature sensitivities of fused silica single mode fiber sensors with pulse pre-pump Brillouin optical time domain analysis." *Measurement Science and Technology*. 27, 065101.

Bao, Y., M.S. Hoehler, C.M. Smith, M. Bundy, and G. Chen, 2017a. "Temperature measurement and damage detection in concrete beams exposed to fire using PPP-BOTDA based fiber optic sensors." *Smart Materials and Structures*, 26(10), 105034.

Bao, Y., M.S. Hoehler, C.M. Smith, M. Bundy, and G. Chen, 2020. "Measuring three-dimensional temperature distributions in steel–concrete composite slabs subjected to fire using distributed fiber optic sensors." *Sensors*, 20(19), 5518.

Bao, Y., W. Meng, Y. Chen, G. Chen, and K.H. Khayat, 2015. "Measuring mortar shrinkage and cracking by pulse pre-pump Brillouin optical time domain analysis with a single optical fiber." *Materials Letters*, 145, 344–346.

Bao, Y., Y. Chen, H. Matthew, C. Smith, B. Matthew, and G. Chen, 2016. "Experimental analysis of steel beams subjected to fire enhanced by Brillouin scattering-based fiber optic sensor data." ASCE J. Struct. Eng. 143, 04016143.

Bao, Y., Y. Chen, M.S. Hoehler, C.M. Smith, M. Bundy, and G. Chen, 2017b. "Experimental analysis of steel beams subjected to fire enhanced by brillouin scattering-based fiber optic sensor data." *Journal of Structural Engineering*, 143(1), 04016143.

Barrias, A., J.R. Casas, and S. Villalba, 2016. "A review of distributed optical fiber sensors for civil engineering applications." *Sensors*, 16, 748.

Bastianini, F., R. Di Sante, F. Falcetelli, G. Bolognini, D. Marini, 2019. "Optical fiber sensing cables for brillouin-based distributed measurements." *Sensors*, 19(23), Article 5172.

Chen, J., and B. Young, 2007. "Experimental investigation of cold-formed steel material at elevated temperatures." *Thin-Walled Structures*, 45(1), 96–110.

Chen, J., B. Young, and B. Uy, 2006. "Behavior of High Strength Structural Steel at Elevated Temperatures." *Journal of Structural Engineering*, 132(12), 1948–1954.

Choi, B.H., and I.B. Kwon, 2019. "Damage mapping using strain distribution of an optical fiber embedded in a composite cylinder after low-velocity impacts." *Composites Part B: Engineering*, 173, Article 107009.

Fan, L., and Yi Bao, 2021. "Review of fiber optic sensors for corrosion monitoring in reinforced concrete." *Cement and Concrete Composites*, 120, 104029.

Fan, L., Y. Bao, and G. Chen, 2018. "Feasibility of distributed fiber optic sensor for corrosion monitoring of steel bars in reinforced concrete." *Sensors*, 18(11), 3722.

Froggatt, M., and J. Moore, 1998. "High-spatial resolution distributed strain measurements in optical fiber with Rayleigh scatter." *Applied Optics*, 37(10), 1735–1740.

Gagliardi, G., 2010. "Probing the ultimate limit of fiber-optic strain sensing." Science, 330(9), 1081-1084.

"Global distributed fiber optic sensor market report 2021-2026." 2022. *Research and Markets*.

Gu, H., H. Dong, G. Zhang, J. He, and H. Pan, 2013. "Effects of polymer coatings on temperature sensitivity of Brillouin frequency shift within double-coated fibers." *IEEE Sensors* Journal 13 864-869.

Guo, C., Y. Zhang, M. Klegseth, J. Gao, and G. Chen, 2020. "Micrometer-accuracy 2D displacement interferometer with plasmonic metasurface resonators." Opt. Lett. 45 6474-6477.

Her, S.C., and C.Y. Huang, 2013. "Thermal strain analysis of optic fiber sensors." *Sensors*, 13(2), 1846–1855.

Kim, S., 2017. "Characterisitcs of strain transfer and the reflected spectrum of a metal-coated fiber Bragg grating sensor." *Optics and Lasers in Engineering*, 96, 83-93.

Kim, S., M. Jeong, I. Lee, and I.B. Kwon, 2013b. "Effects of mechanical and geometric properties of adhesive layer on performance of metal-coated optical fiber sensors." *International Journal of Adhesion and Adhesives*, 47, 1-12.

Kim, S.W., M.S. Jeong, I. Lee, E.H. Kim, I.B. Kwon, and T.K. Hwang, 2013a. "Determination of the maximum strains experienced by composite structures using metal coated optical fiber sensors." *Composites Science and Technology*, 78, 48–55.

Kishida, K., C.H. Li, K. Nishiguchi, Y. Yamauchi, A. Guzik, and T. Tsuda, 2012. "Hybrid Brillouin-Rayleigh distributed sensing system." OFS2012 22nd Int. Conf. Opt. Fiber Sensors. 8421, 84212G.

Kishida, K., C.H. Li, K. Nishiguchi, Y. Yamauchi, A. Guzik, and T. Tsuda, 2012. "Hybrid Brillouin-Rayleigh distributed sensing system." OFS2012 22nd International Conference on Optical Fiber Sensors, 8421, Article 84212G – 4.

Kishida, K., Y. Yamauchi, and A. Guzik, 2014. "Study of optical fibers strain-temperature sensitivities using hybrid Brillouin-Rayleigh system." *Photonic Sensors*, 4 1-11.

Koyamada, Y., 1998. "New technique for distributed strain measurement in optical fibers with very high sensitivity by making use of Rayleigh backscattering." Technical Report of IEICE OFT98-23, 21–25.

Li, Y., F. Zhang, and T. Yoshino, 2003. "Wide temperature-range Brillouin and Rayleigh optical-time-domain reflectometry in a dispersion-shifted fiber." Appl. Opt. 42, 3772-3775.

Li, Y.H., M.W. Yang, D.N. Wang, J. Lu, T. Sun, and K.T.V. Grattan, 2009. "Fiber Bragg gratings with enhanced thermal stability by residual stress relaxation." Opt. Express 17, 19785-19790.

Lu , X., M. A. Soto, and L. Thevenaz, 2018. "Impact of the fiber coating on the temperature response of distributed optical fiber sensors at cryogenic ranges." *Journal of Lightwave Technology* 36, 961-967.

Petrie, C.M., et al., 2019. "High-temperature strain monitoring of stainless steel using fiber optics embedded in ultrasonically consolidated nickel layers." *Smart Materials and Structures*, 28, Article 085041.

Piccolo, A., S. Delepine-Lesoille, D. Leduc, and Y. Lecieux, 2019. "Distributed optical fiber strain and temperature sensing system performances: Brillouin vs Rayleigh." Proceedings of Seventh European Workshop on Optical Fiber Sensors, 11199, Article 111991Z.

Planes, I., S. Girard, A. Boukenter, E. Marin, S. Delepine-Lesoille, C. Marcandella, and Y. Ouerdane, 2017. "Steady γ-Ray Effects on the Performance of PPP-BOTDA and TW-COTDR Fiber Sensing." *Sensors*. 17, 396.

"Polymer Coatings for Silica Optical Fiber." 2009. *Polymicro Technologies*. Retrieved from https://www.molex.com/mx_upload/superfamily/polymicro/pdfs/Polymer_Coatings_for_Silica_Optical_Fiber_Nov_2009.pdf.

Rizzolo, S., E. Marin, A. Morana, A. Boukenter, Y. Ouerdane, M. Cannas, J. Perisse, S. Bauer, J. R. Mace, and S. Girard, 2016. "Investigation of coating impact on OFDR optical remote fiber-based sensors performances for their integration in high temperature and radiation environments." J. Light. Technol. 34, 4460-4465.

S. J. Mihailov, 2012. "Fiber bragg grating sensors for harsh environments." Sens. 12, 1898-1918.

S. Loranger, M. Gagné, V. Lambin-Iezzi, and R. Kashyap, 2015. "Rayleigh scatter based order of magnitude increase in distributed temperature and strain sensing by simple UV exposure of optical fibre." Sci. Rep. 5, 11177.

Shin, I.H., S. Ju, S.P. Veetil, W.T. Han, and D.Y. Kim, 2008. "Simple model for frozen-in viscoelastic stress in optical fibers." Opt. Commun. 281, 2504.

Tan, X., and Y. Bao, 2022a. "Measuring crack width using a distributed fiber optic sensor based on optical frequency domain reflectometry." *Measurement*, 172, 108945.

Tan, X., P. Guo, X. Zou, and Y. Bao, 2022b. "Buckling detection and shape reconstruction using strain distributions measured from a distributed fiber optic sensor." *Measurement*. (Accepted)

"User's manual of Neubrescope NBX-7020," 2012. Neubrex Co. Ltd.

Wang, H., and J.G. Dai, 2019. "Strain transfer analysis of fiber Bragg grating sensor assembled composite structures subjected to thermal loading." Composites Part B: Engineering, 162, 303–313.

Wang, H., and J.G. Dai, 2019. "Strain transfer analysis of fiber Bragg grating sensor assembled composite structures subjected to thermal loading." *Composite Part B: Engineering*, 162, 303-313.

Wang, H., and P. Xiang, 2016. "Strain transfer analysis of optical fiber based sensors embedded in an asphalt pavement structure." *Measurement Science and Technology*, 27(7), Article 075106.

Wang, H., and Z. Zhou, 2014. "Advances of strain transfer analysis of optical fibre sensors." Pacific Science Review, 16(1), 8–18.

Wang, H., L. Jiang, and P. Xiang, 2018. "Improving the durability of the optical fiber sensor based on strain transfer analysis." *Optical Fiber Technology*, 42, 97–104.

Weiss, K., 1938. "Errors of the dial gauge as an instrument for measuring amplitudes of vibration." Review of *Scientific Instruments*, 9(365).

Xu, P., D. Ba, W. He, H. Hu, and Y. Dong, 2018. "Distributed Brillouin optical fiber temperature and strain sensing at a high temperature up to 1000 °C by using an annealed gold-coated fiber." Optics Express 26 (2018) 29724-29734.

Xu, P., Y. Dong, D. Zhou, C. Fu, J. Zhang, H. Zhang, Z. Lu, L. Chen, and X. Bao, 2016. "1200°C high-temperature distributed optical fiber sensing using Brillouin optical time domain analysis." *Applied Optics* 55, 5471-5478.

Yablon, A. B., 2004. "Optical and mechanical effects of frozen-in stresses and strains in optical fibers." *IEEE J. Sel. Top. Quantum Electron* 10, 2004, 300-311.

Yan, M., X. Tan, S. Mahjoubi, and Y. Bao, 2022. "Strain transfer effect on measurements with distributed fiber optic sensors." *Automation in Construction*, 139, 104262.

Yang, T., H. Wang, and X. Wang, 2021. "Strain transfer characteristics of multi-layer optical fiber sensors with temperature-dependent properties at low temperature." *Sensors*, 21(2), Article 495.

Yuan, L., L.M. Zhou, W. Jin, K.T. Lau, and C. Poon, 2003. "Effect of thermally induced strain on optical fiber sensors embedded in cement-based composites." *Optical Fiber Technology*, 9(2), 95–106.

Zhang, S., H. Liu, A.A.S. Coulibaly, and M. DeJong, 2021. "Fiber optic sensing of concrete cracking and rebar deformation using several types of cable." *Structural Control and Health Monitoring*, 28(2), 1-23.

Zhang, S., H. Liu, J. Cheng, and M.J. DeJong, 2020. "A mechanical model to interpret distributed fiber optic strain measurement at displacement discontinuities." *Structural Health Monitoring*. doi: 10.1177/1475921720964183.

Zhong, H., C. Fu, P. Li, B. Du, C. Du, Y. Meng, and Y. Wang, 2022. "Distributed high-temperature sensing based on optical frequency domain reflectometry with a standard single-mode fiber." *Optics Letters* 47, 882-885.

Zhu, P., X. Xie, X. Sun, and M.A. Soto, 2019. "Distributed modular temperature-strain sensor based on optical fiber embedded in laminated composites." *Composites Part B: Engineering*, 168, 267–273.

Zhu, Y., and G. Chen, 2022. "Rayleigh scattering based, thermal-induced displacement measurement along a steel plate at high temperature." *Journal of Infrastructure Intelligence and Resilience*. (Accepted)